March 2020

Anti-Jam GPS Controlled Reception Pattern Antennas for Man-Portable Applications

Jeffrey A. Maloney
University of Massachusetts Amherst

ANTI-JAM GPS CONTROLLED RECEPTION PATTERN ANTENNAS FOR MAN-PORTABLE APPLICATIONS

A Dissertation Presented

by

JEFFREY A. MALONEY

Submitted to the Graduate School of the
University of Massachusetts Amherst in partial fulfillment
of the requirements for the degree of

DOCTOR OF PHILOSOPHY

February 2020

Electrical and Computer Engineering

ANTI-JAM GPS CONTROLLED RECEPTION PATTERN ANTENNAS FOR MAN-PORTABLE APPLICATIONS

A Dissertation Presented

by

JEFFREY A. MALONEY

Approved as to style and content by:

Ramakrishna Janaswamy, Co-Chair

Do-Hoon Kwon, Co-Chair

Steven D. Keller, Member

Daniel Sheldon, Member

Christopher V. Hollot, Department Head
Electrical and Computer Engineering

ACKNOWLEDGMENTS

First and foremost, I want to express my gratitude to Steven Keller for being a mentor to me these past four years. His guidance and friendship have been instrumental to me during this process. Steve has encouraged me to look into new lines of inquiry and helped me become the engineer I am today. This work could not have been completed without his advice and insight.

Also, I wish to thank my academic advisors, Do-Hoon Kwon and Ramakrishna Janaswamy, both of whom have been central to my development. I only hope that I can live up to their commendable examples as I continue my career. Additionally, I am indebted to Daniel Sheldon for his work on my committee. Dan has offered his insight in the revision of this document, which is better for having had his input.

The faculty at UMass have guided me through my entire college education, and I have benefited from the expertise of every professor who's lectures I have sat through. Specifically, I would like to thank Daniel Holcomb for his assistance and his generosity with his time. Additionally, I have had the benefit these past nine years of having access to the makerspace M5, as well as the equipment and materials therein. I wish to thank Baird Soules for building this wonderful UMass institution and Shira Epstein for the positive changes she has made since joining the faculty.

I also wish to express my gratitude to the staff at ARL and all I have learned from them. First and foremost, to John T. Clark and Theodore K. Anthony for their innumerable contributions to this work. I have learned much from the examples set by these two, particularly decisiveness form John and resourcefulness from Theo. To Arthur Harrison and Russel Harris not only for their technical contributions, but also for letting me pick their brains. I benefited from their years of experience and accumulated institutional knowledge.

Many of the experiments would not have been possible without Abigail Hedden who provided crucial equipment, as well as insight during troubleshooting. Additionally, Steven J. Weiss offered guidance in designing experiments and measurements.

This research was sponsored by the U.S. Army Research Laboratory and was accomplished under Cooperative Agreement Number W911NF-18-2-0311. The views and conclusions contained in this document are my own and should not be interpreted as representing the official policies, either expressed or implied, of the Army Research Laboratory or the U.S. Government. The U.S. Government is authorized to reproduce and distribute reprints for Government purposes notwithstanding any copyright notation herein.

ABSTRACT

ANTI-JAM GPS CONTROLLED RECEPTION PATTERN ANTENNAS FOR MAN-PORTABLE APPLICATIONS

FEBRUARY 2020

JEFFREY A. MALONEY

BS, UNIVERSITY OF MASSACHUSETTS AMHERST

MS, UNIVERSITY OF MASSACHUSETTS AMHERST

PhD, UNIVERSITY OF MASSACHUSETTS AMHERST

Directed By: Professor Ramakrishna Janaswamy

and Professor Do-Hoon Kwon

Military GPS receivers provide crucial information to soldiers in the field, however, the performance of these devices is degraded by in band RF interference, making GPS susceptible to jamming. Anti-jam techniques for aircraft and vehicular platforms have been developed, but at present there is no system for dismounted soldiers. There is a need for an anti-jam system which meets the demands of a dismounted soldier and conforms to the size, weight, and power requirements of a portable device.

A controlled reception pattern antenna, or CRPA, is a potential solution for jammer mitigation. These devices work by steering reception pattern nulls toward the jammer direction, reducing the jammer power which reaches the GPS receiver. Prior CRPA realizations have been designed for use on vehicular and aircraft applications, however, these platforms do not suffer from the same limitations as a man-portable CRPA. Three considerations which are more pertinent for man-portable designs than prior work are (i) distributed antenna element positions and orientations dynamically change during use changing the reception

pattern characteristics, (ii) the user is lower to the ground and moves through the environment meaning that multipath propagation can have a greater effect on CRPA performance, and (iii) the size weight and power constraints for a portable system limit the number of antenna elements reducing the degrees of freedom that can be used for cancellation.

To address these challenges, a framework for man-portable CRPA modeling is presented. This includes development of efficient modeling methods which enable investigations into element perturbations to address the dynamic orientation problem. These and other methods are presented in Chapter 3, along with a discussion of the relative strengths and weaknesses of each. Additionally, a mixed scattering channel model is applied to the CRPA reception patterns, combining diffuse and specular reflection in Chapter 4. Discussion of this model centers around the eigenvalues of the signal covariance matrix and the effect of coherence between multipath components. Following this, Chapter 5 examines the performance of polarimetric CRPAs and space-time adaptive processing for man-portable CRPAs with limited degrees of freedom.

TABLE OF CONTENTS

LIST OF TABLES

Table **Page**

LIST OF FIGURES

CHAPTER 1

INTRODUCTION

1.1 Motivation

Since its inception in the 1960s, the Global Positioning System has developed from a military navigational system to a widespread commercial service. Policy makers have had to address trade-offs between commercial and national security interests since 1983 when the decision was made to make GPS available to commercial industries such as aviation and surveying [1]. As a result, GPS signal characteristics, such as the carrier frequencies and bandwidths, are well known to consumers as well as hostile actors, making GPS receivers vulnerable to attack.

GPS signals originate from satellite vehicles in medium earth orbit, ∼20,200 km above the earth's surface, and the power available to terrestrial users is low, on the order of -130 dBm [2]. Terrestrial users estimate the approximate distances or pseudoranges to multiple satellites to infer their position. These estimates depend on acquiring and tracking very weak signals which can easily be overwhelmed by in band interference. Because of the already low signal power and the well known spectral characteristics, it is possible for an adversary to intentionally introduce RF interference into the GPS frequency bands, referred to as jamming, and deny the user position, navigation, and timing (PNT) data.

The effects of both intentional jamming and unintentional RF interference may be reduced by the GPS receivers antenna reception pattern. A reception pattern which has high gain directed towards satellites and low gain towards sources of interference will reduce the jammer to signal ratio compared to an isoptropic antenna. In cases where the GPS receiver is stationary and the interference is assumed to come from low elevations, a fixed reception

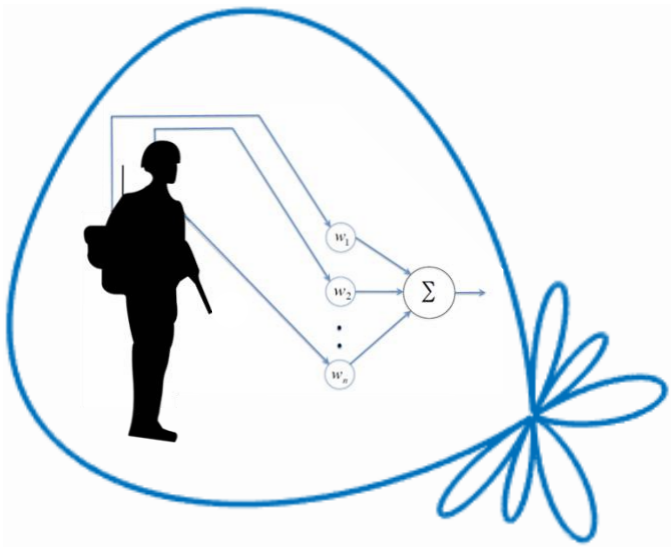

Figure 1.1: Man-portable CRPA concept.

pattern antenna (FRPA) may be employed to reduce gain at the horizon by at least 35 dB compared to zenith [3]. However, for man-portable applications such as a GPS receiver for a dismounted soldier, the receiver orientation and location will dynamically change and the reception pattern must adapt with the changing interference environment. A controlled reception pattern antenna (CRPA) [4] is a device that combines time-delayed and scaled received signals on multiple antenna elements to dynamically alter the reception pattern, placing pattern nulls in the angle-of-arrival of a hostile interference source, or jammer. Adaptive algorithms are used to control the complex-valued weights that are applied to each antenna to alter the reception pattern based on received signal statistics [5]. The number of independent jammers which can be mitigated by a particular CRPA design is limited by the number of elements used in that design's construction. In general, a CRPA comprising N elements has $N-1$ degrees of freedom which may be employed to cancel $N-1$ jammers.

Anti-jam GPS CRPAs have been studied for large platforms such as aircraft before [6], however no solutions for dismounted soldiers currently exist. There is a need for a robust anti-jam system capable of allowing ground troops to maintain PNT service in congested and contested environments. However, a man-portable CRPA introduces unique design challenges, such as battery requirements which substantially limit processing power and

hardware, necessitating an efficient, low-power design. Additionally, the size, weight, and power (SWAP) constraints limit the number of CRPA elements that could be used, reducing the spatial degrees of freedom. For a given number of antenna elements, additional degrees of freedom can be introduced by utilizing dual-polarized antennas, or tapped delay lines [7]. However, both of these methods increases the power demands by either doubling the number of RF channels or requiring a larger digital processor, respectively.

Degrees of freedom outside of the spatial domain are of interest, as the number of pattern nulls is limited by the number of antenna elements, and physical propagation environments often present multiple paths for electromagnetic waves between antennas [8]. In a multipath environment, a single jammer reflecting off objects in the surrounding medium can present wavefronts from multiple directions to a CRPA, and may exhaust a CRPA's degrees of freedom. Analytic and physical channel models have been developed for various multipath environments [9], though their application to null steering has not been reported. The effects of GPS multipath components on receiver performance has been studied with an emphasis on the errors introduced into the receiver [10], but multipath considerations for jammers have not been explored. The characterization of an anti-jam CRPA in multipath environments is necessary to inform design choices, such as the necessary number of elements and the inclusion of dual-polarized elements or STAP techniques to meet the needs of today's warfighter.

1.2 Related Work

Spatial filtering in antenna arrays with the use of adaptive algorithms is a mature field [11–14] and investigations into adding degrees of freedom outside of the spatial domain have been performed. Polarimetric techniques can be employed to introduce degrees of freedom in the polarization domain [15–18]. CRPA elements with two orthogonal ports, such as dual-linear antennas have been reported to cancel jammers without increasing the CRPA footprint. Time domain degrees of freedom may be introduced with tapped delay lines, a technique referred to as space-time adaptive processing (STAP) [19–21]. Similarly, with multiple samples from each antenna, Fourier transforms have been used on data from

each antenna for space-frequency array processing (SFAP) [23, 24]. The real-time Fourier transforms are computationally intensive, making SFAP a poor candidate for the current purpose. Each of these techniques increases the complexity of a CRPA, whether through introducing additional hardware, requiring larger processors, or both.

Investigations into non-planar CRPA configurations [25,26] and flexible textile antennas [27] have also been performed, as have models with limited degrees of freedom [28,29]. Small conformal arrays differ from larger phased arrays, and concepts such as a array factors are of limited use for arrays comprising a small number of elements with diverse element patterns [30].

Multipath environments have been studied, and a large body of propagation models exists, primarily for use in communications engineering. It is common practice to classify propagation models into one of two categories, these being physical and analytic [8, 31], where physical models aim to incorporate the electromagnetic characteristics and analytic models are based on assumptions about the impulse response of the channel. Analytic models may be developed to include many effects, such as polarization [32], however they do not capture the complete electromagnetic environment. Some physical models rely on geometrical assumptions about the locations of scattering objects [33,34]. Several standardized models incorporate measured results for specific frequency bands and types of environments. The model presented in Chapters 4 and 5 is best described as a physical model.

Additionally, work has been done in the domain of direction-of-arrival estimation in multipath environments under assumptions of coherent and incoherent scattering [35–37]. For the direction finding problem, coherency between incoming signals presents challenges and introduces estimation errors [38]. On the contrary, coherence in the jamming problem can actually improve CRPA performance as will be shown in Chapter 4. The gaps identified above must be addressed to successfully design a man portable system.

1.3 Organization and Contributions

Considerations for a man-portable anti-jam GPS receiver differ from previous anti-jam efforts in two crucial ways. First, greater SWAP constraints exist for man-portable systems.

These constraints put a limit on the degrees of freedom available for jammer mitigation. Second, the operating environment will likely put the CRPA low to the ground and in close proximity to many scattering objects, making multipath a larger concern than for aircraft or vehicle mounted systems. The communications and multiple-input multiple-output (MIMO) literature often relies on analytic models for multipath environments divorced from electromagnetic considerations. This work aims to comprehensively address the jamming problem in realistic electromagnetic environments and inform the design considerations for a SWAP constrained anti-jam GPS CRPA.

This document is structured as follows: Chapter 2 provides background on the algorithms available for null-steering as well as GPS satellite coverage and the electromagnetic environments. Following this discussion, multipath channel models represented from the literature are outlined. Chapter 3 provides the modeling techniques used in simulating CRPA operation in a line-of-sight environment. The strengths and uses of each of these techniques are highlighted and the accuracy of predictions made with either are compared. The chapter closes with anechoic chamber measurements of synthesized nulls. A scattering model which includes both specular and diffuse reflection is introduced in Chapter 4. This model is used to analyze the spectral characteristics of the partial covariance matrices under different scattering assumptions. A synthesized time-domain scattering example is then provided showing agreement with the previous results. Chapter 5 expands the mixed scattering model to include polarization effects and also investigates STAP techniques for mitigating wideband jammers. Two STAP constraints are presented and compared, and a key strength of STAP over other techniques is demonstrated, this being the ability to mitigate wide band interference. Finally, Chapter 6 summarizes the conclusions drawn from this work.

Some of the work contained herein has been presented in conference [39–42] and has led to one journal paper [43]. The novel contributions of this work are:

1. The verification process described in Section 3.3.1. A need arose to confirm the null-steering suite generated in MATLAB using commercially available full-wave electromagnetic software. However, the specific requirements, viz. control over current

excitations, were not supported for that specific model. Therefore, a method involving non-radiating networks and S-parameter renormalization was developed to confirm the null-steering predictions of other models.

2. The specular reflection factor defined in Section 4.3. A parameter, ς, is introduced and used to balance between specular and diffuse reflection from a scattering object. Objects in a multipath environment are modeled having both specular and diffuse properties, with the relative power in each of these controlled by ς. This differs from the Ricean fading factor, K, in that the latter is the ratio of line-of-sight to scattered power, whereas ς has no effect on the line of sight component and instead controls the relative power in coherent and incoherently scattered waves.

3. The analysis of the eigenvalues of partial covariance matrices in chapter 4. The structure of the signal covariance matrix, $\mathbf{R}$, has been documented in the literature, in particular for subspace decomposition methods for direction finding. However, this analysis focuses on the eigenvalues in the signal space alone, and how they relate to specular and diffuse scattering.

4. The application of the scattering matrix, $\mathbf{\Gamma}$, of the form of (5.4) to the null-steering problem. Similar forms of $\mathbf{\Gamma}$ have been used to characterize bulk material for passive and active radiometry. However, a matrix of this form has not been randomly parameterized and used for investigations into anti-jam CRPAs prior to this.

5. The comparison between the two STAP constraints in Section 5.2.1. Many STAP applications assume known steering vectors. The blind null-steering problem, i.e. canceling interference with no estimate of the directions to the desired signals, requires only that a single reference element remain on. The two constraints in this work assume no known steering vectors, and differ in that one adds multiple signals at the desired frequency coherently.

The following pages lay out flexible techniques for modeling anti-jam CRPAs in dynamic electromagnetic environments. Methods for efficiently simulating CRPA geometries are described and compared with higher fidelity full-wave modeling methods. Additionally, a

parametric physical channel model is outlined which can be modified for different assumed terrains and environmental objects.

Increasing the degrees of freedom of a CRPA is essential for man-portable application, therefore polarimetric and STAP CRPAs are considered. Given the SWAP limitations and multipath considerations of a man-portable CRPA, this work argues for the use of STAP over dual-linear elements as a method for increasing degrees of freedom and overall CRPA performance. Polarimetric methods require a greater amount of hardware, increased power and weight, and do not offer the same benefits of STAP. Conversely, time samples can be implemented digitally and have an advantage over polarimetric techniques in mitigating wide band jammers. The coming discussion will elucidate these claims, but first the necessary foundations must be laid out. With that, attention is now turned to null-steering algorithms and electromagnetic considerations.

CHAPTER 2

BACKGROUND

2.1 Adaptive Null-Steering Algorithms

For a CRPA comprising multiple antenna elements, the received signals present at each antenna port may be arranged as a column vector, $\mathbf{x}$. The port voltage on the ith port, $[\mathbf{x}]_i$, comprises GPS signals, Gaussian noise, and any interfering signals present. The CRPA output, y, is a weighted sum of of the port voltages,

$$y = \mathbf{w}^{\dagger}\mathbf{x}, \tag{2.1}$$

where $\{\bullet\}^{\dagger}$ denotes the conjugate transpose. The weight vector, $\mathbf{w}$, comprises the complex conjugates of the applied weight coefficients used to find y. Jamming is mitigated by trying to solve a minimization problem, namely minimizing the output power

$$\|y\|^2 = \mathrm{E}\left[\mathbf{w}^{\dagger}\mathbf{x}\mathbf{x}^{\dagger}\mathbf{w}\right] = \mathbf{w}^{\dagger}\mathbf{R}\mathbf{w}, \tag{2.2}$$

where $\mathrm{E}[\bullet]$ denotes the expectation operator and $\mathbf{R} = \mathrm{E}\left[\mathbf{x}\mathbf{x}^{\dagger}\right]$ is the covariance matrix of the received vector $\mathbf{x}$. The linearly constrained minimization problem is subject to the constraint,

$$\mathbf{w}^{\dagger}\mathbf{e} = c, \tag{2.3}$$

where $\mathbf{e}$ is the constraint vector and c is a constant, say $c = 1$. Different values of $\mathbf{e}$ may be used to achieve different goals, e.g., $\mathbf{e}$ can be selected as the steering vector in the direction

of the desired signal,

$$[\mathbf{e}]_i = [\boldsymbol{\psi}]_i \frac{1}{\sqrt{N}} e^{jk(x_i \sin\theta \cos\phi + y_i \sin\theta \sin\phi + z_i \cos\theta)}. \tag{2.4}$$

In this case, referred to as Capon beamforming [52], the goal is to maintain unit gain in the direction of a desired signal, given by (θ, ϕ). However, when the CRPA is subject to the dynamic orientation changes anticipated for a man-portable system deployed in the field, the steering vector will constantly change. Knowledge of the bearings to GPS satellite vehicles (SVs) is not readily available or easily estimated under dynamic orientation changes. Inertial data and feedback from the GPS receiver could be used to overcome this limitation with considerable computational resources, though this is beyond the scope of this work, which considers a modular system designed to work with existing receivers. Selecting $\mathbf{e} = [1, 0, 0, ..., 0]^T$, sometimes referred to as power inversion, sets a reference element, or individual antenna, which will always be weighted with a value of 1. The remaining antenna elements are then used to cancel interference impinging on the CRPA from different directions, leaving the low-power GPS signals unaffected by adaptive nulling over much of the visible region. Another useful method is to employ a CRPA comprised of dual-linear elements, i.e. two co-located LP antennas, and choose $\mathbf{e} = [1, -j, 0, ..., 0]^\dagger$ to maintain a synthesized CP reception pattern [16].

In all these cases, the optimal weight vector is given by

$$\mathbf{w} = \frac{\mathbf{R}^{-1}\mathbf{e}}{\mathbf{e}^\dagger \mathbf{R}^{-1}\mathbf{e}}, \tag{2.5}$$

which is found using Lagrange multipliers [53]. Lagrange multipliers are used to optimize a real-valued function of complex variables subject to one or more linear constraints. Geometrically, equation (2.5) finds the minimum point in the intersection of a convex surface and plane.

The Lagrangian, H, is defined in terms of the constraining function, g, the cost function, f, and the Lagrange multiplier, λ,

$$H(\mathbf{w}) = f(\mathbf{w}) + \lambda\, g(\mathbf{w}). \tag{2.6}$$

Critical points of H occur when the gradient of H vanishes, or equivalently when ∇f is parallel to ∇g with a proportionality constant of λ. If the cost function is complex valued, the real-valued Lagrangian is defined in terms of a complex Lagrange multiplier,

$$H = f + \mathrm{Re}\left[2\lambda^* g\right] = f + \left(\lambda^* g + g^* \lambda\right). \tag{2.7}$$

Multiple constraints determined by a system of equations with different Lagrange multipliers for each constraining function can be written in vector notation as

$$H(\mathbf{w}) = f(\mathbf{w}) + \boldsymbol{\lambda}^\dagger \mathbf{g}(\mathbf{w}) + \boldsymbol{\lambda}^T \mathbf{g}^*(\mathbf{w}). \tag{2.8}$$

The gradient with respect to $\mathbf{w}$ is defined by

$$[\nabla H]_i = \frac{\partial H}{\partial w_i^*} = \frac{1}{2}\left[\frac{\partial H}{\partial u_i} + j\frac{\partial H}{\partial v_i}\right], \tag{2.9}$$

where u_i and v_i denote the real and imaginary components of w_i, respectively. The cost function, f, is the output power of the CRPA given by (2.2), the gradient of which is

$$\nabla_{\mathbf{w}} f(\mathbf{w}) = \nabla_{\mathbf{w}} \mathbf{w}^\dagger \mathbf{R}\mathbf{w} = \mathbf{R}\mathbf{w}. \tag{2.10}$$

For multiple constraints on the $M \times 1$ weight vector, as in (2.8), consider the system of N linear equations

$$\mathbf{C}\mathbf{w} = \mathbf{c}, \tag{2.11}$$

where $\mathbf{C}$ is a $N \times M$ matrix, $\mathbf{c}$ is a $N \times 1$ vector, and the system of constraining functions is defined by

$$\mathbf{g}(\mathbf{w}) = \mathbf{C}\mathbf{w} - \mathbf{c}. \tag{2.12}$$

Combining this with (2.8) and taking the gradient gives

$$\nabla_{\mathbf{w}} H(\mathbf{w}) = \nabla_{\mathbf{w}} \left(f(\mathbf{w}) + \boldsymbol{\lambda}^\dagger \mathbf{g}(\mathbf{w}) + \boldsymbol{\lambda}^T \mathbf{g}^*(\mathbf{w})\right) = \mathbf{R}\mathbf{w} + \mathbf{C}^\dagger \boldsymbol{\lambda}. \tag{2.13}$$

Expressions for $\mathbf{w}$ and $\boldsymbol{\lambda}$ are obtained by setting (2.13) to zero and substituting this into

(2.11) to obtain

$$\mathbf{w} = \mathbf{R}^{-1}\mathbf{C}^{\dagger}\boldsymbol{\lambda}\ ,\ \ \left(\mathbf{C}\mathbf{R}^{-1}\mathbf{C}^{\dagger}\right)^{-1}\mathbf{c} = \boldsymbol{\lambda}. \tag{2.14}$$

For the $N = 1$ case of (2.3), the single constraint vector $\mathbf{e}$ replaces $\mathbf{C}^{\dagger}$ and (2.5) is recovered.

Additional degrees of freedom in the time-domain may also be introduced by taking $\mathbf{x}$ to be a $MN \times 1$ vector comprising M time samples of the N antenna element ports. This is referred to as STAP, which is discussed in more detail in Sections 2.2 and 5.2.

2.1.1 Sample Matrix Inversion

If $\mathbf{R}$ is known, the optimal weights can be found from (2.5), however $\mathbf{R}$ often must be estimated from observations of $\mathbf{x}$. This is done by taking an average value over some number of samples

$$\hat{\mathbf{R}} = \sum_{n=1}^{N} \mathbf{x}(n)\mathbf{x}^{\dagger}(n). \tag{2.15}$$

If $\mathbf{R}$ is stationary, only one matrix inversion is necessary, however a dynamically oriented CRPA will not have a stationary covariance matrix and multiple inversion are necessary. A windowed average may be employed in which

$$\hat{\mathbf{R}}(t) = \sum_{n=t-N}^{t} \mathbf{x}(n)\mathbf{x}^{\dagger}(n), \tag{2.16}$$

though this requires some decisions on how long of a window to use to balance the changing $\mathbf{R}$ and the computational resources required to perform multiple matrix inversions.

2.1.2 Conjugate Gradient Method

The Conjugate Gradient (CG) Method is a variation of the steepest descent method that can be used for solving systems of linear equations of the form $\mathbf{A}\mathbf{x} = \mathbf{b}$. Setting (2.13) for the single constraint case to zero gives just such a system, $\mathbf{R}\mathbf{w} = \mathbf{e}$. The theory behind CG is to take steps in directions, $\mathbf{d}_i$, that are $\mathbf{R}$-conjugate, or orthogonal after being transformed by $\mathbf{R}$,

$$\mathbf{d}_i^{\dagger}\mathbf{R}\mathbf{d}_j = \delta_j^i, \tag{2.17}$$

where $\delta_j^i = 1$ if $i = j$ and 0 otherwise. Stepping in this way, CG arrives at a solution that minimizes $\mathbf{Rw} - \mathbf{e}$ for a system of N equations in N steps or fewer [56]. The basic CG algorithm [57] works on a symmetric positive definite matrix $\mathbf{A}$, but extension to a Hermitian matrix $\mathbf{R}$ is straightforward [58].

Following an initial guess of $\mathbf{w}(0)$, CG is applied by taking steps along different search directions, $\mathbf{d}(i)$, by a step size of $\alpha(i)$. The first search direction is chosen to be the residual, $\mathbf{r}(i) = \mathbf{e}(i) - \mathbf{Rw}(i)$, at time $i = 0$. The step size is chosen to remove the portion of the error term $\mathbf{e}(i) = \mathbf{w} - \mathbf{w}(i)$ parallel to $\mathbf{d}(i)$. The next search direction is chosen from the conjugate Gram-Schmidt process. The equations for CG are as follows:

$$\boxed{\begin{aligned} \mathbf{d}(0) &= \mathbf{r}(0) = \mathbf{e}(0) - \mathbf{Rw}(0), \\ \alpha(i) &= \tfrac{\mathbf{r}^\dagger(i)\mathbf{r}(i)}{\mathbf{d}^\dagger(i)\mathbf{Rd}(i)}, \\ \mathbf{w}(i+1) &= \mathbf{w}(i) + \alpha(i)\mathbf{d}(i), \\ \mathbf{r}(i+1) &= \mathbf{r}(i) - \alpha(i)\mathbf{Rd}(i), \\ \beta(i+1) &= \tfrac{\mathbf{r}^\dagger(i+1)\mathbf{r}(i+1)}{\mathbf{r}^\dagger(i)\mathbf{r}(i)}, \\ \mathbf{d}(i+1) &= \mathbf{r}(i+1) + \beta(i+1)\mathbf{d}(i). \end{aligned}} \tag{2.18}$$

Here, $\beta(i+1)$ is the Gram-Shmidt constant at time $i+1$. An initial guess of $\mathbf{w}(0) = \mathbf{e}$ is an adequate starting place and will converge in $i \leq N$ steps. The weight vectors produced from (2.5) and (2.18) are linearly dependent and differ only by a scalar factor.

The Conjugate Gradient Method has seen much use in solving systems where N is large and is adept at handling sparse matrices in fewer than N steps. CG also works under the assumption that $\mathbf{R}$ is known [59]. With a non-stationary $\mathbf{R}$ and small N, as in the man-portable CRPA case, CG is not an obvious choice.

Linear constraints and uncertainty in $\mathbf{R}$ may be included in CG by a modified implementation of a generalized sidelobe canceler (GSC). It is possible to construct a GSC that is equivalent to the linearly constrained Frost's Algorithm described below [13]. Starting from this GSC structure it is possible to derive a linearly constrained CG algorithm which converges to the same weight vector more rapidly [60]. This method also estimates the

covariance matrix using an exponentially weighted average,

$$\hat{\mathbf{R}}(i) = \gamma\hat{\mathbf{R}}(i-1) + (\mathbf{P}\mathbf{x}(i))\,(\mathbf{P}\mathbf{x}(i))^{\dagger}\,, \tag{2.19}$$

where $\mathbf{P}$ is the same projection matrix defined below in (2.27). The constrained CG method addresses both the linear constraints and the uncertainty in $\mathbf{R}$ mentioned above, and shows promising convergence rates. However, this method requires far more mathematical operations per update, and an implementation that meets the SWAP constraints of this work would introduce difficult challenges.

2.1.3 Gradient Descent: Frost's Algorithm

Frost developed an iterative algorithm which generates the weight vector at time $k+1$ by moving in the opposite direction of the gradient away from the weight vector at time k,

$$\mathbf{w}_{k+1} = \mathbf{w}_k - \mu\nabla_{\mathbf{w}}H(\mathbf{w}) = \mathbf{w}_k - \mu\left(\mathbf{R}\mathbf{w}_k + \mathbf{C}^{\dagger}\boldsymbol{\lambda}\right). \tag{2.20}$$

By enforcing the constraining equations on the updated weight vector,

$$\mathbf{c} = \mathbf{C}\mathbf{w}_{k+1} = \mathbf{C}\left(\mathbf{w}_k - \mu\nabla_{\mathbf{w}}H(\mathbf{w})\right) = \mathbf{C}\left(\mathbf{w}_k - \mu\left(\mathbf{R}\mathbf{w}_k + \mathbf{C}^{\dagger}\boldsymbol{\lambda}\right)\right), \tag{2.21}$$

an expression for the Lagrange multipliers is obtained,

$$\boldsymbol{\lambda} = \frac{-1}{\mu}\left(\mathbf{C}\mathbf{C}^{\dagger}\right)^{-1}\left(\mathbf{C}\mathbf{w}_k - \mu\mathbf{C}\mathbf{R}\mathbf{w}_k - \mathbf{c}\right). \tag{2.22}$$

Plugging this back into (2.20) leads to

$$\mathbf{w}_{k+1} = \mathbf{w}_k - \mu\mathbf{R}\mathbf{w}_k - \mathbf{C}^{\dagger}\left(\mathbf{C}\mathbf{C}^{\dagger}\right)^{-1}\mathbf{C}\mathbf{w}_k + \mathbf{C}^{\dagger}\left(\mathbf{C}\mathbf{C}^{\dagger}\right)^{-1}\mathbf{C}\mu\mathbf{R}\mathbf{w}_k + \mathbf{C}^{\dagger}\left(\mathbf{C}\mathbf{C}^{\dagger}\right)^{-1}\mathbf{c}. \tag{2.23}$$

The projection matrix, $\mathbf{P}$, and initialization weight, $\mathbf{w}_0$, are defined as

$$\mathbf{P} = \mathbf{I} - \mathbf{C}^{\dagger}\left(\mathbf{C}\mathbf{C}^{\dagger}\right)^{-1}\mathbf{C}\ ,\ \mathbf{w}_0 = \mathbf{C}^{\dagger}\left(\mathbf{C}\mathbf{C}^{\dagger}\right)^{-1}\mathbf{c}, \tag{2.24}$$

to obtain

$$\mathbf{w}_{k+1} = \mathbf{w}_0 + \mathbf{P}\left[\mathbf{w}_k - \mu\mathbf{R}\mathbf{w}_k\right]. \tag{2.25}$$

In practice, the covariance matrix $\mathbf{R}$ is not known, and so an estimate must be introduced. Frost proposed a single sample estimate from the previous received vector

$$\hat{\mathbf{R}}_k = \mathbf{x}_k\mathbf{x}_k^\dagger. \tag{2.26}$$

For the $N = 1$ dimensional constraint system of (2.3), $\mathbf{P}$ and $\mathbf{w}_0$ of (2.24) become

$$\mathbf{P} = \mathbf{I} - \frac{\mathbf{e}\mathbf{e}^\dagger}{\|\mathbf{e}\|^2}\ ,\ \mathbf{w}_0 = \frac{\mathbf{e}}{\|\mathbf{e}\|^2}c\ . \tag{2.27}$$

Using the single sample estimate of (2.26), and choosing $c = 1$ and a normalized constraint vector ($\|\mathbf{e}\| = 1$) results in

$$\mathbf{w}_{k+1} = \mathbf{e} + \mathbf{P}\left[\mathbf{w}_k - \mu\mathbf{x}_k y_k^*\right]. \tag{2.28}$$

2.1.4 Gradient Descent: LMS

The LMS algorithm minimizes the mean square error between the desired signal d_k and the received vector $\mathbf{x}_k$ by gradient descent. The weights at time k applied to $\mathbf{x}_k$ provide an estimate for the desired signal, $\hat{d}_k$, and the error, ε_k, is defined as the difference between the desired signal and the estimate,

$$\varepsilon_k = d_k - \hat{d}_k = d_k - \mathbf{w}_k^\dagger\mathbf{x}_k. \tag{2.29}$$

The LMS algorithm is derived by setting up a steepest descent search for the weight vector,

$$\mathbf{w}_{k+1} = \mathbf{w}_k - \mu\nabla_{\mathbf{w}}\|\varepsilon_k\|^2, \tag{2.30}$$

and choosing as an estimate for the gradient,

$$\widehat{\nabla}_{\mathbf{w}}\|\varepsilon_k\|^2 = \varepsilon_k\mathbf{x}_k^*. \tag{2.31}$$

Note that when the gradient is zero, the error is orthogonal to the received vector. Plugging this into (2.30) yields the LMS weight update equation

$$\mathbf{w}_{k+1} = \mathbf{w}_k - \mu\varepsilon_k\mathbf{x}_k^* = \mathbf{w}_k - \mu\left[d_k\mathbf{x}_k^* - \left(\mathbf{x}_k\mathbf{x}_k\mathbf{w}_k\right)^*\right]. \tag{2.32}$$

This algorithm requires the generation of a desired signal for comparison with the received vector, which adds to the complexity of its implementation. The LMS algorithm also can exhibit drift over time from errors due to finite precision arithmetic, eventually reaching a state that no longer satisfies (2.3) [61]. This is not a large concern on modern computers, but the issue can arise for embedded systems which use fixed point representations of numbers and have power requirements which increase with the system precision. Given the SWAP constraints of this work, Frost's Algorithm is the preferred, simpler option.

2.2 Space Time Adaptive Processing Overview

Two techniques which utilize multiple time samples from each CRPA element to mitigate wide band interference are STAP and space-frequency adaptive processing (SFAP). Unlike space-only array processing, the nulls produced from STAP and SFAP span a larger frequency band and are not solely dependent on the phase differences of the jammer sampled at different point in space. Additionally, for an N element array with $M-1$ tapped delay lines added, the number of degrees of freedom increases to $MN-1$. However, the phase response of a STAP CRPA at GPS frequencies can introduce bias into the GPS receiver's position estimate [19].

There is an additional computational load for SFAP compared to STAP, as processing occurs in the frequency domain and real-time Fourier transforms are necessary. Additionally, for a SFAP system to be equivalent to a corresponding STAP system, overlapping traces must be employed [24]. These factors indicate that SFAP is not the preferred method for man-portable applications.

The STAP CRPA input vector, $\mathbf{x}(k)$, includes samples of the received voltages on the N ports at time k, as well as the previous $M-1$. Time domain degrees of freedom allow for

the cancellation of wideband jammers, as will be seen is Section 5.2, as well as frequency selective filtering. Because of this, STAP is widely used in radar applications [62]. If a radar with a fixed position is assumed, the waves launched by the radar and reflected by stationary objects in the environment will return at the same center frequency with which they originated. Moving objects, on the other hand, will induce a Doppler shift on the returning waveform, and reflections from different types of objects can be discriminated in frequency. In this way, clutter, or stationary environmental objects such as mountains, may be removed from the measurement. The same principles apply to moving radars, though relative velocities and Doppler shifts must be accounted for.

Suppression of clutter in the Doppler domain is advantageous for finding moving targets in uncontested environments, however, if jammers are present, clutter suppression can actually have an adverse effect by increasing the sidelobe [63]. Jammers with angles-of-arrival off the main beam deliver more power to the receiver because of the increased sidelobe level, resulting in worse performance. However, radars implementing some form of STAP are able to mitigate both the clutter and the jammer, due to the spatial degrees of freedom and the adaptive power minimization techniques.

The basic formulation for STAP techniques is identical to those considered above for the single time sample cases. In fact, the formulation of (2.28) originally presented in [64] assumed multiple tapped delay lines as part of the CRPA architecture. Additionally, the optimal STAP weights in terms of maximizing the signal to interference plus noise ratio (SINR) is found from (2.5) when $\mathbf{e}$ is the steering vector for a particular direction and at a particular frequency. Much research has been done to make STAP more computationally efficient for radar applications, as radars often comprise a large number of elements, including multi-stage STAP applied to sub-arrays and rank-reduction techniques [65]. However, for a CRPA with a small number of elements, these methods are neither practical nor necessary.

2.3 Satellite Coverage

GPS receivers work by simultaneously tracking the carrier phase of multiple GPS signals. Both GPS Coarse Acquisition (C/A) code and the military P(Y) code utilize binary

phase shift keying (BPSK) with chip rates of 1.023 MHz and 10.23 MHz respectively. Satellite ephemeris data, including satellite constellation positions and timing, are transmitted in a message signal at a rate of 50 Hz.

Each SV has a unique pseudorandom-noise (PRN) code, with low cross-correlation between codes and low autocorrelation between individual bits in the PRN sequence. A typical receiver generates three replica codes for each SV it is tracking, these being early, prompt, and late replicas. Code tracking loops integrate the product of these replicas with the received signal to find the correlation between the recieved signal and the replicas, and shift the replicas in time to maximize the prompt correlation. The amount of time by which these replicas are shifted is used to generate an estimate of the time delay and distance, or psuedorange, to a satellite. Four SVs are necessary for a position solution, but in practice receivers may track as many as 11 SVs for a more accurate solution.

Carrier tracking loops offer greater accuracy, especially when the receiver is moving, however these are also more susceptible to jamming [48]. When the carrier tracking loop is lost, the code tracking soon fails as well. This can be managed to some extent in receivers that utilize inertial measurement units (IMUs) to estimate receiver velocity, though this is not a current capability of the DAGR receiver used by soldiers in the field.

The GPS specification gives a minimum power level of -158.5 dBW for C/A code and -161.5 dBW for P(Y) code at the L1 frequency (1.57542 GHz) for SVs at an elevation of 5° or greater above the horizon [2]. These signals are transmitted with right hand circular polarization (RHCP) and that minimum power level is assumed to be uniform for all directions of arrival with elevation greater than 5°, though in practice it exceeds this value for many elevation angles. The received signal carrier power as a function of the angle of arrival, $C_s(\theta, \phi)$, depends on the CRPA reception pattern and polarization in that direction.

The CRPA elements are assumed to have white Gaussian noise present due to the ambient background temperature and thermal noise in the front end electronics. Jammer interference can be treated as equivalent additive Gaussian noise, and in doing so the

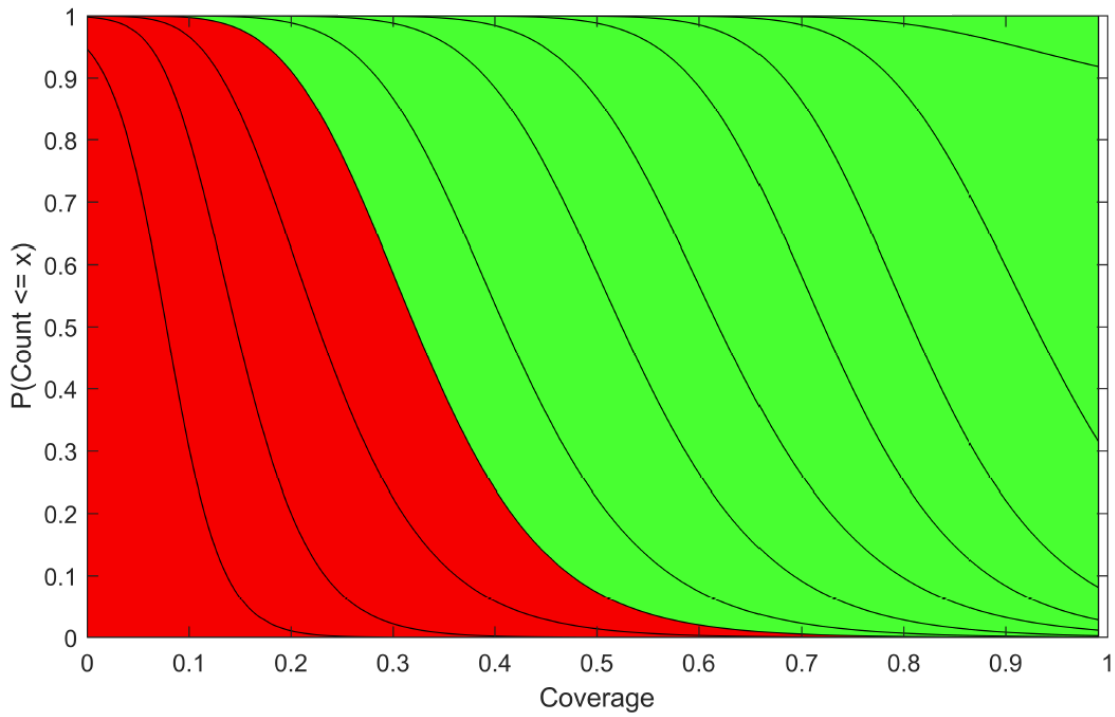

Figure 2.1: Probability of having fewer than x satellites in view as a function of satellite coverage for increasing values of x. Four satellites are necessary for an unambiguous position solution.

effective carrier to noise ratio is defined as [10],

$$(C_s/N_0)_{eff} = \left[\frac{N_0}{C_s} + \frac{C_j}{C_s Q R_c}\right]^{-1}, \tag{2.33}$$

where N_0 is the noise power in a 1 Hz bandwidth, Q is the jamming resistance quality factor (a function of the spectral correlation between the jammer and the GPS signal) and R_c is the chip rate of the PRN code, 1.023 MHz and 10.23 MHz for C/A and P(Y) code, respectively. Here, the jammer power, $C_j\left(\theta_j, \phi_j\right)$, depends on the jammer direction of arrival and may be expanded to include multiple jammers. The subscript $_{eff}$ will be dropped in further discussion of C_s/N_0 to simplify the notation. The GPS carrier tracking loops are able to maintain a lock, provided that C_s/N_0 exceeds a threshold of 28 dB-Hz in a typical receiver. Satellite coverage is defined as the portion of the sky with elevation angles greater than 5°

where C_s/N_0 exceeds this threshold,

$$\frac{\int_{\theta=0}^{85^\circ}\int_{\phi=0}^{360^\circ}[C_s/N_0 > 28]\sin\theta d\phi d\theta}{\int_{\theta=0}^{85^\circ}\int_{\phi=0}^{360^\circ}\sin\theta d\phi d\theta}. \tag{2.34}$$

The GPS constellation is designed so that multiple SVs will be in view regardless of the user's position on Earth, however it is desirable to translate between coverage and a metric of success. For this, the locations of SVs were estimated for an observer in Amherst, MA at varying times of day using a freely available online tool [67], and compared against multiple realizations of null-steering simulations in a jamming environment. A discrete count of satellites that were recoverable for a given time of day and a given jamming environment was recorded and a logistic regression between the count and satellite coverage was undertaken. Figure 2.1 shows the probability that the count is below $x \in [0, 10]$ for increasing values of coverage, with the red regions representing a failure (i.e., fewer than four SVs) and green representing success. Satellite coverage of 50 % translates to a probability of 0.95 for successfully tracking four SVs and generating a position solution.

2.4 Propagation Environment

Time harmonic electromagnetic fields are often expressed as phasors, where the relationship between the time-domain fields and the phasor-domain fields is [68]

$$\boldsymbol{\mathcal{E}}(\mathbf{r};t) = \mathrm{Re}\left[\mathbf{E}(\mathbf{r})e^{j\omega t}\right]. \tag{2.35}$$

Here, j is the imaginary unit, ω is the angular frequency, and $\mathbf{r}$ is the vector pointing from the origin to the observation point in space. If the electric field at a particular location has a magnitude $A(\mathbf{r})$, a phase $\alpha(\mathbf{r})$ and points in the $\hat{\boldsymbol{\rho}}(\mathbf{r})$ direction, (2.35) takes the form

$$\begin{aligned}\boldsymbol{\mathcal{E}}(\mathbf{r};t) &= \mathrm{Re}\left[A(\mathbf{r})\hat{\boldsymbol{\rho}}(\mathbf{r})e^{j\alpha(\mathbf{r})}e^{j\omega t}\right] \\ &= A(\mathbf{r})\Big(\mathrm{Re}\left[\hat{\boldsymbol{\rho}}(\mathbf{r})\right]\cos\left[\omega t + \alpha(\mathbf{r})\right] - \mathrm{Im}\left[\hat{\boldsymbol{\rho}}(\mathbf{r})\right]\sin\left[\omega t + \alpha(\mathbf{r})\right]\Big).\end{aligned} \tag{2.36}$$

In spherical coordinates, $\mathbf{r}$ consists of a radial component r, and angles $\theta \in [0, \pi]$ measured from the z axis and $\phi \in [0, 2\pi]$ measured from the x axis. An incoming jammer is often modeled as a plane wave defined by its angle-of-arrival (a term used to denote both the polar angle, θ_{j}, and azimuthal angle, ϕ_{j}) at the observation point $\mathbf{r} = [x, y, z]^T$,

$$\mathbf{E}_{\mathrm{j}} = A\hat{\boldsymbol{\rho}} e^{j\mathrm{k}_0\left(x \sin\theta_{\mathrm{j}} \cos\phi_{\mathrm{j}} + y \sin\theta_{\mathrm{j}} \sin\phi_{\mathrm{j}} + z \cos\theta_{\mathrm{j}}\right)}, \tag{2.37}$$

where $\mathrm{k}_0 = \frac{2\pi}{\lambda}$ is the wave number in free space. A plane wave has the property that the electric field observed at all points on a plane normal to the direction of propagation has the same phase. Polarization, given by $\hat{\boldsymbol{\rho}}$, describes the locus of points traced out by the electric field over time when observed from along the axis of propagation. Polarization is either linear, circular, or elliptical, and in the last two cases can rotate in a left-handed or right-handed sense. Linear polarized (LP) waves occur when the electric field points in a single direction, e.g.,

$$\hat{\boldsymbol{\rho}}_{\mathrm{LP}} = -\hat{\boldsymbol{\theta}}. \tag{2.38}$$

The electric field for circular polarized (CP) waves rotates in the plane normal to the direction of propagation, and maintains a constant magnitude, e.g.,

$$\hat{\boldsymbol{\rho}_{\mathrm{CP}}} = \frac{\hat{\boldsymbol{\theta}} - j\hat{\boldsymbol{\phi}}}{\sqrt{2}} \tag{2.39}$$

is the polarization vector for a right-hand circular-polarized (RHCP) wave traveling in the $\hat{\boldsymbol{r}}$ direction. Elliptical polarized (EP) waves are similar to CP waves, except that the electric field traces out a locus that is not a circle, due to either non-uniform magnitudes between $\hat{\boldsymbol{\theta}}$ and $\hat{\boldsymbol{\phi}}$ components, or a phase not equal to $\pm j$, or both.

Fields radiated by an antenna at sufficiently large distances can be approximated as plane waves, and the antenna polarization vector is determined by the polarization of these waves. The received power of an incoming plane wave on an antenna is determined by the polarization loss, given by the dot product of the polarization vectors, e.g., received power of an incident field with polarization vector (2.38) impinging on an antenna with polarization vector (2.39) will be a factor of $\|\hat{\boldsymbol{\rho}}_{\mathrm{LP}} \cdot \hat{\boldsymbol{\rho}}_{\mathrm{CP}}\|^2 = 0.5$ lower than the same field impinging on

an antenna with the same polarization. The received signal, x_i on the ith antenna element is a function of the element reception pattern toward the jammer angle-of-arrival and the plane wave value at the antenna center coordinates.

A plane wave incident on an antenna centered at the origin from a given angle-of-arrival will induce a voltage across the antenna terminals. The open circuit voltage for a given antenna and plane wave is a function of the antenna's vector effective height, $\mathbf{h}(\theta, \phi)$, which itself is found from the far-field radiation pattern of the antenna,

$$\mathbf{h} = \frac{4\pi}{j\mathrm{k}_0 \eta_0 I_{in}} \mathbf{E}^{rad} \ , \tag{2.40}$$

where η_0 is the free space impedance, and I_{in} is the input current to the antenna port corresponding to $\mathbf{E}^{rad}$. The open circuit voltage, v^{oc}, is found by taking the dot product of the incident field and the vector effective height,

$$v^{oc} = \mathbf{E}^{inc} \cdot \mathbf{h} \ . \tag{2.41}$$

Note that the dot product relates to the polarization vectors of the incident field and the antenna's radiated field, i.e. an incident field with orthogonal polarization to the antenna it illuminates will not induce a voltage on that antenna's ports.

It is typical to compute $\mathbf{h}$ for an antenna centered at the origin, however, a CRPA comprises multiple elements each with their own phase center. If the antenna is moved away from the origin to some point given by $\mathbf{r}_i$, and assuming the jammer is far away enough that the plane wave assumption holds, the received voltage will be phase-shifted by an amount ψ dependent on the position vector of the element and the direction of arrival,

$$\psi = \mathbf{k} \cdot \mathbf{r}_i = \mathrm{k}_0 \left(x_i \sin\theta \cos\phi + y_i \sin\theta \sin\phi + z_i \cos\theta \right) \ . \tag{2.42}$$

The new vector effective height, $\mathbf{h}'$, for an antenna element at $\mathbf{r}_i$ and phase referenced to the coordinate system origin is then,

$$\mathbf{h}' = \mathbf{h} \ e^{j\psi}. \tag{2.43}$$

When multiple antenna elements are located closely together in space, the current distribution on one element can induce a voltage at the ports of the adjacent elements. This is referred to as mutual coupling and has a greater effect when the antenna elements are in close proximity. Mutual coupling can be accounted for with the impedance parameter $\mathbf{Z}$ which incorporates each antenna's self impedance as well as its mutual impedance with all the other elements [72]. The port voltages due to adjacent currents are given by

$$\mathbf{v} = \mathbf{Z}\mathbf{i}, \tag{2.44}$$

where $\mathbf{v}$ and $\mathbf{i}$ are column vectors with the nth element being the port voltage or current, respectively, for the nth antenna element. If $\mathbf{Z}$ is not explicitly known, it can be found from the S-parameter [73],

$$\mathbf{Z} = \sqrt{z_0}\left(\mathbf{I}_{N\times N} + \mathbf{S}\right)\left(\mathbf{I}_{N\times N} - \mathbf{S}\right)\sqrt{z_0}\ . \tag{2.45}$$

The S-parameter relates incident and reflected voltage waves,

$$\mathbf{v}^{-} = \mathbf{S}\mathbf{v}^{+}. \tag{2.46}$$

Now, assuming each element is terminated with a load impedance z_L, the coupling matrix is defined as

$$\mathbf{A} = z_L\mathbf{I}_{N\times N}\left(z_L\mathbf{I}_{N\times N} + \mathbf{Z}\right)^{-1}, \tag{2.47}$$

which translates the open circuit voltage vector into a vector or received load voltages,

$$\mathbf{v}^{L} = \mathbf{A}\mathbf{v}^{oc}. \tag{2.48}$$

This is the form of the received signal and jammer vectors, which along with additive white Gaussian noise, are used in equation (2.1).

2.5 Jammer Statistics

The received voltage vector, $\mathbf{x}$, is assumed to comprise GPS signals, jammers, and additive white Gaussian noise,

$$\mathbf{x} = \sum_{p=1}^{S} \mathbf{x}_{s,p} + \sum_{q=1}^{J} \mathbf{x}_{j,q} + \mathbf{x}_N, \tag{2.49}$$

where the first subscript refers to the type of contribution (signal, jammer or noise) and the second subscript, if present, is the summation index. GPS signal power is on the order of -130 dBm, less than the noise power σ^2, and so can be safely neglected from the sum. The covariance matrix $\mathbf{R}$ in (2.1) has the form

$$\mathbf{R} = \mathrm{E}\left[\mathbf{x}\mathbf{x}^{\dagger}\right] = \mathrm{E}\left[\left(\sum_{q=1}^{J} \mathbf{x}_{j,q} + \mathbf{x}_N\right)\left(\sum_{q=1}^{J} \mathbf{x}_{j,q} + \mathbf{x}_N\right)^{\dagger}\right]. \tag{2.50}$$

The noise contribution is uncorrelated with all the jammers, i.e.

$$\mathrm{E}\left[\mathbf{x}_N \mathbf{x}_{j,q}^{\dagger}\right] = \mathrm{E}\left[\mathbf{x}_{j,q} \mathbf{x}_N^{\dagger}\right] = 0 \ , \ \forall \ q \ , \tag{2.51}$$

and the noise components across different ports are uncorrelated with one another,

$$\mathrm{E}\left[\mathbf{x}_N \mathbf{x}_N^{\dagger}\right] = \sigma^2 \mathbf{I}_{N\times N}, \tag{2.52}$$

where $\mathbf{I}_{N\times N}$ is the identity matrix. The received signals due to the jammers will be functions of the angles-of-arrival, the antenna element patterns, and possibly a random phase,

$$\mathbf{x}_{j,q} = \tilde{\mathbf{x}}_{j,q} e^{j\xi_q}. \tag{2.53}$$

Assuming independent identically distributed (i.i.d.) random phases, $\xi_q \sim \mathrm{U}\left[0, 2\pi\right]$, simplifies (2.50) because cross terms between distinct jammers cancel,

$$\mathrm{E}\left[\mathbf{x}_{j,p} \mathbf{x}_{j,q}^{\dagger}\right] = \tilde{\mathbf{x}}_{j,p} \tilde{\mathbf{x}}_{j,q}^{\dagger} \int_0^{2\pi} \int_0^{2\pi} \frac{e^{j(\xi_p - \xi_q)}}{4\pi^2} d\xi_p d\xi_q = \mathbf{0}. \tag{2.54}$$

This results in a covariance matrix with the form

$$\mathbf{R} = \sum_{p=1}^{J} \mathbf{x}_{j,p}\mathbf{x}_{j,p}^{\dagger} + \sigma^2 \mathbf{I}_{N\times N}. \tag{2.55}$$

The covariance matrix here is the sum of J rank-one Hermetian everywhere matrices and one full-rank Hermetian matrix. If there are fewer jammers than N antenna elements, then $\mathbf{R}$ has J eigenvectors due to the jammers and $N - J$ eigenvectors due to noise. Assuming the jammer power is larger than σ^2, the corresponding eigenvalues are large compared to the $N - J$ noise eigenvectors, and because $\mathbf{R}$ is full-rank Hermetian, its eigenvectors are orthogonal. This form of covariance matrix is well attested to in the literature and is the basis of subspace decomposition methods used in direction finding such as multiple signal classification (MUSIC) [74]. Now minimizing $\mathbf{w}^{\dagger}\mathbf{R}\mathbf{w}$ is analogous to finding a $\mathbf{w}$ that is orthogonal to the jammer eigenvectors. If $J > N$, this cannot be done. For this reason, an N element CRPA is said to have $N - 1$ degrees of freedom.

If jammer phases are instead assumed to be dependent and fixed, the covariance matrix is written as

$$\mathbf{R} = \sum_{p=1}^{J} \mathbf{x}_{j,p} \sum_{q=1}^{J} \mathbf{x}_{j,q}^{\dagger} + \sigma^2 \mathbf{I}_{N\times N} = \mathbf{x}'\mathbf{x}'^{\dagger} + \sigma^2 \mathbf{I}_{N\times N}. \tag{2.56}$$

In this instance, the jammer contribution to $\mathbf{R}$ is only a single rank-one Hermetian matrix. This seems to imply that the number of jammers is irrelevant if they are completely correlated. Of course, this would require coordination and phase locking between multiple jammers. In practice this seems unlikely, although strongly correlated fields at the CRPA may not exhaust the degrees of freedom as rapidly as in the independent case. Equations (2.55) and (2.56) are of interest because in a multipath environment it is possible that a single jammer may arrive at the CRPA from enough distinct angles to exhaust the degrees of freedom of a SWAP constrained CRPA, and the correlation between the multipath components may predict CRPA performance. Correlated sources have been studied terms of the direction finding problem, although this is in contrast to the present discussion [38]. Coherence between sources produces challenges to the direction finding problem and reduces the ability to accurately predict the directions of arrival, whereas coherence in the

null-steering problem may enable a CRPA to perform beyond its degrees of freedom.

2.6 Channel Models

The propagation channel is a term used to describe the environment in which electromagnetic waves travel in. This can include the effects of reflections from terrain or other objects as well as atmospheric effects. A wave originating from a single source will travel through the channel, and the resulting fields measured at the receiver can differ substantially from that of a simple plane wave in free space. Many physical phenomena can occur in the channel, including reflection of the waves from smooth surfaces, scattering from rough surfaces, diffraction around sharp corners, and diffraction through the intervening objects [75]. Herein, the term scattering will often be used to describe the total effect of the interactions between electromagnetic waves and objects in the channel.

Applied to the jamming problem, it is convenient to think of plane waves departing from the jammer in all directions, with varying magnitudes and phases determined by the jammer's radiation pattern. These waves will scatter off objects in the channel in all directions, with some portion of their energy directed towards the CRPA. All of the waves present at the CRPA will add, sometimes constructively and sometimes destructively, leading to a total observed electric field. If the channel is non-stationary, i.e. if the jammer, CRPA, or objects in the channel move relative to one another, then fading occurs at the CRPA. This is when the total fields at some point add destructively and the power decreases substantially. Fading is often described as fast-fading due to objects in close proximity to the receiver, and slow fading due to objects far away [76].

Fading at a single point will not, in general, be statistically correlated to fading of the fields at any other point. This is of great importance for a CRPA, as the separate CRPA elements are sampling the fields at different points, and these observation are being added coherently. To highlight this, consider the case with $N = 2$ CRPA elements, one of which is used as a reference. If the output at some time is given by

$$y = w_1^* x_1 + w_2^* x_2 = x_1 + w_2^* x_2, \tag{2.57}$$

and the magnitude of x_2 suddenly drops by several dB while $|x_1|$ remains constant, it is necessary that $|w_2|$ increases rapidly to account for this drop. The response time of the CRPA will have to be quick enough to account for this change, otherwise high levels of jammer power will slip through periodically and may disrupt PNT services. Additionally, the CRPA must be implemented in such a way that the magnitude of the weights has a high dynamic range, otherwise a deeply faded element will not have much effect on the overall output while its relative magnitude is small compared to the other elements. A channel in which fading between different elements is highly correlated will not experience the same impact from fading. If the relative magnitudes at the different elements remains relatively constant, the weight vector will remain reasonably stable.

Early channel models include the Rayleigh fading model, in which the channel lacked a direct line of sight between the transmitter and receiver [51]. Waves are assumed to come from all directions with equal probability in a Rayleigh channel, and the multiple uncorrelated paths add incoherently at the receiver. The extension of this model is Ricean fading, which also includes a line-of-sight component. In a Ricean channel, the power ratio of the power in the line-of-sight component to the power in the scattered components is set by the Ricean fading factor, K.

A need for an improved model arose from the empirical observation that scattered waves were often spatially correlated [9]. Many more recent models are defined in terms of the dual directional impulse response [8]. This response is the sum of all the contributions from different paths a wave may take between the transmission point, $\mathbf{r}_{tx}$, and reception point, $\mathbf{r}_{tx}$,

$$h(\mathbf{r}_{rx}, \mathbf{r}_{tx}, \tau, t, \Phi, \Psi) = \sum_{l=1}^{L} h^l(\mathbf{r}_{rx}, \mathbf{r}_{tx}, \tau, t, \Phi, \Psi). \tag{2.58}$$

Here Φ and Ψ denote the angle-of-departure from the transmitter and the angle-of-arrival for the receiver, respectively. The time variable τ refers to the delay along the traveled path and t is included for non-stationary channels, i.e. channels which have properties that change over time. This description of h accounts for the spatial channel only, though it can easily be expanded to include antenna patterns and frequency selective filtering.

For MIMO systems using multiple antennas at both the transmit and receive side, it

is common to define $h_{i,j}$ for each pair of transmit and receive antennas and organize them into a channel matrix, H. The channel matrix gives the relationship between an excitation at one end, $\mathbf{s}$, and the observation, $\mathbf{x}$, at the other,

$$\mathbf{x} = \mathbf{H}\mathbf{s} + \mathbf{n}, \tag{2.59}$$

where some additive noise is assumed.

The structure of $\mathbf{H}$ can define the channel properties, and much research has been done in this vein. Many models are commonly referred to as analytical models (as opposed to physical) which are abstractions of the propagation problem with some broad general characteristics. The simplest of these would be a channel matrix comprised of i.i.d. Gaussian random variables,

$$[\mathbf{H}_G]_{i,j} = h_{i,j} \sim \mathcal{N}\left(0, \sigma^2\right). \tag{2.60}$$

A matrix with this structure produces the familiar Rayleigh fading channel model. Spatial correlation between elements of the transmit and receive sides can be included into the channel model as well. One such model is the Kronecker model, which makes use of the spatial correlation matrices, $\mathbf{R}_{tx}$ and $\mathbf{R}_{rx}$, to include the array geometry into the channel. It should be noted that the correlation matrices here differ from the signal covariance matrices described in other sections; $\mathbf{R}_{tx}$ and $\mathbf{R}_{rx}$ are functions of the array structure at either end and do not depend on assumed signal characteristics. The Kronecker model further assumes that the channel covariance matrix is separable and expressible as the Kronecker matrix product,

$$\mathbf{R}_H = \mathbf{R}_{rx} \otimes \mathbf{R}_{tx}, \tag{2.61}$$

hence its name. By finding any matrices $\mathbf{R}_{tx,rx}^{1/2}$ satisfying

$$\mathbf{R}_{tx,rx}^{1/2}\mathbf{R}_{tx,rx}^{1/2} = \mathbf{R}_{tx,rx}, \tag{2.62}$$

the Kronecker channel matrix is given by [31]

$$\mathbf{H}_K = \mathbf{R}_{rx}^{1/2}\mathbf{H}_G\mathbf{R}_{tx}^{1/2}. \tag{2.63}$$

The obvious limitation to this channel model is that it includes structure of the arrays but none of the structure of the physical channel. To overcome this, the Weichselberger model was developed [77]. This model makes use of an assumed coupling matrix, $\mathbf{\Omega}$, which gives the average coupled power between transmit and receive elements. This and the eigendecompositions of the spatial correlation matrices, are used to find the channel matrix

$$\mathbf{H}_W = \mathbf{U}_{rx} \left(\mathbf{H}_G \odot \mathbf{\Omega} \right) \mathbf{U}_{tx}, \tag{2.64}$$

where $\odot$ is the Schur-Hadamard, or element-wise, product. The interested reader is directed to [77] for a full treatment of this subject, including variants not addressed here.

The Weichselberger channel model includes characteristics of the antenna elements as well as the propagation channel, assuming that the eigendecomposition of both transmit and receive arrays is attainable and the coupling matrix is known. In the absence of this knowledge assumptions must be made, and the physical realities of a given environment may not be perfectly modeled. For designed MIMO systems where an engineer has some control over both the transmit and receive ends[1] of the channel, characterization of these variables may be obtained through measurements of the antenna sites and simulation of the antennas on either side. However, the current purpose of this work is to characterize CRPA performance for combat operations. Jammer characteristics are unlikely to be well documented, and extensive measurement campaigns in contested areas are unlikely. For this reason, a physical model is preferred over an analytic one for this work, with enough control for defining the individual scattering objects in the CRPA's operational environment. This model is developed in Chapter 4 following development of the antenna modeling methods and measurements presented in Chapter 3.

[1] It should be noted that in modern communications systems, the transmit and receive distinction lacks some meaning as either node will be transmitting and receiving at different times.

CHAPTER 3

LINE-OF-SIGHT JAMMER MODELING METHODS AND MEASUREMENTS

The performance of a man-portable CRPA depends on the individual element patterns, element placements, and interactions between elements. Accurate simulations of CRPA constructions can be achieved with numerical electromagnetic software, however, these introduce heavy computational demands, and may not be appropriate for studies involving a large number of CRPA geometries. On-body distributed elements and hand-held units are of interest for man-portable applications. As such, a large number of constructions is possible. Additionally, the human body is not rigid and unchanging, unlike a vehicular or airframe platform. Changes in relative CRPA element orientation and placement are possible for the man-portable CRPA. Modeling small changes to a given construction requires efficient methods to consider many randomly perturbed variations of a baseline geometry.

In this chapter, techniques for efficiently simulating CRPA elements and geometries are developed, and the accuracy of these models is compared with a commercially available software package. Full-wave methods provide more realistic results than the translational methods outlined in Section 3.2 due to the inclusion of parasitic effects between elements. Yet, the computational demands are higher for full-wave solutions, and this constrains their application to problems involving several variants of similar arrays. The strengths of each of these methods are highlighted and compared before attention is turned to CRPA measurements in Section 3.4.

Results in this chapter are for idealized propagation conditions involving plane wave jammers incident from a single angle-of-arrival for each jammer. Propagation effects are

accounted for in later chapters, but the foundational techniques are presented here for a free-space environment first.

3.1 Analytic CRPA Model

Closed form analytic solutions are possible for some antenna geometries, and this can be a first step in obtaining CRPA element patterns for a model. As a starting point, vector effective heights for a dual-linear patch element similar to [16] are found using the cavity model, details of which are found in Chapter 14 of [71]. The CRPA elements are all assumed to be square patches with two ports, a horizontal or h-port which induces two effective magnetic currents oriented in the $\hat{y}$ direction, and a vertical, or v-port, which induces currents in the $-\hat{x}$ direction. With a patch side length of L and width of W, the radiated fields are of the form

$$\mathbf{E}_{h,\phi} = -\hat{\boldsymbol{\phi}}\ C\cos\theta\sin\phi\frac{\sin\left(\frac{\mathrm{k}_0 W}{2}\cos\theta\right)}{\frac{\mathrm{k}_0 W}{2}\cos\theta}\frac{\sin\left(\frac{\mathrm{k}_0 L}{2}\sin\theta\sin\phi\right)}{\frac{\mathrm{k}_0 L}{2}\sin\theta\sin\phi}\cos\left(\frac{\mathrm{k}_0 L_e}{2}\sin\theta\cos\phi\right),$$

$$\mathbf{E}_{h,\theta} = \hat{\boldsymbol{\theta}}\ C\cos\phi\frac{\sin\left(\frac{\mathrm{k}_0 W}{2}\cos\theta\right)}{\frac{\mathrm{k}_0 W}{2}\cos\theta}\frac{\sin\left(\frac{\mathrm{k}_0 L}{2}\sin\theta\sin\phi\right)}{\frac{\mathrm{k}_0 L}{2}\sin\theta\sin\phi}\cos\left(\frac{\mathrm{k}_0 L_e}{2}\sin\theta\cos\phi\right),$$

$$\mathbf{E}_{v,\phi} = \hat{\boldsymbol{\phi}}\ C\cos\theta\cos\phi\frac{\sin\left(\frac{\mathrm{k}_0 W}{2}\cos\theta\right)}{\frac{\mathrm{k}_0 W}{2}\cos\theta}\frac{\sin\left(\frac{\mathrm{k}_0 L}{2}\sin\theta\cos\phi\right)}{\frac{\mathrm{k}_0 L}{2}\sin\theta\cos\phi}\cos\left(\frac{\mathrm{k}_0 L_e}{2}\sin\theta\sin\phi\right),$$

$$\mathbf{E}_{v,\theta} = \hat{\boldsymbol{\theta}}\ C\sin\phi\frac{\sin\left(\frac{\mathrm{k}_0 W}{2}\cos\theta\right)}{\frac{\mathrm{k}_0 W}{2}\cos\theta}\frac{\sin\left(\frac{\mathrm{k}_0 L}{2}\sin\theta\cos\phi\right)}{\frac{\mathrm{k}_0 L}{2}\sin\theta\cos\phi}\cos\left(\frac{\mathrm{k}_0 L_e}{2}\sin\theta\sin\phi\right). \tag{3.1}$$

The radiated fields from these magnetic currents are used in (2.40) through (2.43), however mutual coupling is not accounted for at this stage.

The analytic formulation allows for easily modeling of dual-linear CRPAs with differing patch sizes and spacings by simply changing variables in the calculation. Null-steering is done for a jamming environment by finding $\mathbf{x}$ for a CRPA model and assumed jammer polarization and angles-of-arrival. Letting $\mathbf{E}_p^{inc}$ denote the incident field of the pth jammer,

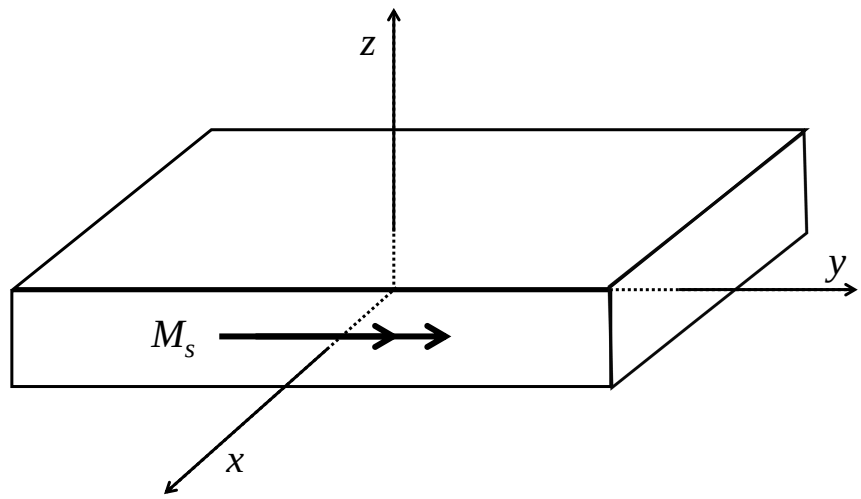

Figure 3.1: Patch antenna geometry for the cavity model, with equivalent magnetic current $\mathbf{M}_s$ due to excitation of the h-port.

the open circuit voltage for the nth CRPA port can be found from

$$\left[\mathbf{v}_p^{oc}\right]_n = \mathbf{h}_{v,n}^h e^{j\psi_n} \cdot \mathbf{E}_p^{inc}, \tag{3.2}$$

depending on whether port n is a horizontal or vertical port. A simplifying assumption of the port impedance and the load impedance may also be made, i.e. letting $z_{in} = z_L = 50\Omega$ gives a load voltage vector due to jammer p of

$$\mathbf{v}_p^L = \frac{\mathbf{v}_p^{oc}}{2}. \tag{3.3}$$

This is the received jammer vector, $\mathbf{x}_{j,p}$, of (2.50). Finding $\mathbf{R}$ for the two independent jammer case and using (2.5),

$$\mathbf{w} = \frac{\mathbf{R}^{-1}\mathbf{e}}{\mathbf{e}^\dagger \mathbf{R}^{-1}\mathbf{e}},$$

yields null-steering weights which will cancel two jammers. The jammer power after nulling, C_j, is found from the sum of the weighted jammer vectors,

$$C_j = \mathbf{w}^\dagger \left(\mathbf{x}_{j,1}\mathbf{x}_{j,1}^\dagger + \mathbf{x}_{j,2}\mathbf{x}_{j,2}^\dagger\right)\mathbf{w}, \tag{3.4}$$

assuming two independent jammers, and the noise power in a 1 Hz bandwidth after nulling is

$$N_0 = \mathbf{w}^\dagger N_0' \mathbf{w}. \tag{3.5}$$

Here, N_0' denotes the pre-nulling noise power density, which should not be confused with the noise power, σ^2, which is found by integrating N_0' over the receiver bandwidth. Typical values of $N_0' = -170.9$ dBm and $\sigma^2 = -99$ dBm are taken from [10].

To see the effect of jamming and null-steering on GPS coverage, the GPS signal power must also be computed. Let $\mathbf{x}_s(\theta, \phi)$ be the received GPS signal for $\theta \in [0, 85°]$ and $\phi \in [0, 360°]$. This can be calculated over the entire range by assuming an RHCP incident wave present from each angle-of-arrival with an amplitude set so that the minimum power requirement of -138.5 dBm for C/A code is met. The signal carrier power as a function of angle-of-arrival may be found from the null-steering weights,

$$C_s(\theta, \phi) = \mathbf{w}^\dagger \mathbf{x}_s(\theta, \phi) \mathbf{x}_s^\dagger(\theta, \phi) \mathbf{w}. \tag{3.6}$$

From here, the effective carrier to noise ratio may be computed over the region of interest, namely the sky, from (2.33),

$$C_s/N_0 = \left[\frac{N_0}{C_s} + \frac{C_j}{C_s Q R_c}\right]^{-1}.$$

Figures 3.2 and 3.3 show coverage maps for two CRPA geometries with four dual-linear elements. The color denotes C_s/N_0 which must exceed a threshold of 28 dB-Hz for $\mathbf{x}_s$ to be recoverable. The region $\theta \in [0, 85°]$ and $\phi \in [0, 360°]$ has been transformed into the u-v plane, where the transform

$$\begin{aligned} u &= \sqrt{2} \sin\tfrac{\theta}{2} \cos\phi, \\ v &= \sqrt{2} \sin\tfrac{\theta}{2} \sin\phi, \end{aligned} \tag{3.7}$$

is chosen so that the relative areas are preserved and the unit circle is the horizon. Note that these are not the direction cosines u and v that appear often in the literature and do not

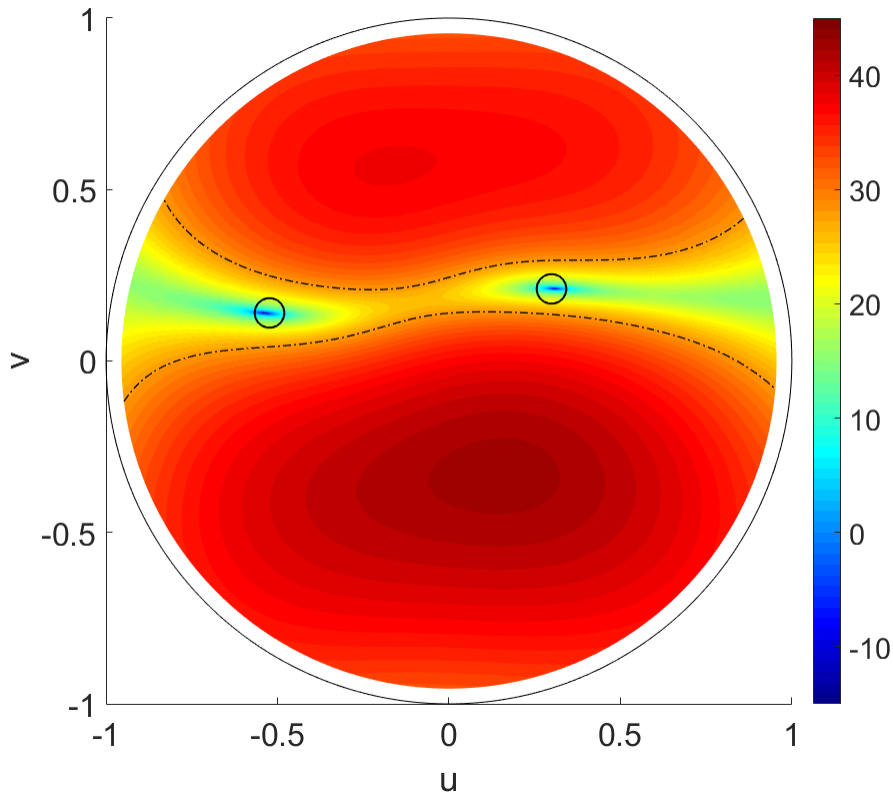

Figure 3.2: Coverage map (C_s/N_0) for analytically modeled CRPA with half wavelength ($d = \frac{\lambda}{2}$) spacing.

preserve relative areas. Each CRPA comprises four dual-linear elements in a 2×2 planar grid, with center coordinates of $(x_c, y_c, z_c) = \left(\pm\frac{d}{2}, \pm\frac{d}{2}, 0\right)$ where d is the CRPA spacing. The dashed line in Figs. 3.2 and 3.3 shows the boundary between the covered regions where C_s/N_0 exceeds the threshold, and outage regions where it does not. The jammer angles-of-arrival are marked by the black circles. The CRPA dimensions vary in Figs. 3.2 and 3.3 with spacings set to 9.5 cm and 19.0 cm which correspond to one half free-space wavelength, $\frac{\lambda}{2}$, at L1, and one wavelength, λ, respectively. Coverage is much higher for $d = \frac{\lambda}{2}$ at 85.5% than for $d = \lambda$ at 52.5%. This is because the larger d brings more of the CRPA response into the visible region, including areas with lower gain. Two lobes appear in Fig. 3.2 compared to the roughly six in Fig. 3.3.

This trend continues for other jamming environments with the same two CRPA models. Tracking coverage over multiple realizations and increasing jammer counts shows that the

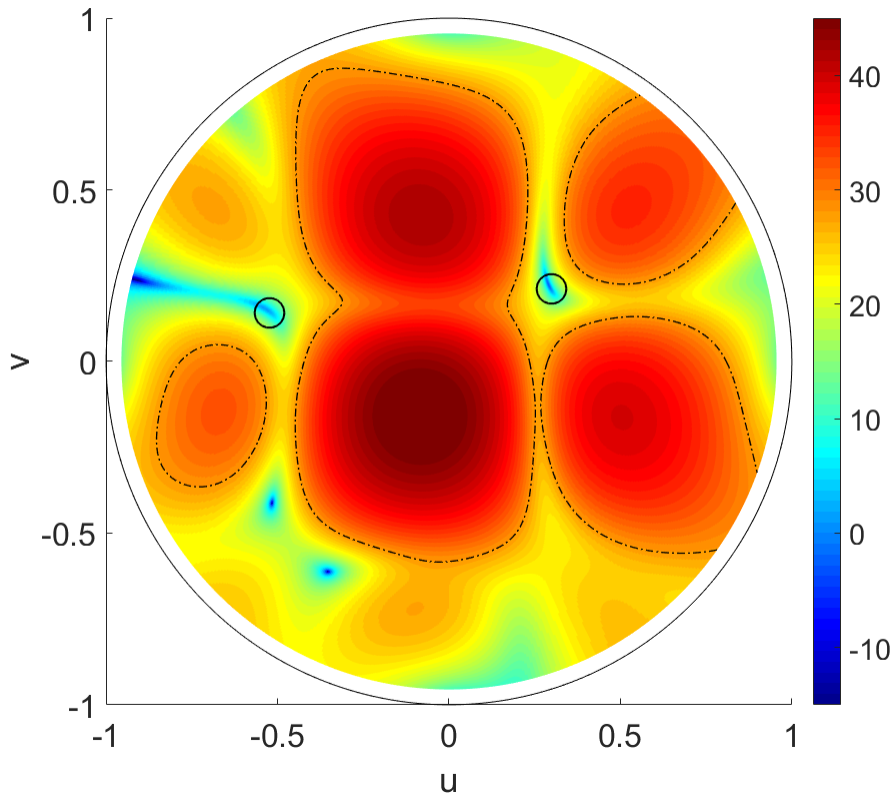

Figure 3.3: Coverage map (C_s/N_0) for analytically modeled CRPA with one wavelength ($d = \lambda$) spacing.

smaller CRPA has an advantage over the larger one. Figure 3.4 shows coverage across 1000 realizations of jamming environments with $J = 1, 2, \cdots, 10$ jammers present. The $d = \lambda$ CRPA shows worse performance in all cases, as expected. However, as stated before, this analytic model does not account for mutual coupling, which is more pronounced between CRPA elements with tighter spacing.

Performance between three different null-steering criteria is shown in Fig. 3.4. These criterion, taken from [16], are set by three different constraint vectors,

$$\mathbf{e}_1 = [1\ 0\ 0\ 0\ 0\ 0\ 0\ 0]^T\,,$$

$$\mathbf{e}_2 = [1\ 0\ 0\ 0\ 0\ 0\ 0]^T\,,$$

$$\mathbf{e}_3 = \tfrac{1}{\sqrt{2}}\,[1\ \ -j\ 0\ 0\ 0\ 0\ 0\ 0]^\dagger\,. \tag{3.8}$$

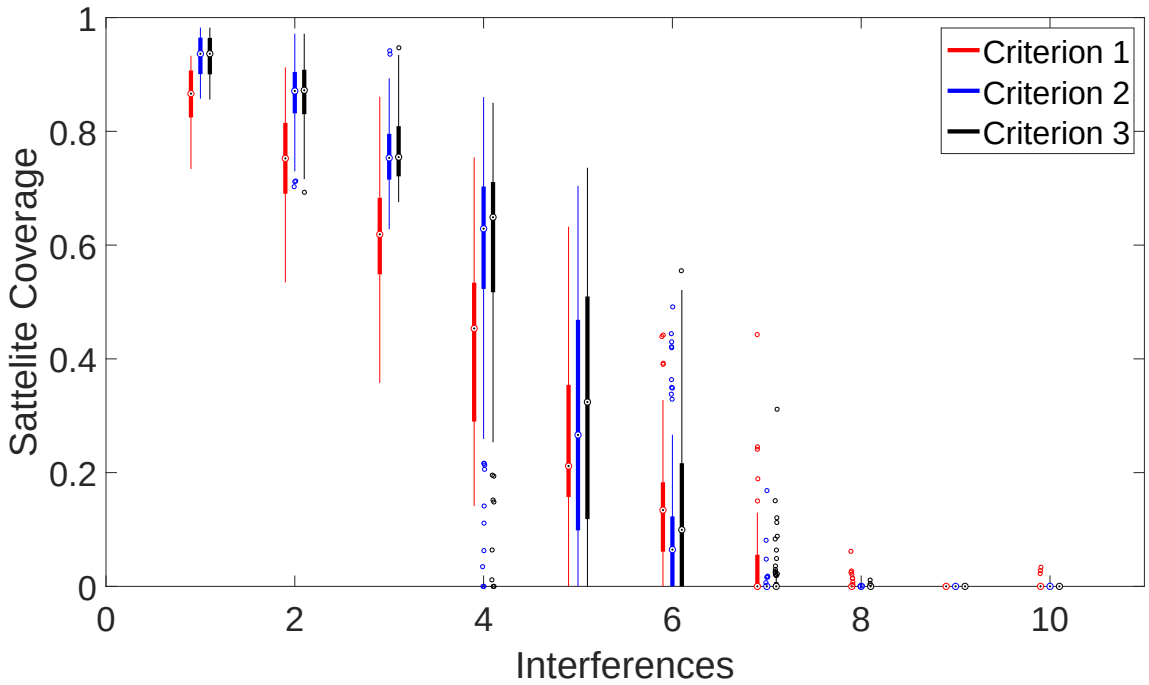

(a) CRPA spacing $d = \frac{\lambda}{2}$.

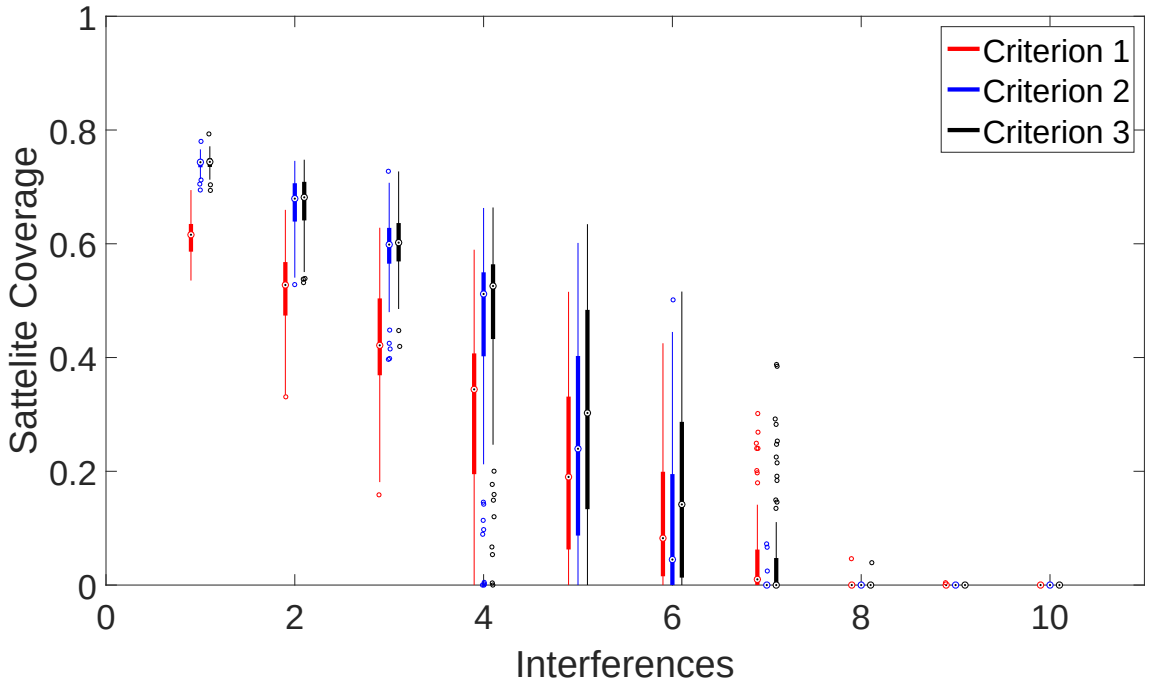

(b) CRPA spacing $d = \lambda$.

Figure 3.4: Coverage for multiple realizations of jamming environments with increasing jammer counts. Statistics for 1000 realizations each for one to ten jammers.

The first of these represents a single port on a dual-linear patch being used as a reference elements. The second criterion is a 7×1 vector, which assumes that the h and v ports on a single patch are combined with a 90° hybrid prior to null steering, effectively using a single RHCP reference element. The third criterion synthesizes an RHCP element with two ports on a reference element, though $\mathbf{e}_3$ has more degrees of freedom than $\mathbf{e}_2$. The differences between the three constraints can be discerned from either of Figs. 3.4a and 3.4b. The extra degree of freedom gives $\mathbf{e}3$ an advantage over $\mathbf{e}_2$ when the CRPA count increases, and both of these enjoy an advantage over $\mathbf{e}_1$, which has a 3 dB polarization mismatch with the GPS signal, resulting in lower C_s and therefore, lower coverage.

Jammer polarization also plays a role in CRPA performance when considering dual-linear elements. The RHCP GPS signals are of interest, and are best captured with RHCP elements, however LP interference will exhaust the degrees of freedom of a CRPA comprising only RHCP elements, as the CRPA's degrees of freedom are entirely in the spatial domain. An N port dual-linear CRPA has additional degrees of freedom in the polarization domain, and may cancel up to $N-1$ independent jammers. RHCP jammers exhaust the degrees of freedom more rapidly, and CRPA performance suffers more for the same number of RHCP jammers as it would for LP jammers.

In some instances, a dual-linear CRPA synthesizing an RHCP reference element can even maintain full coverage in the presence of one LP jammer, as appears in Fig. 3.5. The single jammer case for $\mathbf{e}_2$ and $\mathbf{e}_3$ have some cases with full coverage due to the fact that the dual-linear elements can cancel out an LP jammer and still receive half the power of an RHCP GPS signal from the same direction. This means that a visible null will not necessarily be present in the RHCP reception pattern of the CRPA when using dual-linear elements. The contrast between RHCP jammers in Fig. 3.4a and LP jammers in Fig. 3.5 is most pronounced for $J \geq 4$ jammers, when the degrees of freedom are being strained. High coverage is still predicted at $J = 7$ LP jammers for $\mathbf{e}_3$, with three quartiles of the cases resulting in greater than 60% coverage. Recall from Fig. 2.1 that this corresponds to a 97.5% chance of recovering four or more SVs and a position solution. The analytic CRPA model shows partial coverage for Fig. 3.4a when $4 \leq J \leq 7$, however this is overly optimistic and a result of the model assumptions. The limits of this model will be further

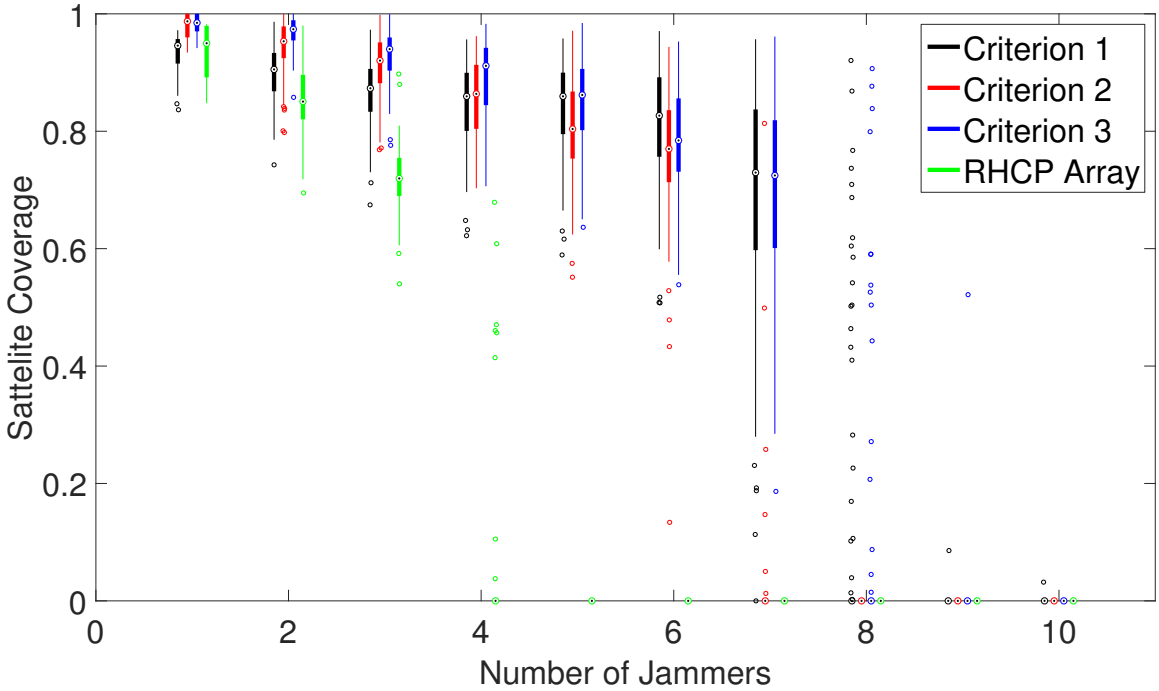

Figure 3.5: Satellite coverage of an $N = 8$ port dual-linear CRPA in the presence of LP jammers.

discussed in Section 3.3.2.

Analytic CRPA modeling is a useful first step, however, more sophisticated models are necessary for more accurate prediction. Numerical modeling can solve for complicated geometries which may not have closed form solutions and can be applied to either a single element or an entire CRPA model. This higher fidelity model requires greater computational resources, and the variety of CRPA models that can be compared is limited by the time required to solve for them. Alternatively, other methods can be employed, which can be used to rapidly model many CRPA geometries with slightly less accuracy. The following two sections explore both these methods and compare the capabilities of each.

3.2 Euler Rotations and Spatial Translations

The application of transformations, namely rotations and translations, to existing element patterns allows for changing the CRPA structure easily. Elements can be oriented and located almost arbitrarily, and models can be generated quickly from a single element pattern. These methods do neglect the effects of mutual coupling between elements, which

can be significant at small array spacings, but they offer the advantage of enabling rapid simulations of a wide variety of CRPA layouts that would be infeasible to model using higher fidelity numerical methods.

The Euler rotations and spatial translations are applied to existing elements patterns. These patterns are derived from either analytic models, as in [43], or by simulating a design in full-wave software for a single element [39]. Further discussion of full wave modeling appears in Section 3.3. After obtaining the isolated element pattern, the CRPA is constructed using a two step process: first, each element is oriented as desired using Euler rotations, then the elements are offset from the global coordinate origin by a spatial translation, i.e. phase shifting the rotated pattern to its new phase center.

The Euler rotation matrix is the product of three successive rotations; first around the z-axis by an angle $-\gamma$, followed by a rotation about the x-axis by α, and finally around the z-axis by γ,

$$\mathbf{R}_{Euler}\left(\alpha,\gamma\right)=\begin{bmatrix}\cos\gamma & -\sin\gamma & 0\\ \sin\gamma & \cos\gamma & 0\\ 0 & 0 & 1\end{bmatrix}\begin{bmatrix}1 & 0 & 0\\ 0 & \cos\alpha & \sin\alpha\\ 0 & -\sin\alpha & \cos\alpha\end{bmatrix}\begin{bmatrix}\cos\gamma & \sin\gamma & 0\\ -\sin\gamma & \cos\gamma & 0\\ 0 & 0 & 1\end{bmatrix}. \tag{3.9}$$

In this manner, most desired element orientations can be realized in three rotations. To apply $\mathbf{R}_{Euler}$ to the CRPA element patterns, first the global CRPA coordinates $\mathbf{r}_G = [x_G, y_G, z_G,]^T$ are defined as points on the unit sphere corresponding to the incident angles (θ_G, ϕ_G). These are used to find the local element coordinates $\mathbf{r}_L = [x_L, y_L, z_L,]^T$,

$$\mathbf{r}_L = \mathbf{R}_{Euler}\mathbf{r}_G. \tag{3.10}$$

Now the rotated vector effective height for the global incident angles is found from the vector effective height of the local coordinates,

$$\mathbf{h}_R\left(\theta_G,\phi_G\right)=\mathbf{h}\left(\theta_L,\phi_L\right). \tag{3.11}$$

Each CRPA element is rotated by the desired rotation angles, γ_i, α_i, before (2.41) is ap-

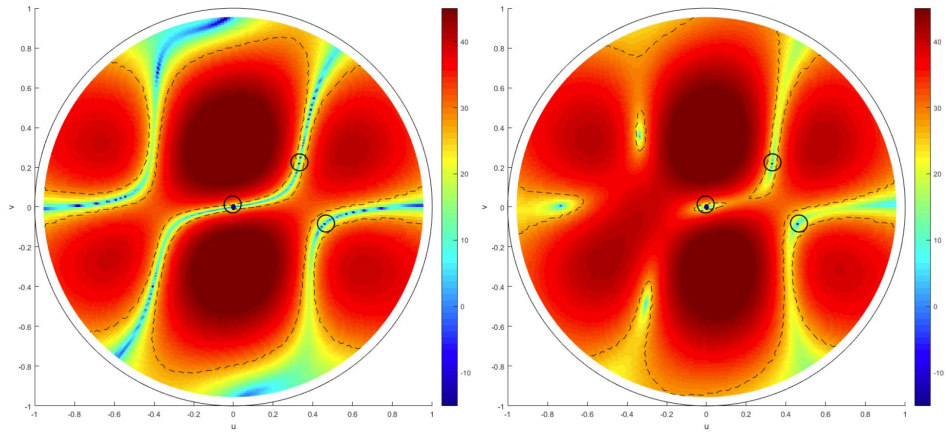

Figure 3.6: Coverage maps (C_s/N_0), for $d = \lambda$ spacing with regularly (left) and irregularly (right) spaced elements subject to three RHCP jammers.

plied. Finally, the element is offset from the global origin by applying a phase shift of $\psi = \mathbf{k}\left(\theta_G, \phi_G\right) \cdot \mathbf{r}_c$, where $\mathbf{r}_c$ gives the center coordinates of the antenna element.

The Euler rotation method is useful for generating CRPA models without the same computational costs as in full-wave modeling, however the S-parameter for an arbitrary CRPA is not known. This prevents the use of (2.47) and results in a model lacking the effects of mutual coupling between ports. With the exception of two ports on the same element, i.e. h and v ports on a dual-linear antenna, mutual coupling is not readily accounted for. This method suffers some reduction in accuracy but reduces the time necessary for generation and is appropriate for studying how small changes affect CRPA performance. Small changes to design parameters can be modeled using rotations and translation, as can dynamic changes in position for non-rigid CRPAs.

Now that the methodology for these transformations has been established, the next two sections will highlight applications to which this technique is well suited.

3.2.1 Euler Rotations for Modeling CRPA Geometry

A CRPA with large element spacing exhibits periodicity in the reception pattern. As the spacing increases, more of the CRPA response is brought into the visible region. When this pattern has nulls present in jammer angles-of-arrival, periodic nulls reduce satellite coverage and do not contribute to cancellation of interference. By spacing the CRPA elements

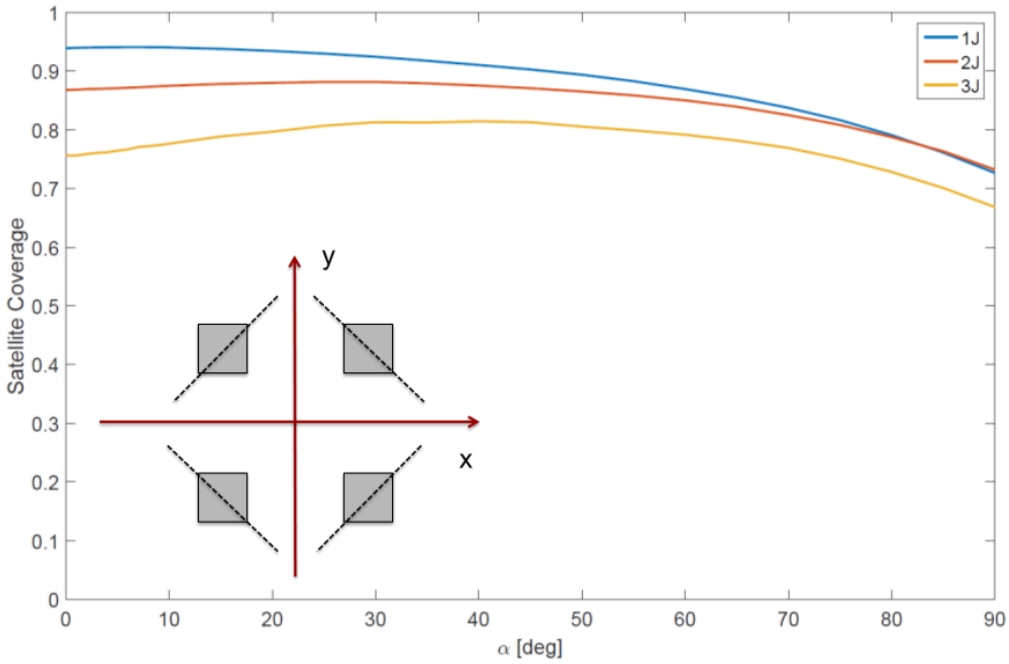

(a) Outboard CRPA footprint.

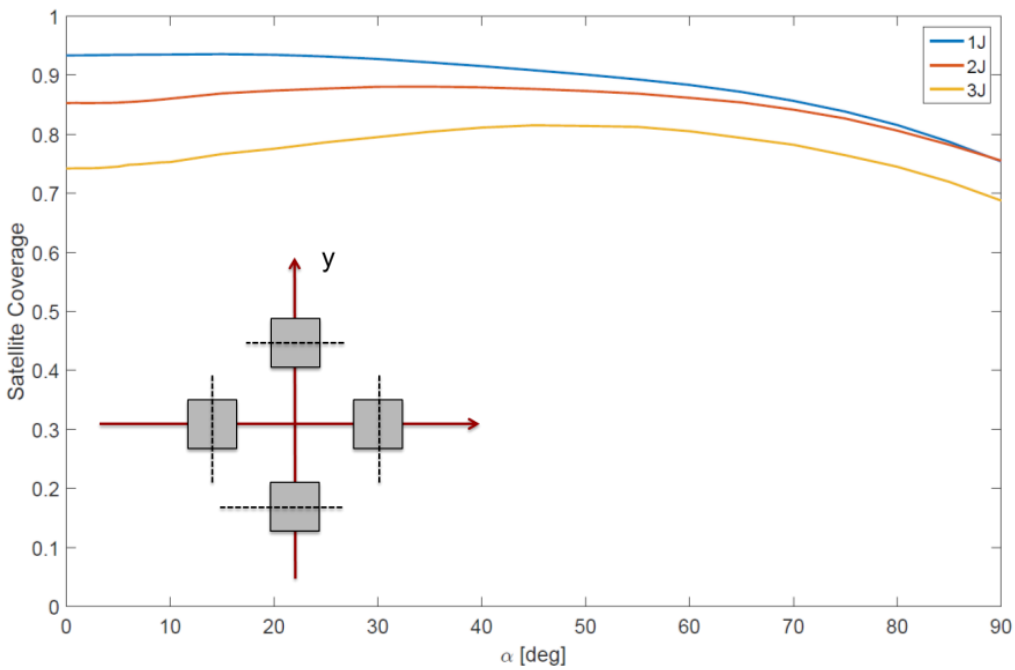

(b) Diamond CRPA footprint.

Figure 3.7: Mean coverage for two CRPA models sweeping through rotation angle α_i.

irregularly, or aperiodically, this effect can be mitigated. Coverage maps for two CRPAs, one with regular spacing and the other with the center coordinates randomly shifted in the

xy-plane, appear in Fig. 3.6. Note that the coverage increases for the irregularly spaced array as the low gain trenches are broken up.

Euler rotations allow for quickly generating multiple CRPA models with a single variable being changed, e.g., the rotation angles α_i. Two CRPA geometries, denoted "Outboard" and "Diamond" are shown in Fig. 3.7. The geometries differ in the axis of rotation of the patch elements, but keep the center-to-center spacing fixed at $d = \frac{\lambda}{2}$. Mean coverage as a function of α_i is plotted for each configuration for $J = 1, 2, 3$ jammers. In both Figs. 3.7a and 3.7b, all CRPA elements are rotated by the same α_i, and the constraint vector used is $\mathbf{e}_3$. A drop in coverage is observed as α_i approaches the horizon, due to the region of interest corresponding to the upper hemisphere, where the GPS SVs will be in view. However, for both CRPA configurations, an increase in coverage in the presence of multiple jammers is present for the regions $\alpha_i \in [30°, 60°]$. The weights for the reference element are fixed by $\mathbf{e}$, however weights on all other elements vary. Relative weight magnitudes increase for multiple jammers, corresponding to higher gain, and therefore C_s/N_0, in the region covered by those elements.

The analysis in Fig. 3.7 is enabled by the efficiency the Euler rotation method in modeling several CRPAs with small changes in geometry. With simple scripting methods, a variable such as α_i can be swept through a variety of values and coverage calculations can be performed much more rapidly than if full-wave modeling were to be used. This can be applied to any family of CRPAs that can be parameterized by a few variables to find optimal values.

3.2.2 Euler Rotations for Array Perturbations

The technique of rotating and translating element patterns is also well suited for studying the effects of relative motion between CRPA elements. The free-space wavelengths at the GPS L1 and L2 frequencies are 7.5 in and 9.6 in, respectively, and CRPA designs intended for dismounted soldiers must adhere to practical physical constraints. When considering a wearable on-body CRPA realization, the amount of space required for antenna elements renders a rigid construction infeasible. A CRPA comprising distributed elements that are free to move relative to one-another is far more realistic when considering the necessity of

dismounted soldiers to move. For such a construction, it is important to evaluate the CRPA performance. The rotational and translational techniques described above are well suited to simulating the small perturbations in element center location and orientation expected while the CRPA is subjected to jostling and other motion.

To investigate the effects of relative CRPA motion, a planar four-element CRPA is considered for comparison. This geometry is well studied, and performance under dynamic motion conditions can easily be compared to the static case. The first of these studies considers only motion in the plane. Each element is allowed to move by a random amount, $\Delta_{x,i}$ in the x direction and $\Delta_{y,i}$ in the y direction. All amounts are i.i.d. mean-zero random variables that are limited by some maximum amount, Δ_{max}. Both x and y maximum distances are taken to be the same. The notation is selected two represent the maximum relative distance any to elements may move relative to one another in a given direction in terms of the array spacing, d. Under this naming scheme, a maximum value of $\Delta_{max} = d/100$ in either x or y is denoted a 2% perturbation.

These spatial perturbations change the CRPA reception pattern when the weights are held fixed. A CRPA in a stable state, i.e. one that has had sufficient time to converge to stable weights in a stationary jamming environment, will have a null directed in the angle-of-arrival of the jammer or jammers present. When the center locations of the CRPA elements changes rapidly enough that the weights do not have time to update, the reception pattern changes slightly, and the null is no longer aligned with the jammer. Some jammer cancellation is still accomplished provided that the reception pattern does not substantially change due to the jammer still being aligned with a low gain region of the pattern. If the perturbations are small relative to array spacing, this can be expected.

This is demonstrated in Fig. 3.8, where the stable weights from an unperturbed, or periodic, CRPA are applied to ten different realizations of randomly perturbed CRPAs. Overall coverage as a function of jammer power is plotted, with the dashed line representing the unperturbed CRPA, and the solid lines representing the perturbations. Initially, coverage is high due to jammer power being below the noise floor. As jammer power increases, the best case periodic CRPA coverage dips below its final value, occurring around -130 dBW. When the jammer power level is close to the noise power, full cancellation is difficult as the

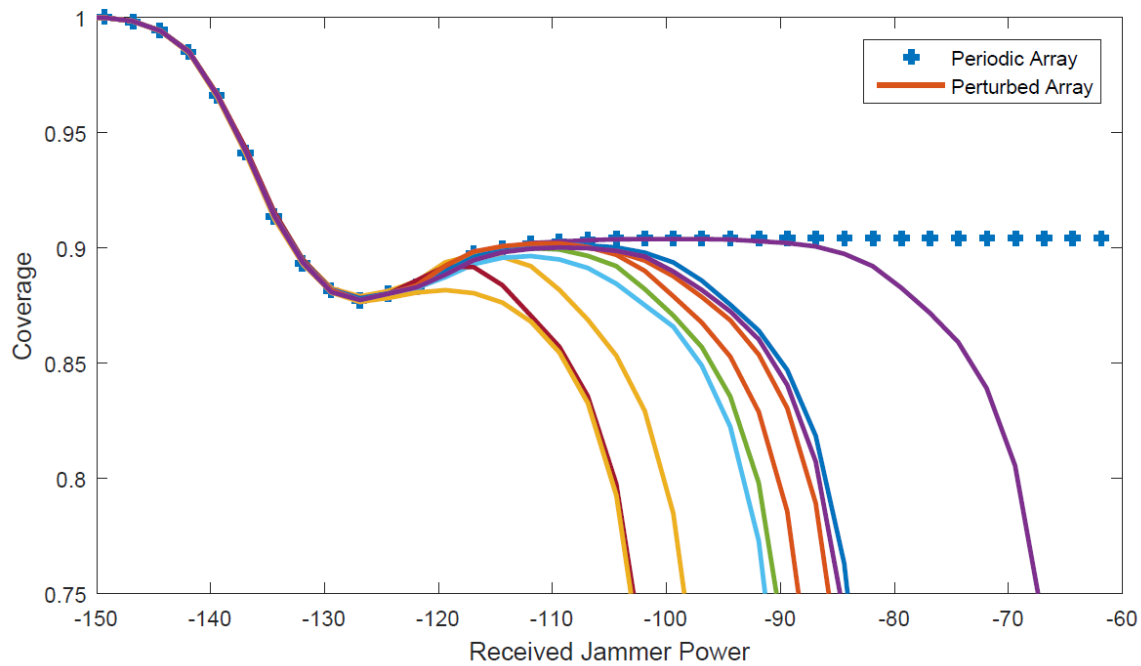

Figure 3.8: Coverage vs received jammer power for a ten CRPAs with random 1% spatial perturbations.

weights must balance between jammer cancellation and increasing noise power. When the jammer power level is large compared to the noise, a deep null forms. This occurs when the jammer is approximately 10 dB above the noise power in Fig. 3.8. For the periodic array, coverage converges to its final value. It should be noted that this model does not address physical limitations of implementing a CRPA in hardware. Jammer cancellation as power increases will be limited by the dynamic range of the receiver.

The representative perturbed arrays all show the same dip followed by an increase in coverage. For the worst case realization, this increase is minuscule and coverage quickly drops as jammer power increases. The realization with the highest performance shows high coverage until the received jammer power reaches -80 dBW. The decrease in coverage corresponds to a fixed level of jammer suppression. CRPA pattern nulls are narrow relative to the CRPA beamwidth, therefore any misalignment between the null and the jammer results in a substantial difference in jammer suppression, which in turn leads to lower C_s/N_0 and coverage. The effect of perturbations on jammer suppression is demonstrated more clearly in Fig. 3.9. The jammer power level prior to nulling for a single jammer is recorded

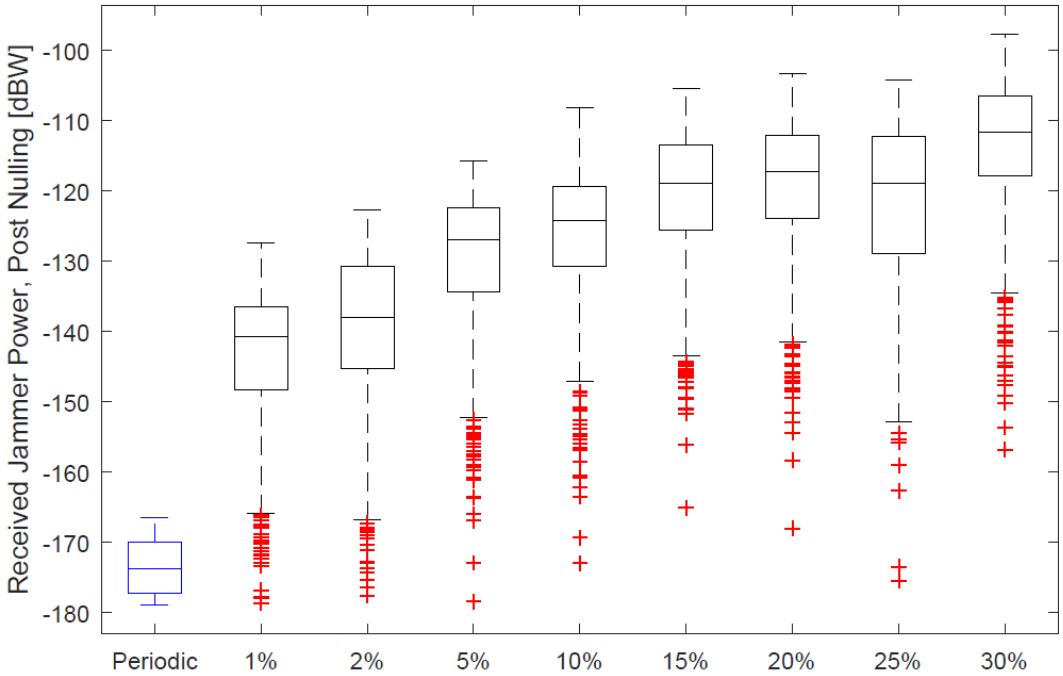

(a) Jammer suppression for nominal spacing of $\frac{\lambda}{2}$.

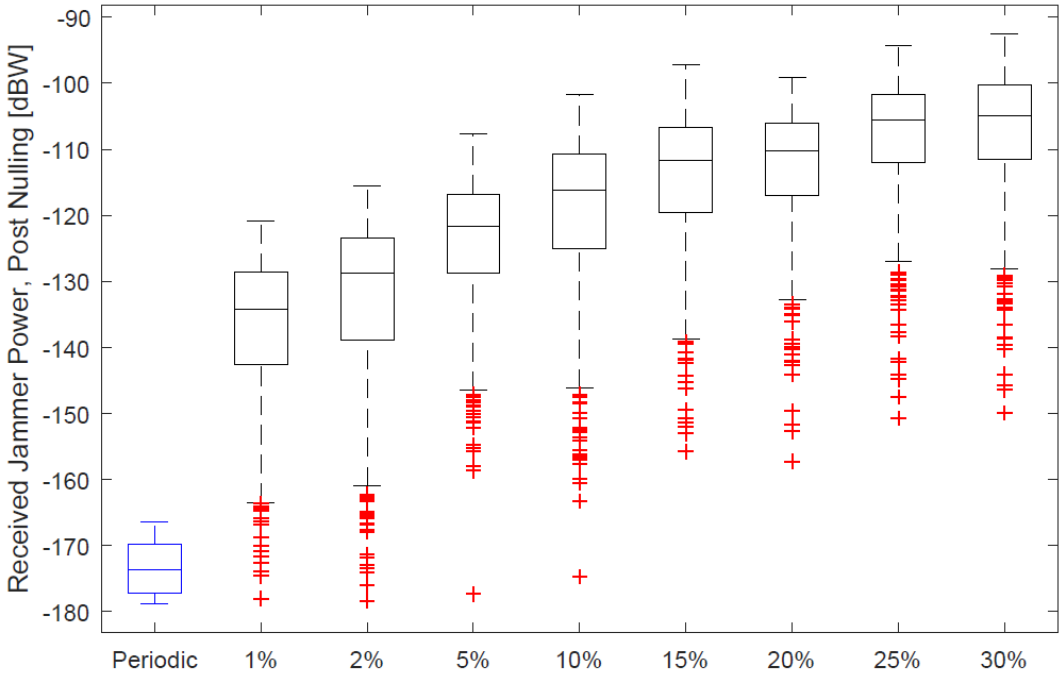

(b) Jammer suppression for nominal spacing of λ.

Figure 3.9: Jammer suppression under CRPA perturbations.

for multiple jamming environments. In each instance, the stable weights are recorded for the unperturbed or periodic array and applied to multiple realizations of perturbed arrays. The perturbation amounts range from 1% to 30%, as previously defined. A nominal pre-nulling jammer power level of -95 dBW is used. Both the half-wavelength spaced array in Fig. 3.9a and the one-wavelength spaced array in Fig. 3.9b show an immediate decrease in jammer suppression. At the 1% perturbation level, suppression drops by 35 dB and 40 dB in each of these, respectively, and at the 5% perturbation level the median output power level has surpassed the noise power of -129 dBW for either array spacing.

Similar results are obtained for CRPA elements tilting out of the array plane. Defining the tilt percentage as the maximum tilt angle over 90°, random realizations of tilted CRPAs can be applied to jamming environments. In each case, each element rotates in a right-handed sense about an axis defined by an angle $\gamma_i \sim \mathrm{U}[0, 2\pi]$. Similarly to the spatial perturbations, tilted perturbations move the null location away from the jammer direction, resulting in worse jammer suppression. This results in lower coverage, as seen in Fig. 3.10. Even just a 1% perturbation in tilt angle, i.e. each element rotating by a maximum of 0.9° out of the plane, results in an immediate, albeit modest, decrease in coverage. Median coverage for both array spacings drops well below the 50% mark for a tilted perturbation of 5%, i.e. a maximum angle of 4.5°.

Both spatial perturbations and rotations can be expected for an in-situ distributed CRPA, and as seen from Figs. 3.9 and 3.10, either of these will have a significant impact on CRPA performance if the weights are held stable. The question remains as to whether an adaptive implementation would have the time to react to dynamic non-uniform movement of CRPA elements.

To address this, two possible velocities were considered to generate an estimate of how well a CRPA could respond. The first velocity estimate comes from an assumed worst case scenario. At the time of writing, the world record speed for a heavyweight boxer's punch is held by Ricky Hatton [82]. Hatton was able to throw a punch at 14.3 $\frac{m}{s}$, which is used as an upper limit to the velocity any two elements of an on-body distributed CRPA. In fact, under normal operating conditions, it is not suspected that this velocity will ever be reached. A more representative velocity estimate can be made by considering the requirements for a

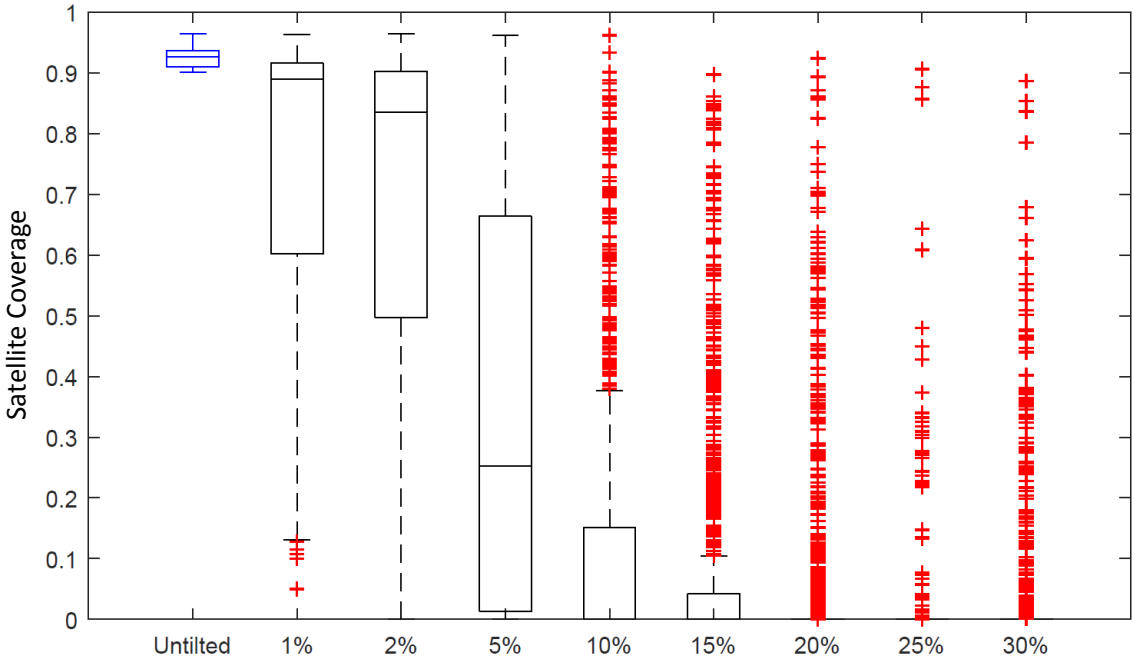

(a) Coverage for spacing of $\frac{\lambda}{2}$.

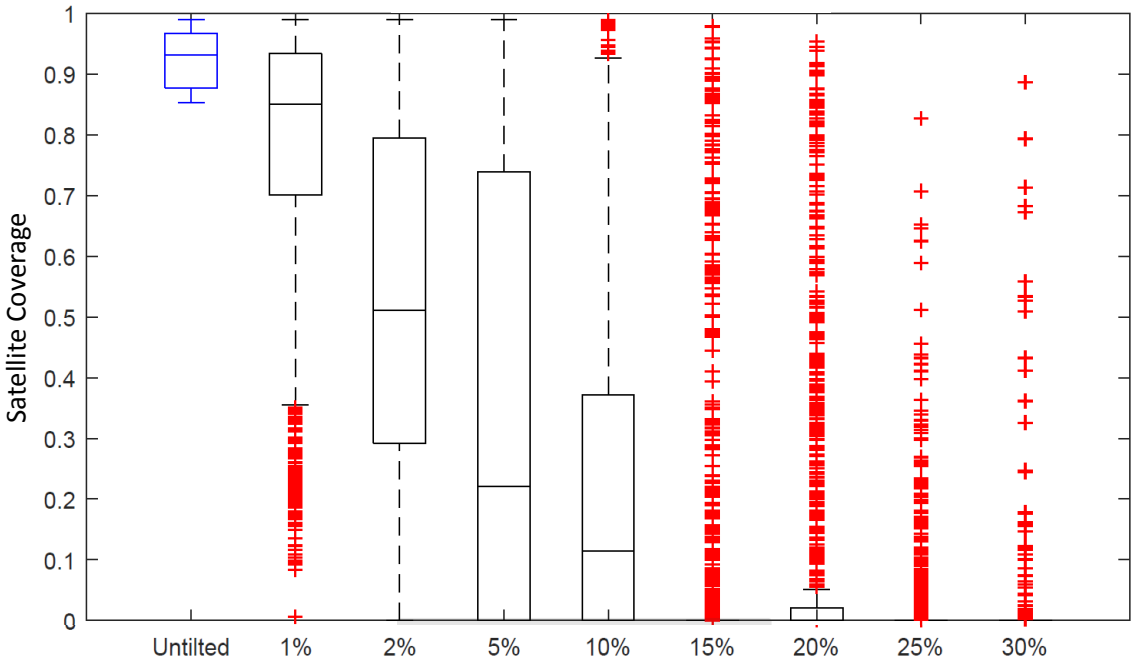

(b) Coverage for spacing of λ.

Figure 3.10: Satellite coverage under CRPA tilted perturbations.

military fitness test used by the United States Marines. The Marine Corps Physical Fitness Test circa 2010 tested Marines in three areas, including abdominal crunches. In this test, a Marine could obtain a perfect score by completing 100 abdominal crunches in a two minute

window. This corresponds to a velocity of slightly less than 1 $\frac{m}{s}$ for the torso relative to the legs, which remain mostly stationary. This value, one meter per second, is more realistic than the world record winning velocity of 14 $\frac{m}{s}$ and still exceeds the velocities anticipated for individual elements in situations where the dismounted soldier would be paying attention to his GPS receiver.

Table 3.1: Estimated times to reach perturbation percentages [μs].

Amount Perturbed	1%	2%	5%	10%
λ spacing at 14 $\frac{m}{s}$	66.7	133	333	666
$\frac{\lambda}{2}$ spacing at 14 $\frac{m}{s}$	33.3	66.7	166	333
λ spacing at 1.0 $\frac{m}{s}$	952	1904	4760	9520
$\frac{\lambda}{2}$ spacing at 1.0 $\frac{m}{s}$	476	952	2380	4760

The approximate travel times for both velocity estimates appear in Table 3.1 . For either array spacing, this value denotes how much time is necessary for an element to travel the maximum distance corresponding to the array perturbation percentage, e.g., at 14.3 $\frac{m}{s}$ an element would take 666.7 μs to travel 10% of the array spacing, or 9.5 cm. The impact of these movements, with respect to coverage, is dependent on the time needed for weights to update, therefore a first order approximation of convergence time is needed. This is accomplished by estimating the number of samples needed for weights to become stable and making assumptions about the hardware implementation of the CRPA.

To estimate the necessary number of samples, time domain data for jamming environments were generated assuming complex sinusoidal representations of the jammer with magnitudes and phases determined by the CRPA elements' reception pattern in the assumed jammer directions,

$$[\mathbf{x}]_i = g_i(\theta,\phi)\left\{\cos\left[\omega t + \psi_i(\theta,\phi)\right] + j\sin\left[\omega t + \psi_i(\theta,\phi)\right]\right\} + \frac{\sigma}{\sqrt{2}}\left[\eta(t) + j\nu(t)\right]. \tag{3.12}$$

Here, g_i and ψ_i denote the magnitude and phase of the ith elements reception pattern toward the jammer, respectively, and η and ν are mean-zero i.i.d. Gaussian random processes with variance one. The covariance matrix estimate at time t, $\hat{\mathbf{R}}(t)$, is found from a Monte Carlo average, and the weights at time t are calculated using the sample matrix inversion (SMI) equation, (2.15), with all available samples for $t = 0$ to the present time. Coverage

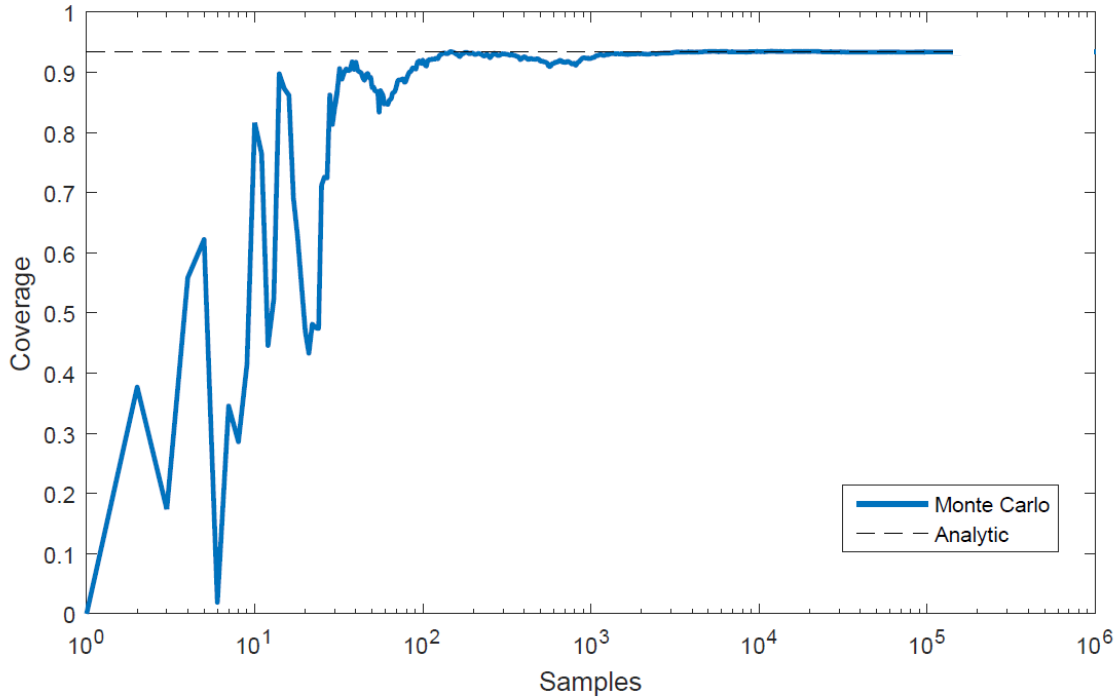

Figure 3.11: Coverage calculated using sample matrix inversion for a Monte Carlo covariance matrix estimate. One jammer impinging on a 2×2 dual-linear CRPA.

calculations as a function of time are shown in Fig. 3.11 and compared against the analytic solution found assuming perfect knowledge of $\mathbf{R}$. For this realization, SMI coverage reaches 1% of the analytic coverage value within 1050 samples. Repeating this experiment with three jammers increased this number to 1550 samples, as is seen from Fig 3.12.

To convert the number of samples to an estimate of convergence time, assumptions about the hardware must be made. Searching for commercially available FPGAs at the time of writing led to a reasonable clock rate estimate of 75 MHz and an update latency of 3 clock cycles. For K samples at this rate, the convergence time is found from

$$t_{convergence} = K \text{ samples} \frac{1}{75} \times \frac{\text{seconds}}{\text{cycle}} \times 3 \frac{\text{cycles}}{\text{sample}} , \tag{3.13}$$

which yields 42 μs and 62 μs for the one jammer and three jammer cases, respectively. Comparing these values to the perturbation travel times in Table 3.1, only one entry (33.3 μs) falls below the estimated convergence times. This corresponds to a modest decrease in cov-

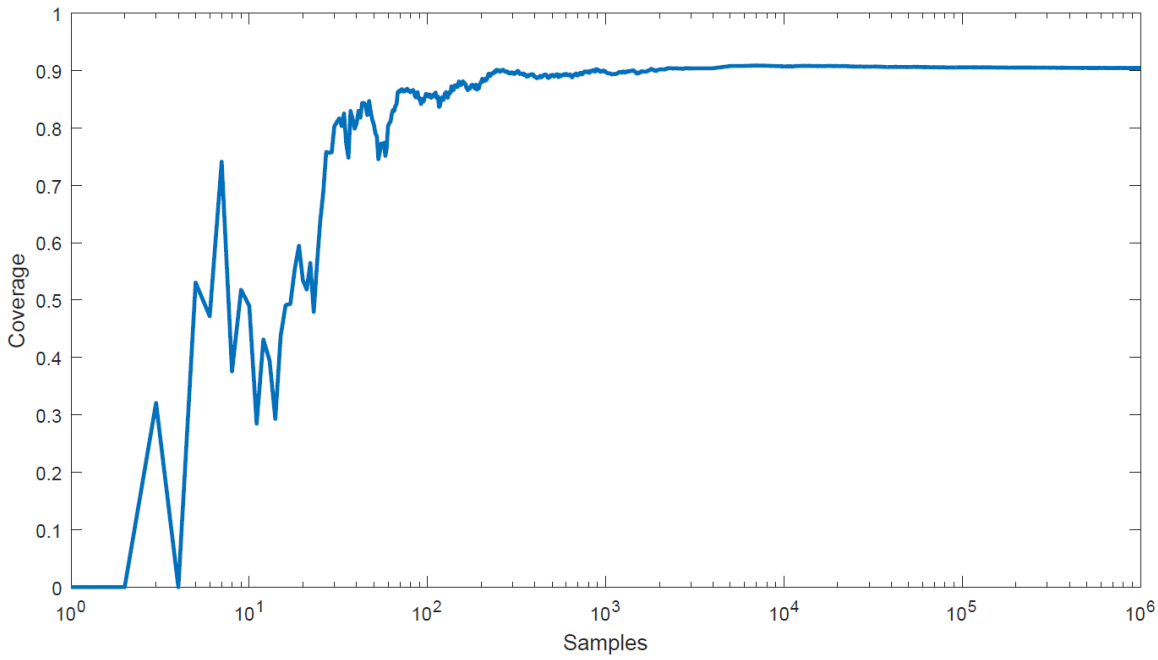

Figure 3.12: Coverage calculated using sample matrix inversion for a Monte Carlo covariance matrix estimate. Three jammers impinging on a 2×2 dual-linear CRPA.

erage assuming the highest conceivable element velocities. At the more realistic 1 $\frac{\mathrm{m}}{\mathrm{s}}$ speed, all travel times are greater than convergence times. Using reasonable hardware assumptions and velocity estimates, the problem of relative motions of elements does not appear to have overly detrimental effects on coverage. Of course, design of the DSP portion of a CRPA will have to account for the operating conditions and actual hardware used. FPGA clock rates can be set appropriately given specific algorithm and hardware capabilities.

In Section 3.2, a method for modeling CRPAs of arbitrary geometries has been presented. The strength of this method is in its adaptability and reduced computational demands compared to other methods. Comparisons between parametric CRPA designs and a random perturbation study have been presented to showcase the uses of this method. In Section 3.3, more accurate full-wave modeling is described, and the two methods are compared in terms of performance prediction under the satellite coverage metric.

3.3 Full-Wave Electromagnetic Modeling

Analytic modeling methods for antenna elements depend on simplifying assumptions, and are more idealized than physically realizable antennas. Alternatively, isolated element patterns can be obtained through the use of full-wave electromagnetic modeling software to incorporate material effects. These patterns can be transformed using the Euler rotations and spatial translations presented above, however, this is still an incomplete method in the sense that proximity effects between elements and other objects in the environment are not accounted for. This is true whether the transformations are applied to analytically modeled element patterns or patterns obtained through full-wave modeling. Incorporation of mutual coupling between elements and dielectric losses from objects in the environment can be achieved through full-wave modeling of a complete CRPA, or array environment model. However, this comes at the cost of increased computational complexity in the form of higher demands on memory and increased processor time.

The commercially available electromagnetic modeling software, *FEKO*, is one of many software suites on the market that can simulate array environment models and deliver element patterns, mutual impedances, and the effects of near-field scattering objects such as the human body. FEKO utilizes the Moment of Methods (MOM) to solve for current distributions over complex structures. This is accomplished by solving an $N \times N$ matrix equation which solves the boundary conditions in an average sense over the surface [71]. Here, N is the number of polygons used to approximate the surface of the antenna structure. The result is a computationally intensive, accurate solution to the radiated fields by the antenna.

The radiated patterns for the CRPA ports are computed by exciting each port individually in a separate simulation. The result of each simulation is the radiated fields $\mathbf{E}^{rad}$ for use in Eqs. (2.40) and (2.41). All patterns are phase referenced to the origin, not their own phase center, therefore (2.42) is not necessary.

This gives the open circuit voltage for each port under the assumption that all other ports are left open. To obtain the patterns with the ports terminated, the coupling matrix $\mathbf{A}$, for a given loading condition must be calculated. This is accomplished by first computing

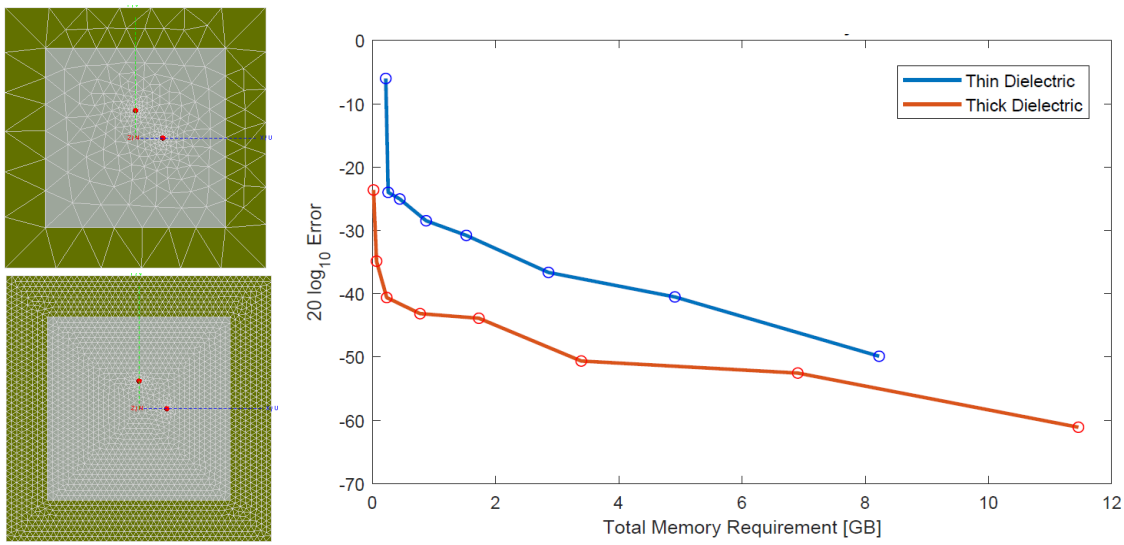

Figure 3.13: Error vs increasing memory requirements for two patch widths $W = 1.27$ mm and $W = 12.70$ mm. Memory requirements increase for finer mesh sizes.

S in FEKO, and choosing a load impedance for use in (2.47). Matched loads, where $z_L = z_{in}^*$ eliminate reflection between antenna ports and their terminations, and deliver the maximum power for the load, and so a load equal to the complex conjugate of the average antenna impedance is chosen. It is also possible to replace $z_L \mathbf{I}_{N\times N}$ with a diagonal matrix with each element $z_{L,i} = z_{in,i}$, however the CRPAs modeled here had little variation in input impedance making this unnecessary.

The array environment simulation in FEKO meshes the surface of the CRPA geometry into multiple triangles, and computes a MOM matrix that grows quadratically with the number of triangles. Finer mesh sizes increase the accuracy to a point, however the solution eventually converges. Median error, ε, as a function of mesh size is plotted in Fig. 3.13 for two isolated element patch antennas. Here, error is defined as the norm of the difference in the electric fields of the two simulations over the maximum norm of the electric field for the finer simulation,

$$\varepsilon = \frac{\|\mathbf{E}_a - \mathbf{E}_{90}\|_2}{\max\limits_{\theta,\phi} \|\mathbf{E}_{90}\|_2}, \tag{3.14}$$

where the subscript a corresponds to the numerator of the mesh length $\frac{\lambda}{a}$, i.e. the maximum length of the side of a mesh triangle, which ranges from $\frac{\lambda}{10}$ to $\frac{\lambda}{90}$. Note that the thinner

patch has higher error for the same mesh size. This necessitates very fine mesh sizes for simulation of textile antenna elements and increases the computational demand for the CRPA model. The element modeled for this comparison is relatively small compared to a 2×2 planar CRPA with no additional objects in the environment, and already 1 GB of memory is required to reduce the median error below 30 dB. This limits the size of the full-wave model depending on the machine running the simulation.

3.3.1 Full-Wave Weighting and Verification

In order to thoroughly confirm the methods described above and build confidence in the model, a method for applying null-steering weights calculated in MATLAB to the full-wave CRPA model is laid out here. Electromagnetic waves radiate due to the acceleration of electrons, i.e. time varying currents. As such, a radiating FEKO model which incorporates the complex valued weights must be excited by current sources, however, the full-wave model of the planar dual-linear CRPA considered in Section 3.1 is generated using FEKO's MOM solver. This is appropriate for planar structures, although FEKO does not support current excitations for MOM structures. To use a current source, a finite element method (FEM) model must be constructed. Though FEM has advantages for arbitrary volumes, the planar structure of this CRPA is best modeled with MOM, and the results from the two models may vary. Using a model solved by FEM to verify an existing model using MOM does not make sense and invites differences and errors to creep in. Rather, the existing model must be modified in such a way as to verify the CRPA perfomance.

Exciting the array with complex valued voltage sources will not ensure the desired weights are applied to each CRPA element, as mutual coupling between ports will change the current distribution on each element. In order to apply the weights without distortion, the original radiating model is modified to a receiving configuration. The CRPA is excited with plane waves from multiple directions, and the received signals on each port are combined using a non-radiating network. This network is defined in terms of its S-parameter, with the desired effect that the received signals on each of the eight CRPA ports are combined on a ninth port, which is terminated by a 50 Ω load. The S-parameter defines the relationship

between incident and reflected voltage waves on a multiport network,

$$\mathbf{v}^- = \mathbf{S}\mathbf{v}^+, \tag{3.15}$$

where $\mathbf{v}^-$ is the reflected component and $\mathbf{v}^+$ is the incident wave. The desired network must not induce any reflections on the eight CRPA ports, i.e. $[\mathbf{S}]_{i,j} = 0$ for $i, j = 1, 2, ..., 8$. Also, the network must perform the linear combination of the eight antenna ports and supply the result to the ninth port, i.e. $[\mathbf{v}^-]_9 = \sum_{i=1}^{8} [\mathbf{w}]_j^* [\mathbf{v}^+]_j$. Therefore, $\mathbf{S}$ is defined as

$$\mathbf{S} \begin{bmatrix} 0 & 0 & \cdots & 0 & w_1^* \\ 0 & 0 & \cdots & 0 & w_2^* \\ \vdots & \vdots & \ddots & \vdots & \vdots \\ 0 & 0 & \cdots & 0 & w_8^* \\ w_1^* & w_2^* & \cdots & w_8^* & 0 \end{bmatrix}. \tag{3.16}$$

Note that $\mathbf{S}$ is reciprocal, though this is not strictly necessary. A non-radiating network in FEKO with this form will behave as intended if no reflections are present, however, the matrix elements $[\mathbf{S}]_{i,j}$ are defined under the assumption that all ports are matched. If the antenna ports vary from 50 Ω by any amount, errors are introduced. To eliminate these errors, $\mathbf{S}$ must be renormalized in terms of the actual port impedances of the modeled CRPA [73]. These impedances are the diagonal elements of the Z-parameter, and are found from the CRPA S-parameter solved with the FEKO model and (2.45). Let Z_n denote the port impedance for the nth CRPA element, $\hat{Z}_n$ be the port impedance for the nth network port, and the diagonal matrices $\mathbf{B}$ and $\mathbf{C}$ be defined as

$$\mathbf{B}_n = \frac{1}{\hat{Z}_n + Z_n} \sqrt{\frac{\hat{Z}_n}{Z_n}}, \tag{3.17}$$

$$\mathbf{C}_n = \frac{\hat{Z}_n - Z_n}{\hat{Z}_n + Z_n}. \tag{3.18}$$

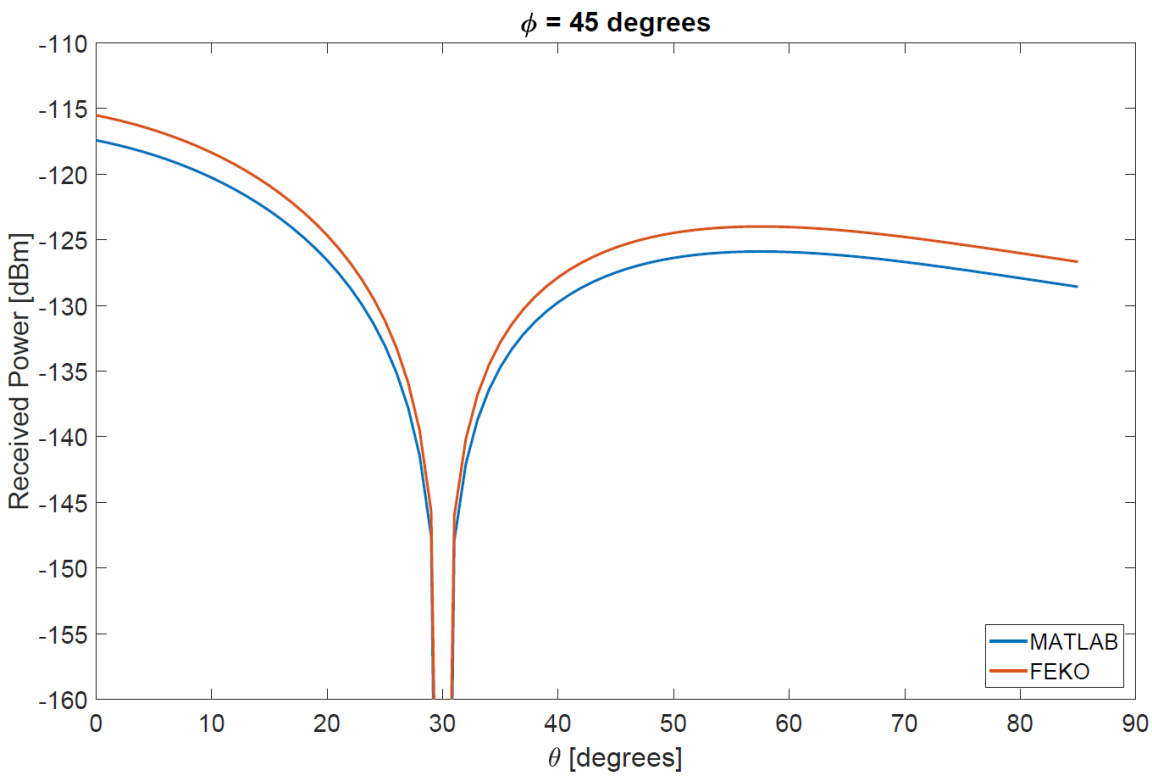

Figure 3.14: Comparison of received GPS power, C_s, between MATLAB null-steering suite prediction and FEKO non-radiating power combiner network.

Now the renormalized S-parameter, $\hat{\mathbf{S}}$, is given by,

$$\hat{\mathbf{S}} = \mathbf{B}^{-1} (\mathbf{S} - \mathbf{C}) (\mathbf{I} - \mathbf{CS})^{-1} \mathbf{B}. \tag{3.19}$$

Using the eight-port dual-linear planar CRPA, weights are derived for a jamming environment with a single RHCP jammer located at $(\theta_j, \phi_j) = (30°, 45°)$ and used to form $\hat{\mathbf{S}}$ for a non-radiating network in FEKO. The CRPA model is connected to the network and excited by RHCP plane waves arriving in 1° increments along θ, and the received pattern of the CRPA through $\hat{\mathbf{S}}$ is recorded. Figure 3.14 shows this reception pattern along with the predicted pattern from the MATLAB null-steering suite. The two patterns are nearly identical, save an assumed receiver loss of 2 dB which was incorporated into the MATLAB model, but neglected in FEKO. This confirms the integration of full-wave patterns into the CRPA model as described above.

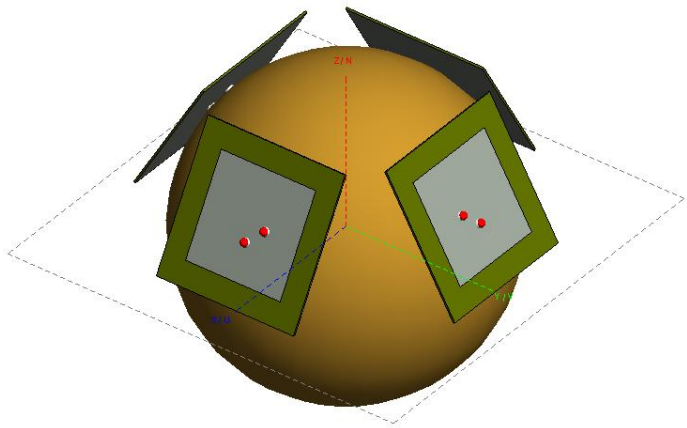

Figure 3.15: In-situ head mounted CRPA with simplified human head phantom.

3.3.2 Modeling Method Comparison

To demonstrate the limitations of analytic pattern modeling and pattern transformations described above, a comparison with the full-wave array environment CRPA model was carried out [39]. A CRPA with the same diamond footprint as in Fig. 3.7b was modeled using both the Euler rotations and the full-wave array environment methods. The full-wave model also included a dielectric sphere with properties matching human brain matter, intended as a crude model of the head for a helmet mounted CRPA[1]. Both CRPA models were subjected to the same jamming environments (1000 realizations each with $J = 1, 2 \cdots, 8$ randomly placed RHCP jammers) and coverage was logged for each. The Free-Space CRPA referred to in Fig. 3.16 is modeled using the Euler transformation method of Section 3.2, whereas the In-Situ CRPA refers to the full-wave CRPA model. Each CRPA comprises four dual-linear elements for $N = 8$ ports. For $1 \leq J \leq 3$ jammers, the full-wave CRPA actually performs better. This is due to the dielectric sphere acting somewhat like a ground plane and making the CRPA element patterns more directive. The degrees of freedom for each CRPA are expected to be exhausted by $J = 4$ RHCP jammers, as can be seen by the sharp drop in coverage, however the free-space CRPA model continues to predict median cover-

[1]It should be noted that a helmet mounted design is impractical for safety concerns.

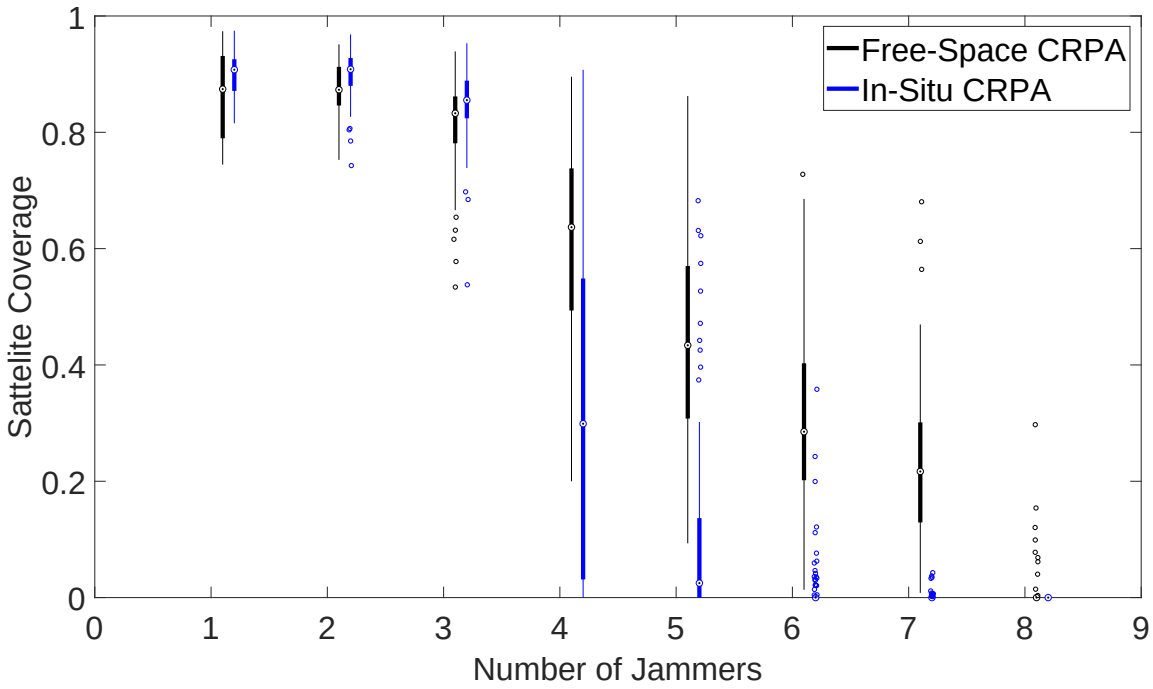

Figure 3.16: Satellite coverage across multiple realizations with mutual coupling and dielectric losses (in-situ) and without (free-space).

age values about 30% higher than the more realistic CRPA model. This overly optimistic prediction ignores the realities of a physically realizable CRPA. Mutual coupling between ports diminishes performance here as there is an additional correlated component between the CRPA elements. Additionally, the dielectric sphere acts as an obstruction and reduces the gain in the overlapping region.

Full-wave modeling offers more realistic pattern modeling and incorporates proximity effects neglected by other methods described in this chapter. Additionally, the methodology has been verified in and high confidence can be placed in results obtained through these methods. Simpler CRPA models (in terms of computational efficiency) are a good alternative when multpile geometries must be modeled and compared, but, as seen from Fig. 3.16, predictions made with these simplifying assumptions can be overly optimistic. When considering a large design space, Euler rotations and spatial translations are best used as a starting point, with a final design being verified with more realistic modeling methods.

3.4 Anechoic Chamber Measurements

Antenna measurements in the anechoic chamber approach the idealized free-space models by minimizing exterior interference and interior reflections. This environment is well suited to achieving null-synthesis in hardware, a necessary step for confirming the theory. To achieve a successful CRPA implementation, methods for acquiring data and measuring patterns must be developed.

To acquire the data for null-synthesis, two methods may be employed. The first is to simply measure the CRPA element patterns, and generate a received vector $\mathbf{x}_j$ from sampling multiple antenna patterns at a given direction. First the CRPA must be mounted in the anechoic chamber on the mast, and then each element must be measured one at a time, with all others terminated in 50 Ω loads. An RHCP transmit antenna at the apex is ideal, if RHCP reception patterns and jammers are desired, however, a single LP antenna may be used in lieu of an RHCP antenna. For synthesizing the RHCP reception pattern of a CRPA element with a standard gain horn, two measurements are necessary. The horn must be rotated 90°, resulting in two measurements F_h and F_v, which are then added together in post processing to generate

$$F_r = \frac{F_h}{\sqrt{2}} - j\frac{F_v}{\sqrt{2}}. \tag{3.20}$$

Figure 3.17 shows the magnitude and phase of such a measurement for the V port of a dual linear element. The same element was also measured using a RHCP transmit antenna at 30° increments, and the two measurements show good agreement.

From here, the received vector $\mathbf{x}_j$ is taken to be a combination of $F_{r,n}(\theta, \phi)$ for each of the N CRPA elements at the desired angle-of-arrival. The covariance matrix is formed by assuming some noise power, although the F measurements should be reasonably free of noise, and calculating $\mathbf{w}$ from the matrix inversion equation (2.5),

$$\mathbf{w} = \frac{\mathbf{R}^{-1}\mathbf{e}}{\mathbf{e}^{\dagger}\mathbf{R}^{-1}\mathbf{e}}.$$

Without the assumed noise, $\mathbf{R}$ is a singular matrix, however, if the noise power is too large compared to the implicit jammer power the optimal weights will not produce a deep

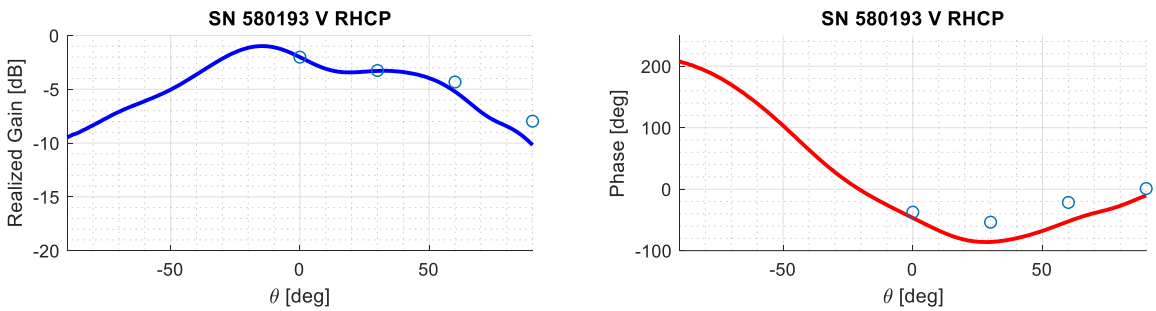

Figure 3.17: Antenna element RHCP reception pattern measurement synthesized from two LP antenna measurements. The points correspond to measurements of the same antenna element using a RHCP transmit antenna.

null [42]. A jammer to noise ratio of around 20 dB will accomplish the desired results.

The second method that may be employed is to acquire time-domain samples using a data acquisition tool. One such tool which requires minimal setup is a digital storage oscilloscope, such as the Keysight DSO 91240. The DSO can sample four channels simultaneously and transfer the data over Ethernet to a PC for post processing. This allows for use in the iterative algorithm, (2.28),

$$\mathbf{w}_{k+1} = \mathbf{e} + \mathbf{P}\left[\mathbf{w}_k - \mu \mathbf{x}_k y_k^*\right].$$

An added benefit is that connections to CRPA ports need not be changed between measurements, however, this does not allow for the synthesis of an RHCP jammer if the transmit antenna is LP.

Hardware that applies the weights to the individual CRPA elements is needed for measurement of a synthesized null. For this purpose, the beamforming network in Fig. 3.18 was fabricated [42]. The beamforming network comprises four identical channels, each of which connect to a CRPA element. On each channel, the first device after the antenna is a low noise amplifier (LNA), followed by a power splitter. Half the power is sent to an SMA connector on the bottom of the PCB, for interfacing with the DSO. The remaining half of the power exiting the LNA is fed into an eight-bit variable phase shifter, PE 44820, which applies the desired phase with 1.4° resolution. Following this is another LNA for increased isolation and additional gain, followed by a SKY12343-364LF variable attenuator, with 0-

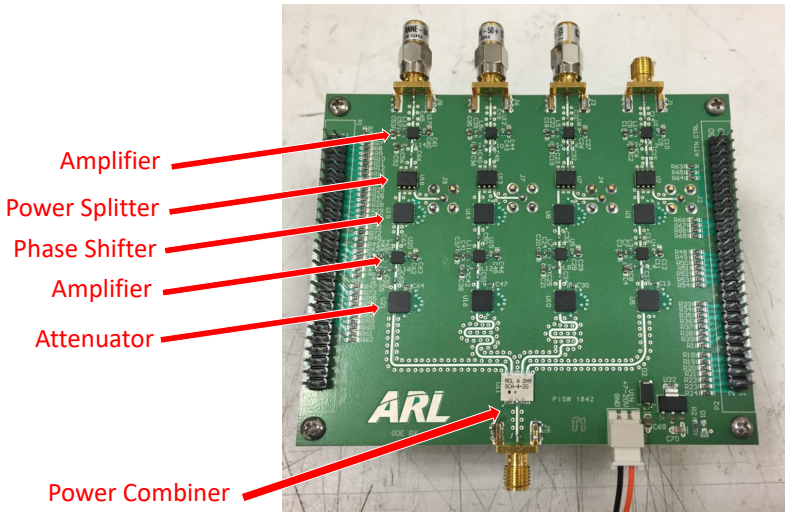

Figure 3.18: Beamforming receiver for GPS denied environment.

31.75 dB attenuation in 0.25 dB steps. Finally, all four channels are combined and output through an SMA connector for measurement.

Two commercial off-the-shelf dual linear antennas were placed on a 12 in ground plane with 4 in spacing, and connected to the beamforming network. Weights were calculated using the same constraint vectors, $\mathbf{e}_1$ and $\mathbf{e}_3$, introduced in Section 3.1. Recall that $\mathbf{e}_1$ implements a single LP port as a reference element, whereas $\mathbf{e}_3$ synthesizes an RHCP element from both ports on one antenna. Selected measurements are shown in Fig. 3.19 for $\mathbf{e}_3$ and patterns for $\mathbf{e}_1$ appear in Fig. 3.20. Measured results agreed with simulated results first reported in [16] and confirmed in [43], i.e. that better cancellation was achieved for the synthesized CP reference element than for the LP reference. Additionally, the CRPA reception pattern saw higher gain away from the jammer, partially due to the application of the weights. Despite the constraint vectors both being normalized vectors, it was decided that attenuating the ports on the reference channel would lessen the dynamic range of the measurement, and so a modified constraint vector, $\mathbf{e}_3 = [1 \;\; -j \;\; 0 \;\; 0]^\dagger$ was used in practice. This adds an additional 3 dB of gain to the active reception patterns in Fig. 3.19.

The receiver uses discrete state phase shifters and attenuators to apply the relative magnitude and phase weights, introducing errors compared to the double-precision floating point weights applied in simulation. The phase shifters also introduce a phase change that is not uniform across states, or even across devices. This must be corrected by the use

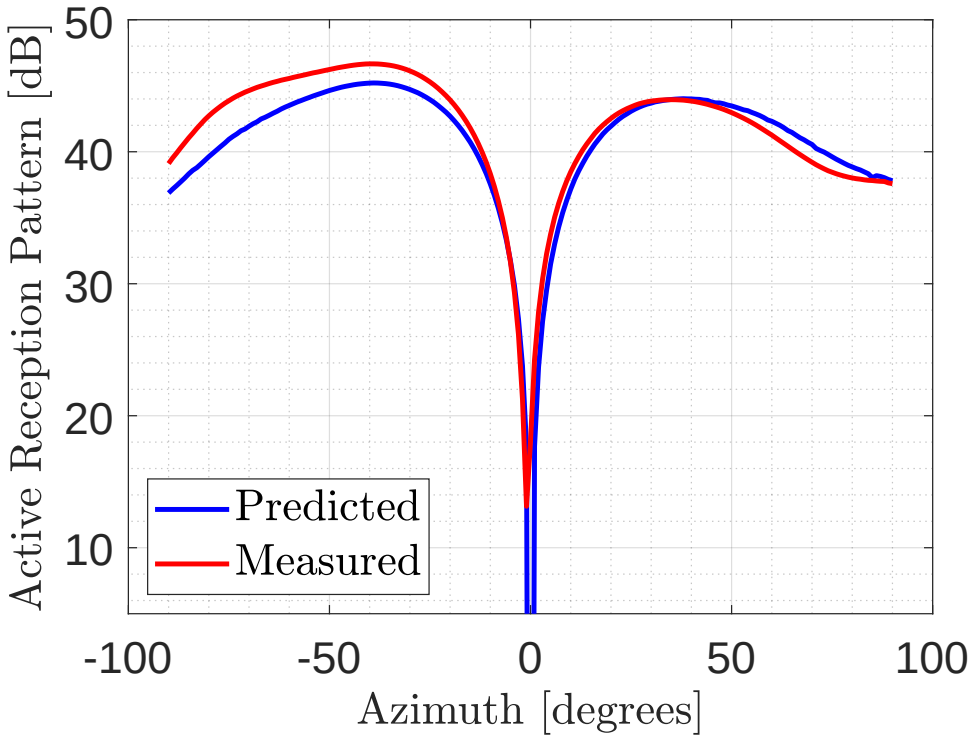

(a) Synthesized CP reference, jammer at 0°

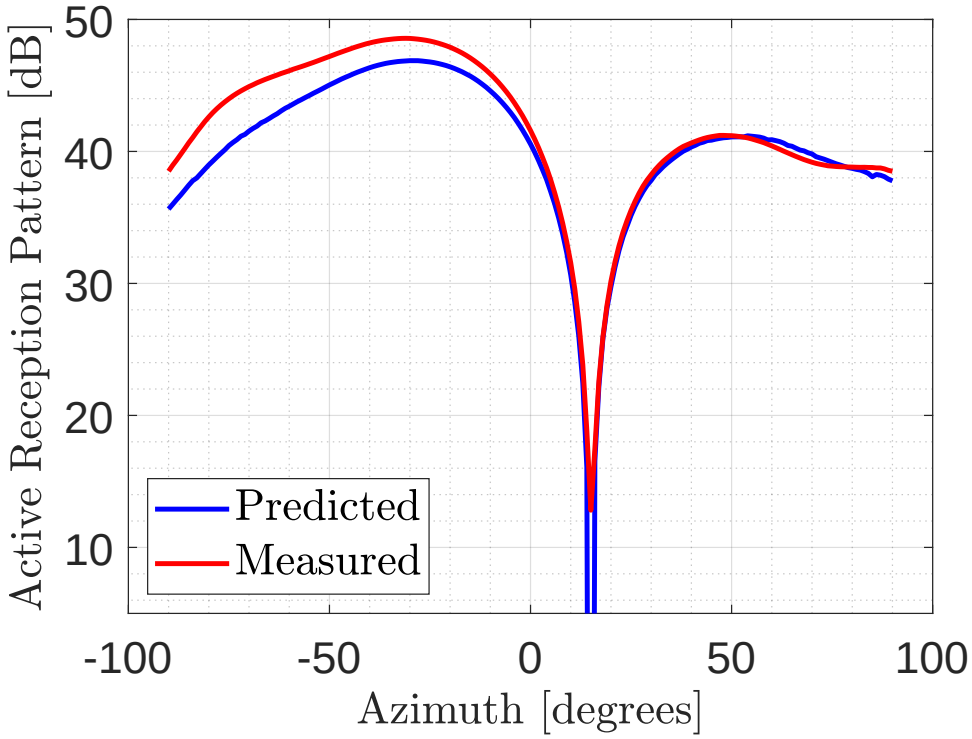

(b) Synthesized CP reference, jammer at 15°

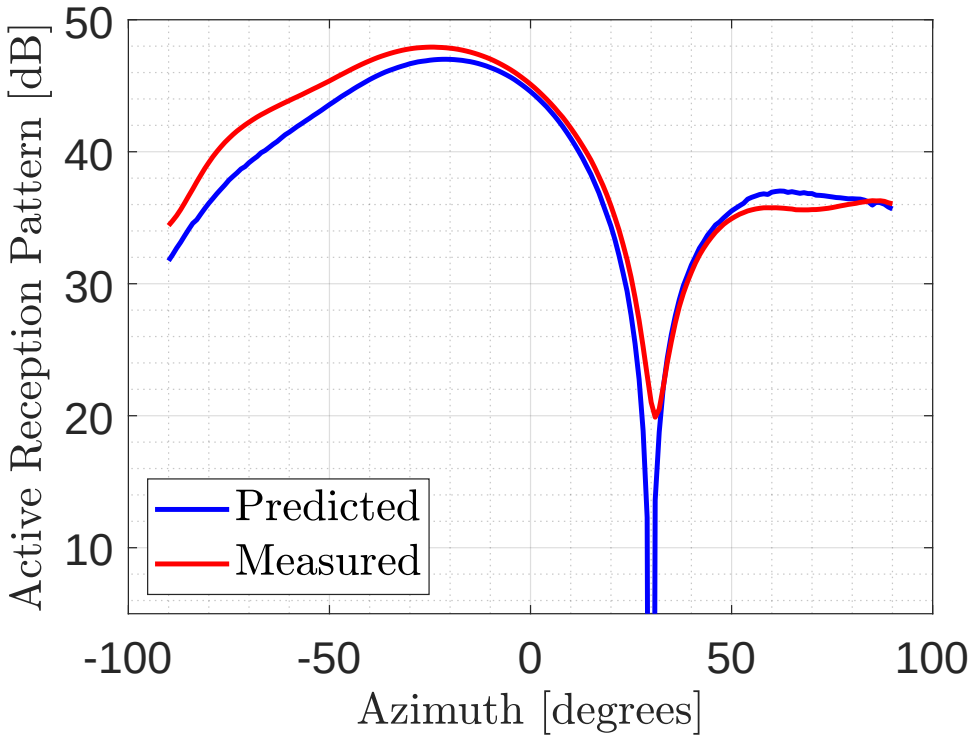

(c) Synthesized CP reference, jammer at 30°

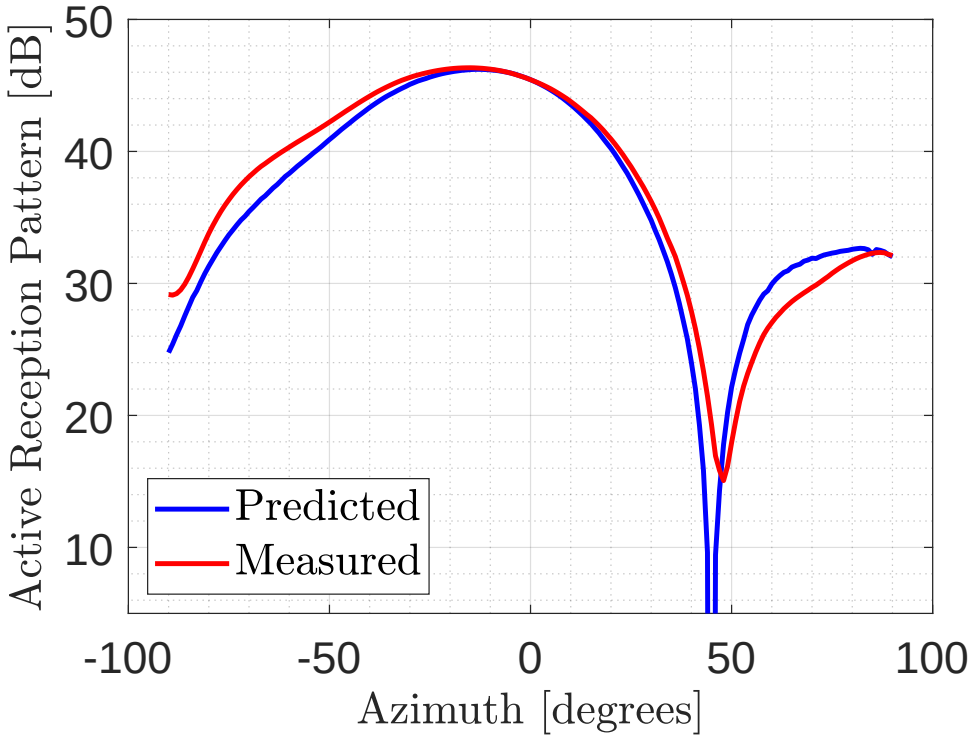

(d) Synthesized CP reference, jammer at 45°

Figure 3.19: Measured reception patterns using beamforming receiver and synthesized CP reference element.

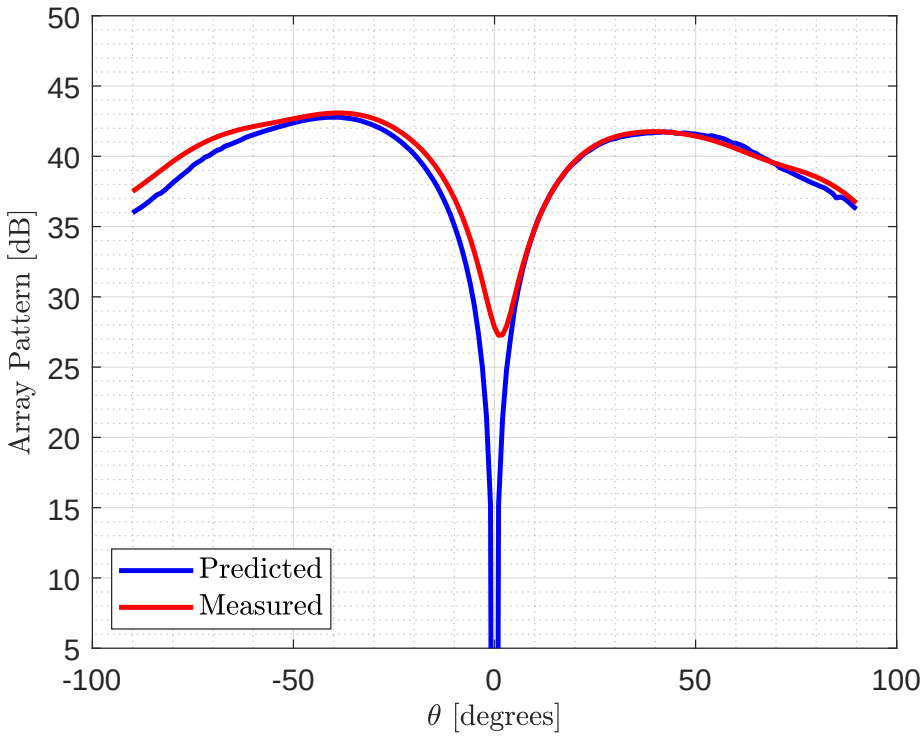

(a) LP reference, jammer at 0°

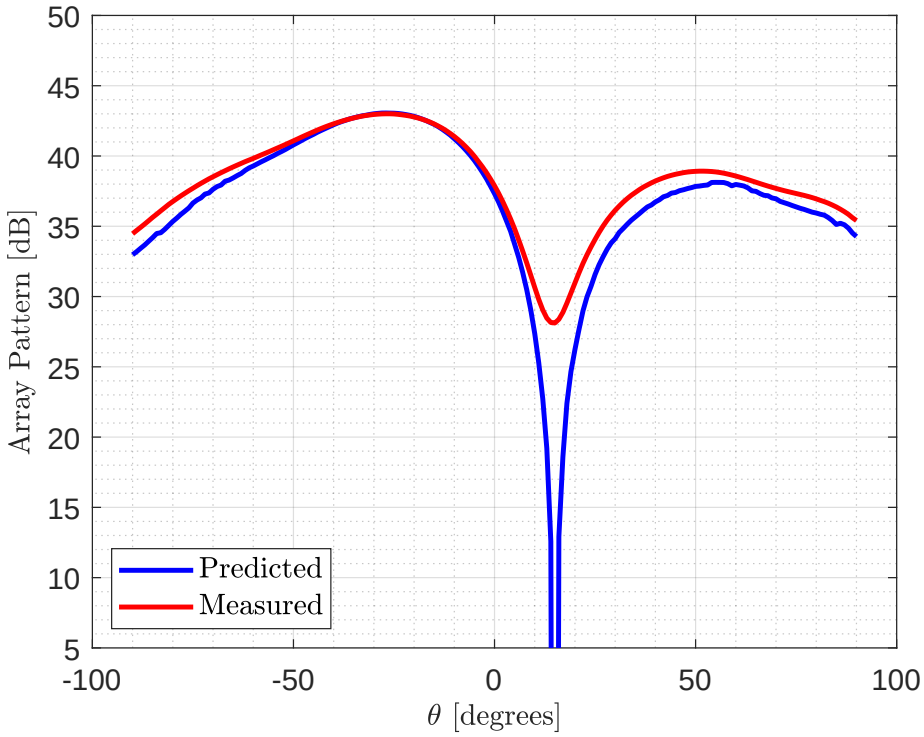

(b) LP reference, jammer at 15°

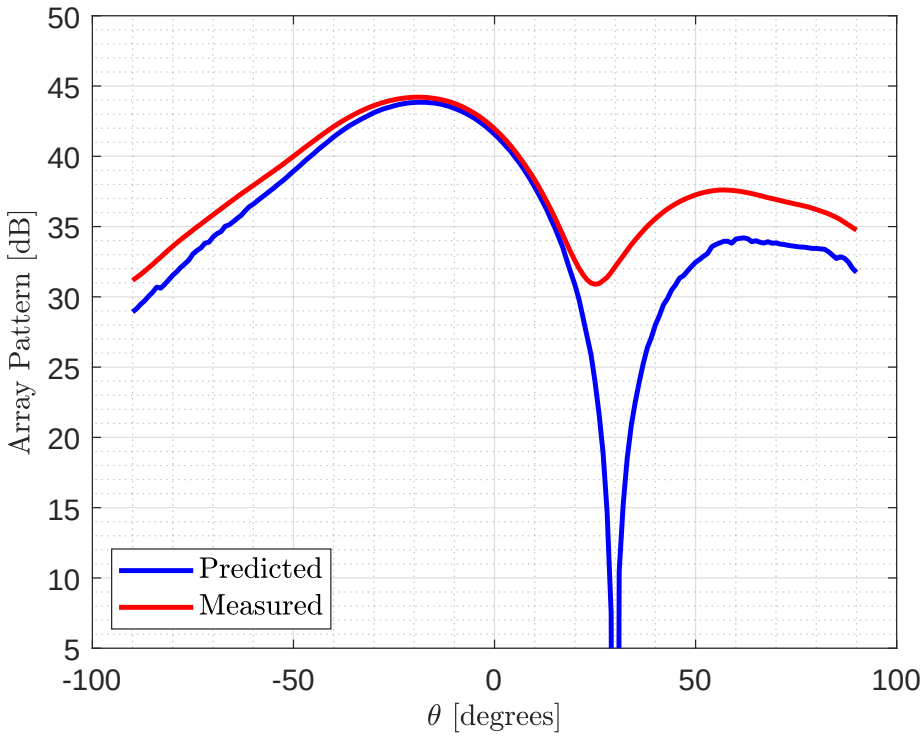

(c) LP reference, jammer at 30°

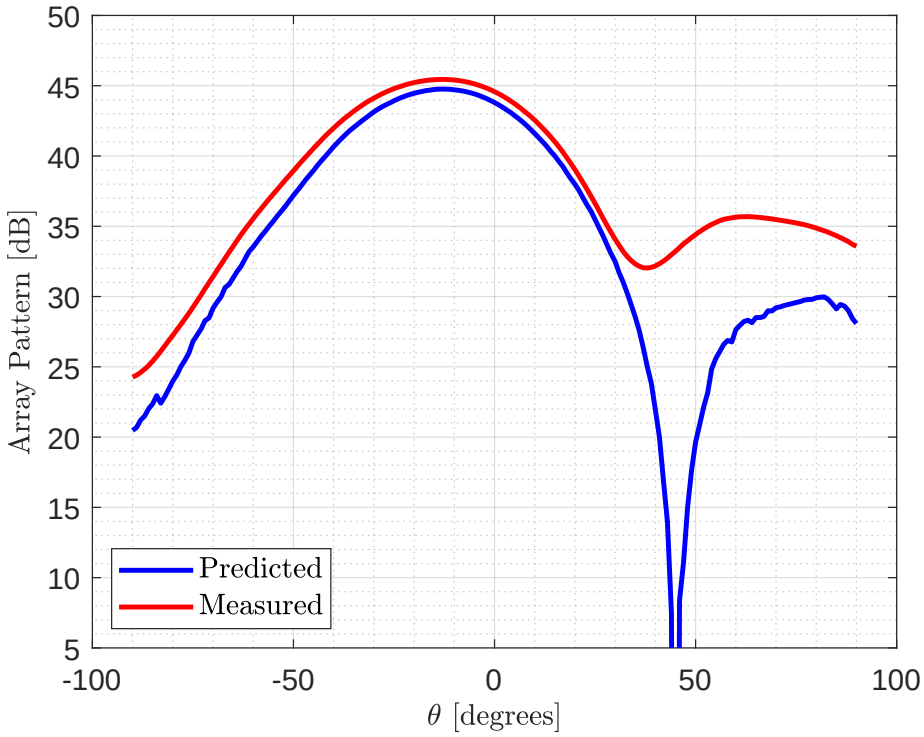

(d) LP reference, jammer at 45°

Figure 3.20: Measured reception patterns using beamforming receiver and linearly polarized reference element.

of a lookup table (LUT). Small errors in measurement as well as finite precision result in the null locations not always aligning with the jammer angle-of-arrival for all cases, e.g., Fig. 3.19d. In the absence of the large discretization errors present in hardware, the iterative algorithm applied in post-processing is able to reduce jammer power below the noise floor for a variety of jamming environments, achieving better jammer suppression than the hardware realization [40]. Additionally, in a fully realized CRPA design, each port must be sampled so that processing can be done on an embedded computer. For this reason, a digital implementation is preferred to an implementation using variable phase shifters and attenuators. The beamforming receiver in Fig. 3.18 is a useful piece of laboratory equipment, but is still far from a complete system ready to be fielded.

3.5 Discussion

Design of a CRPA must pass through several stages. One must walk before one can run, so to speak. Modeling the CRPA in software is a first step and can identify trends and candidate designs for further development. At this stage there are numerous tools at the disposal of a designer, ranging from idealized analytic models to commercially available numerical tools. Varying levels of model sophistication can produce varying degrees of accuracy in the model, though there are costs incurred with these higher fidelity models. Depending on the computational resources available, these costs may be may be a limiting factor.

Different techniques have different strengths, and having multiple tools in one's toolbox provides adaptability to the demands of a given goal. The Euler rotation technique is well suited to studies involving minor variations to design parameters or perturbations to an existing CRPA layout. For each of these investigations, the large number of variations on the CRPA design that must be modeled makes it impractical to use more sophisticated methods, such as MOM solvers. However, predictions made with the Euler rotation models must interpreted carefully, as mutual coupling effects present in the full-wave models have a large impact on overall performance.

Ultimately, measurements provide the most confidence in a design, as numerical models

will never capture the complexity of the real world. In a controlled environment, such as an anechoic chamber, it is possible to achieve decent cancellation of jammers even with a small number of elements. The laboratory equipment used to obtain these measurements is still far from a complete end-to-end system, and the environment is static and idealized in a way that a theater of combat will not be. In the following chapters, an attempt to model channel effects and multipath is presented, and the effects on CRPA performance is documented.

CHAPTER 4

MULTIPATH JAMMER MODELS

The modeling methods and measurements of Chapter 3 are all idealized in one common way; none of them account for realistic propagation effects. The element patterns are simulated in free space, and the measurements are done in an anechoic chamber, a room specifically designed to remove environmental effects. An end to end CRPA deployed in the field will not operate under such idealized conditions. Propagation effects and dynamically changing environments will produce an electromagnetic environment quite different from what has thus far been simulated.

Of chief concern is how well a man-portable CRPA, limited in degrees of freedom, can effectively cancel out interference due to multipath components of hostile jammers. Statistically independent jammers exhaust a degree of freedom for each jammer present, therefore two paths that a jammer takes to reach the receiver could potentially require a degree of freedom each, provided that these two components are statistically independent and sufficient power from the jammer arrives at the CRPA from each path. However, several multipath propagation models present in the literature are divorced from the specific geometric properties of a given environment, therefore there is a need for physical models tailored to the operating conditions the CRPA being modeled.

In this chapter, a scattering model specific to a GPS jamming environment is presented. First, two extreme forms of scattering, independent and fully correlated, are explored, and the conditions under which a CRPA will successfully mitigate interference identified. This is followed by the development of a mixed scattering model which combines aspects of specular and diffuse reflection. Finally, the jamming problem in the time domain is considered to

highlight the physical conditions which give rise to statistical dependence or independence.

A man-portable CRPA will undoubtedly experience dynamically changing propagation effects as the user moves through their environment. This application calls for models that can adapt to changing conditions as well as the CRPA and the soldier who carries it must be able to.

4.1 Generalized Scattering

The line-of-sight simulations and measurements presented in Chapter 3 do not take the effects of other objects into account. A CRPA operating in-situ will not be surrounded by electromagnetic absorber, as in the anechoic chamber, but rather will be located near reflective objects, or scatterers. Similarly, waves launched by the jammer may be scattered by objects local to the jammer as well as by distant objects. The multiple paths taken to the CRPA present a challenge to the null-steering problem in that the total interference from all paths must be canceled, and multipath components exhibiting statistical independence require additional degrees of freedom even when originating from a single jammer. It is possible for a single jammer to exhaust the CRPA degrees of freedom, provided that the multipath components are statistically independent.

The simplest multipath case that can be studied comprises a single jammer and a single scattering object. At the CRPA, two incident fields will be present: the line-of-sight field and the scattered field. Defining the global coordinate system in terms of the CRPA phase center, the position vector from the origin to the ith CRPA element is $\mathbf{r}_{oi} = [x_i, y_i, z_i]^T$. The position vector $\mathbf{r}_{oj}$ denotes the location of the jammer, and $\mathbf{r}_{os}$ is the position vector of the scatterer. Let the jammer's local coordinate system be defined by the unit vectors $(\mathbf{x}', \mathbf{y}', \mathbf{z}')$. The position vector originating at the jammer and ending at the CRPA origin, $\mathbf{r}_{jo} = -\mathbf{r}_{oj}$, can be expressed in the jammer-centric coordinates by applying the transform

$$\tilde{\mathbf{r}} = \begin{bmatrix} x_1' & x_2' & x_3' \\ y_1' & y_2' & y_3' \\ z_1' & z_2' & z_3' \end{bmatrix} \mathbf{r}. \tag{4.1}$$

The angles of incidence (θ_{oj}, ϕ_{oj}) for the CRPA and angles of departure for the jammer are found using

$$\theta_{oj} = \arccos \frac{z_{oj}}{\sqrt{x_{oj}^2 + y_{oj}^2 + z_{oj}^2}}, \tag{4.2}$$

$$\phi_{oj} = \arctan \frac{y_{oj}}{x_{oj}}, \tag{4.3}$$

for either coordinate system. Similarly, the vector $\mathbf{r}_{js} = \mathbf{r}_{os} - \mathbf{r}_{oj}$ can be expressed in either coordinate system, as can the angles between the scatterer and either the CRPA or the jammer.

The jammer radiation pattern will determine the line-of-sight fields present at the CRPA origin and at the scatterer, i.e.

$$\mathbf{E}_L(\mathbf{O}) = \tilde{\mathbf{E}}_L(\tilde{\mathbf{r}}_{jo}) = \frac{e^{-j\mathrm{k}R_{jo}}}{R_{jo}} \left[\boldsymbol{\theta}' E_\theta \left(\tilde{\theta}_{jo}, \tilde{\phi}_{jo} \right) + \boldsymbol{\phi}' E_\phi \left(\tilde{\theta}_{jo}, \tilde{\phi}_{jo} \right) \right], \tag{4.4}$$

$$\mathbf{E}_S(\mathbf{r}_{os}) = \tilde{\mathbf{E}}_S(\tilde{\mathbf{r}}_{js}) = \frac{e^{-j\mathrm{k}R_{js}}}{R_{js}} \left[\boldsymbol{\theta}' E_\theta \left(\tilde{\theta}_{js}, \tilde{\phi}_{js} \right) + \boldsymbol{\phi}' E_\phi \left(\tilde{\theta}_{js}, \tilde{\phi}_{js} \right) \right]. \tag{4.5}$$

The fields at the scatterer will be reflected towards the CRPA origin, with some reflection coefficient. To account for the mixing of polarizations the reflection coefficient matrix is defined as

$$\boldsymbol{\Gamma} = \begin{bmatrix} \Gamma_{\theta,\theta'} & \Gamma_{\theta,\phi'} \\ \Gamma_{\phi,\theta'} & \Gamma_{\phi,\phi'} \end{bmatrix}, \tag{4.6}$$

where $\Gamma_{\theta,\theta'}$ denotes the reflection coefficient for the $\boldsymbol{\theta}'$ component of the incident wave in jammer-local coordinates to the $\boldsymbol{\theta}$ component of the reflected wave in CRPA-centric coordinates, and so on [86]. Now the scattered fields at the CRPA origin are given by

$$\mathbf{E}_S(\mathbf{O}) = \frac{e^{-j\mathrm{k}R_{os}}}{R_{os}} \boldsymbol{\Gamma} \mathbf{E}_S(\mathbf{r}_{os}). \tag{4.7}$$

The open circuit voltage at the CRPA element ports are found from the vector effective heights,

$$[\mathbf{v}_{oc}]_i = \mathbf{h}_i(\theta_{oj}, \phi_{oj}) \cdot \mathbf{E}_L(\mathbf{O}) + \mathbf{h}_i(\theta_{os}, \phi_{os}) \cdot \mathbf{E}_S(\mathbf{O}). \tag{4.8}$$

This formulation can be extended to multiple scatterers by simply adding more terms,

though when considering multiple scatterers it is possible to have paths with more than one reflection. In the following, only paths with a single reflection are considered.

4.2 Fully Correlated Scattering

In order to examine the impact that statistical dependence plays in the null-steering problem, a simple case of the above generalized case is now developed. Let the jammer and the CRPA elements all have the radiation patterns of vertically oriented half-wavelength dipoles, there be exactly one scatterer, and let $\mathbf{\Gamma}$ from (4.6) will take the form

$$\mathbf{\Gamma} = \begin{bmatrix} 1 & 0 \\ 0 & 0 \end{bmatrix}. \tag{4.9}$$

Here, it is assumed that the incident fields from the jammer are fully reflected by the scatterer and that the polarization of the reflected component is unchanged and matches that of the CRPA.

The input vector at the receiver is a sum of thermal noise, $\mathbf{x}_N$, the voltage induced by the line-of-sight jammer, $\mathbf{x}_j$, and the voltage induced by the scattered fields, $\mathbf{x}_s$. To examine the extreme cases of independent and fully correlated scattering, the covariance matrix must be examined,

$$\mathbf{R} = \mathrm{E}\left[(\mathbf{x}_N + \mathbf{x}_j + \mathbf{x}_s)(\mathbf{x}_N + \mathbf{x}_j + \mathbf{x}_s)^\dagger\right] = \sigma^2\mathbf{I} + \mathrm{E}\left[(\mathbf{x}_j + \mathbf{x}_s)(\mathbf{x}_j + \mathbf{x}_s)^\dagger\right] . \tag{4.10}$$

The thermal noise is assumed to be Gaussian and can be separated from the other terms in the expectation. The remaining term on the right-hand side comprising the line-of-sight and scattered interference is referred to as the partial covariance matrix, $\overline{\mathbf{R}}$. Expanding out $\overline{\mathbf{R}}$ gives

$$\overline{\mathbf{R}} = \mathrm{E}\left[\mathbf{x}_j\mathbf{x}_j^\dagger + \mathbf{x}_s\mathbf{x}_s^\dagger + \mathbf{x}_j\mathbf{x}_s^\dagger + \mathbf{x}_s\mathbf{x}_j^\dagger\right]. \tag{4.11}$$

Under the independence assumption, $\mathbf{x}_j$ and $\mathbf{x}_s$ are uncorrelated, and so the expectation of the cross-terms, $\mathbf{x}_j\mathbf{x}_s$ and $\mathbf{x}_s\mathbf{x}_j$, are both $\mathbf{0}$. The only contributions to the covariance

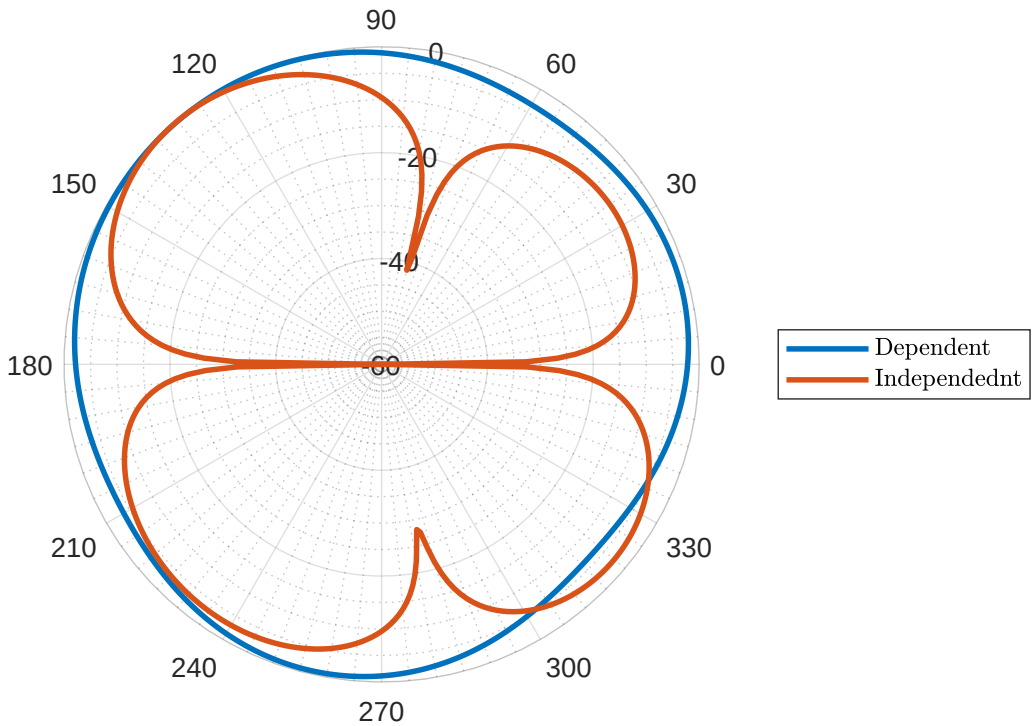

Figure 4.1: Plane wave reception patterns for dependent and independent formulations with $M = 1$ scatterers.

matrix come from the like-terms, $\mathbf{x}_j\mathbf{x}_j^\dagger$ and $\mathbf{x}_s\mathbf{x}_s^\dagger$. However, if it is assumed the two paths are fully correlated, i.e. the two components add coherently at the receiver with a phase difference due only to the path lengths and the deterministic reflection coefficient, then all four terms contribute to $\overline{\mathbf{R}}$.

The independent partial covariance matrix,

$$\overline{\mathbf{R}}_I = \mathbf{x}_j\mathbf{x}_j^\dagger + \mathbf{x}_s\mathbf{x}_s^\dagger, \tag{4.12}$$

is a rank two matrix. If the number of scatterers increases to $M > 1$, then $\overline{\mathbf{R}}_I$ becomes a rank $M + 1$ matrix unless the number of scatterers meets or exceeds the number of CRPA elements, $N \geq M$, in which case $\overline{\mathbf{R}}_I$ is full-rank. However, the dependent partial covariance

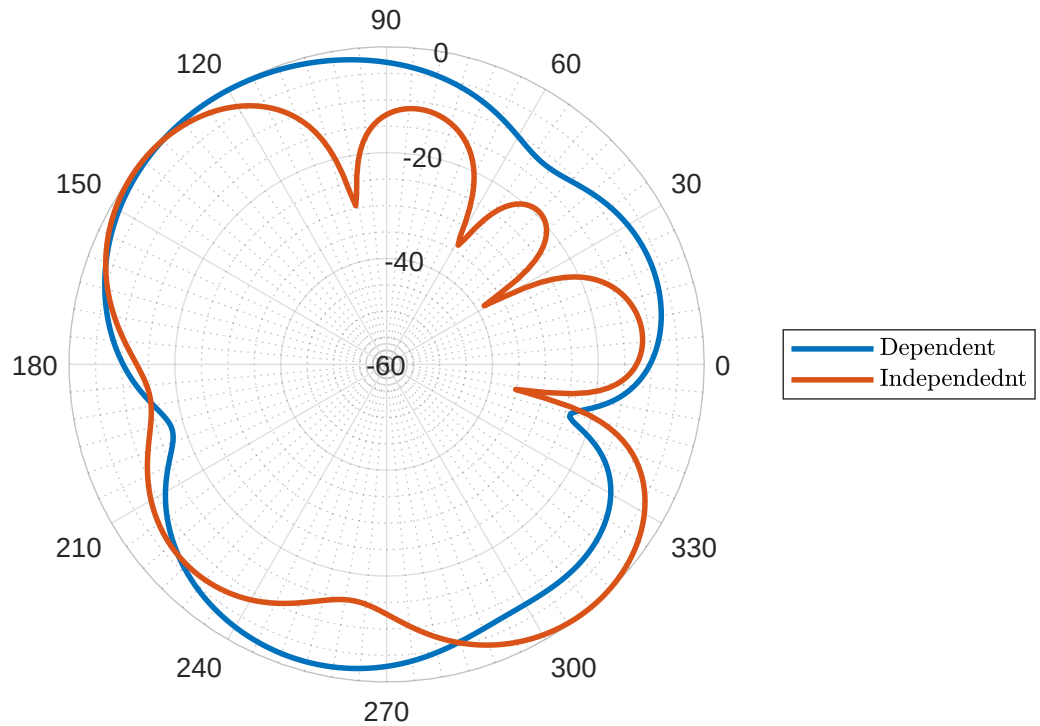

Figure 4.2: Plane wave reception patterns for dependent and independent formulations with $M = 10$ scatterers. The CRPA degrees are overwhelmed under the independence assumption.

matrix,

$$\overline{\mathbf{R}}_D = \left(\mathbf{x}_j + \mathbf{x}_s\right)\left(\mathbf{x}_j + \mathbf{x}_s\right)^\dagger = \mathbf{x}_j\mathbf{x}_j^\dagger + \mathbf{x}_s\mathbf{x}_s^\dagger + \mathbf{x}_j\mathbf{x}_s^\dagger + \mathbf{x}_s\mathbf{x}_j^\dagger \ , \tag{4.13}$$

is a rank one matrix, because each row is a scalar multiple of the vector $\mathbf{x}_j + \mathbf{x}_s$. This is true for $M \geq 1$ scatterers, in fact any number of incident fields adding coherently in this manner present effectively one "jammer" to the CRPA. Although, it should be noted that this effective jammer will not have the same form as a plane wave from any particular direction, and one should not anticipate a distinct radiation pattern null associated with it.

Figure 4.1 shows the normalized reception patterns for a four element planar array with weights calculated from both independent and dependent formulations of $\mathbf{R}$. The independent case has two distinct nulls, one in the DOA of the jammer and the other in the angle-of-arrival of the scatterer, whereas the dependent case does not show any nulls at all.

However, when examining the output power, $\mathbf{w}^\dagger\mathbf{R}\mathbf{w}$, in each case, the output is reduced to the noise floor with the independent and dependent cases yielding output powers of 2.9 and 0.5 dB relative to the noise power, respectively. These values are equal to the norm squared of the respective weight vectors, $\|\mathbf{w}_I\|^2$ and $\|\mathbf{w}_D\|^2$. In each of these cases the interference from both paths taken by the jammer is eliminated.

Each of the formulations, independent and dependent, have been shown to successfully mitigate a jammer and a single reflection, however the difference between these formulations becomes more apparent when considering multiple scatterers. Figure 4.2 shows the normalized plane wave reception patterns for $M = 10$ scatterers. Here the independent weights result in a pattern which steers nulls towards some of the incident fields, but the CRPA lacks the degrees of freedom to effectively cancel all of the interference. The dependent weights do exhibit one feature resembling a null, howeverthis feature seems to be merely coincidental and the overall pattern does not have much directional variation. The differences between the two cases are more apparent when examining the output power. Once again the output power for the dependent case, $\mathbf{w}_D^\dagger\mathbf{R}_D\mathbf{w}_D$, is 2.0 dB greater than the noise power, a factor equal to $\|\mathbf{w}_D\|^2$. However for the independent case $\mathbf{w}_I^\dagger\mathbf{R}_I\mathbf{w}_I$ is 61.6 dB relative to the noise power. The independent formulation fails to cancel the interference, as is expected considering the degrees of freedom available. Each of the paths taken produces an independent field at the CRPA, and each field requires a degree of freedom to be canceled out. The fully correlated formulation, however, is able to cancel the coherent field at the CRPA with only a single degree of freedom. For a CRPA operating in a purely deterministic, fully-correlated scattering environment, it is always possible to find a set of weights which fully cancels the interference.

A more detailed investigation into the CRPA output power and the eigenvalues of $\overline{\mathbf{R}}$ is instructive in this matter. The output noise power, i.e. the portion of the output attributable to the thermal noise only, increases with the norm of the weight vector,

$$P_n = \mathbf{w}^\dagger \mathrm{E}\left[\mathbf{x}_N\mathbf{x}_N^\dagger\right]\mathbf{w} = \sigma^2\|\mathbf{w}\|^2 \ . \tag{4.14}$$

Some noise will pass through the system, and weighting does increase the output noise

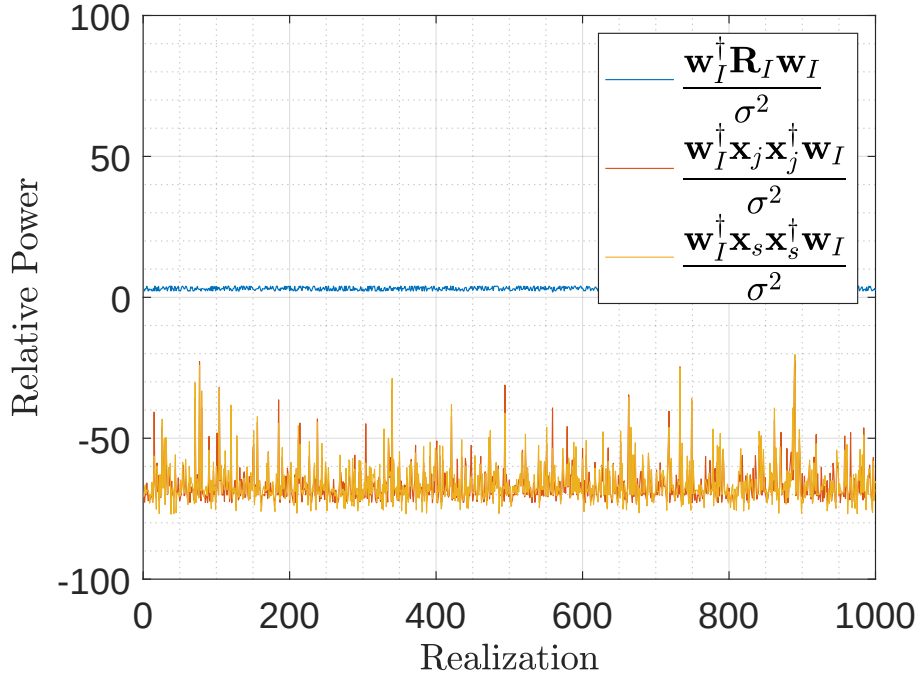

(a) Output power, independent formulation, $M = 1$ Scatterer.

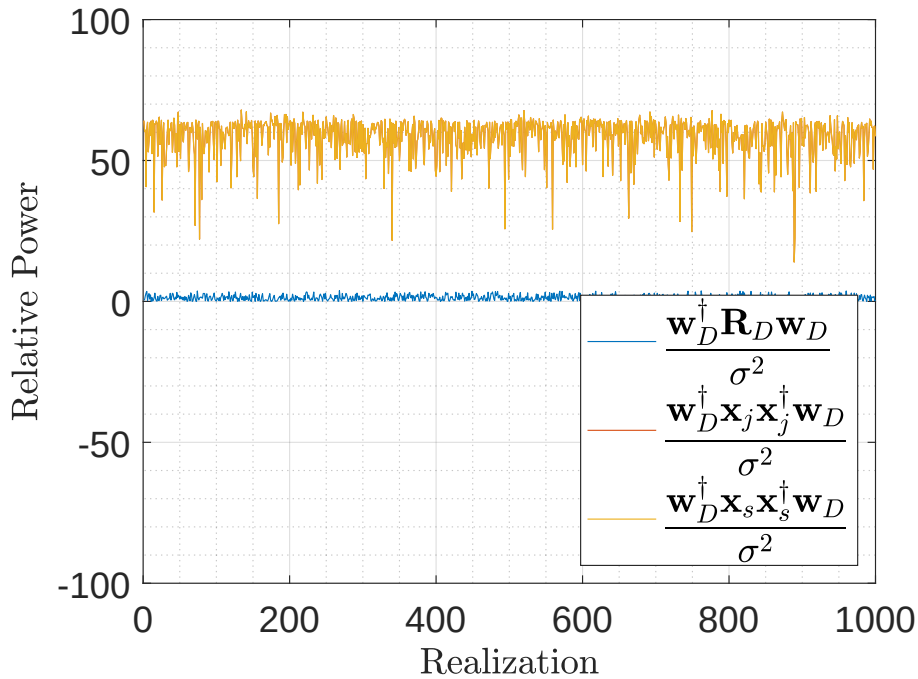

(b) Output power, dependent formulation, $M = 1$ Scatterer.

Figure 4.3: Relative power levels for independent and dependent formulations.

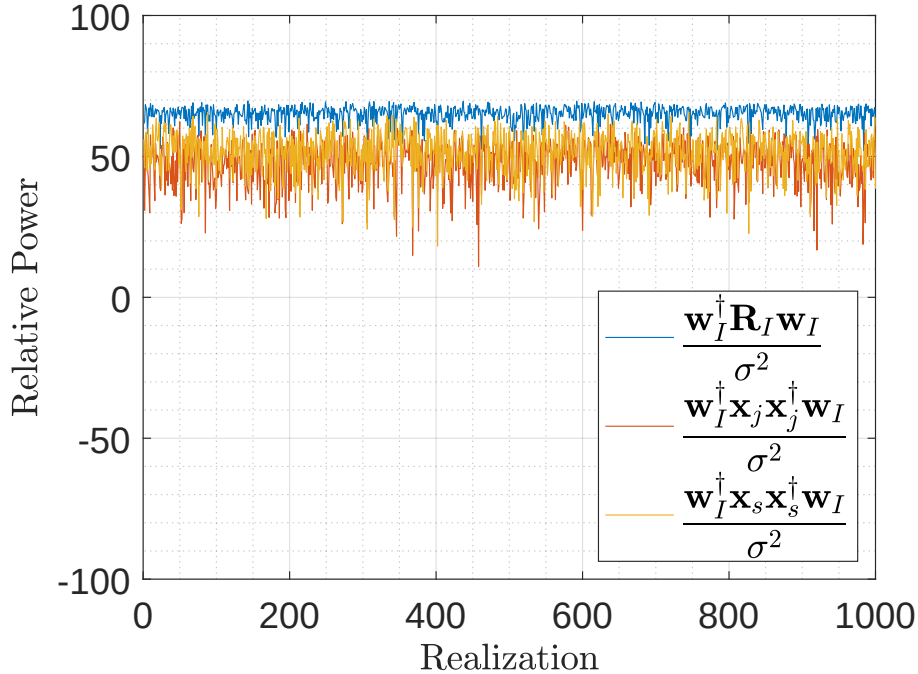

(a) Output power, independent formulation, $M = 10$ Scatterers.

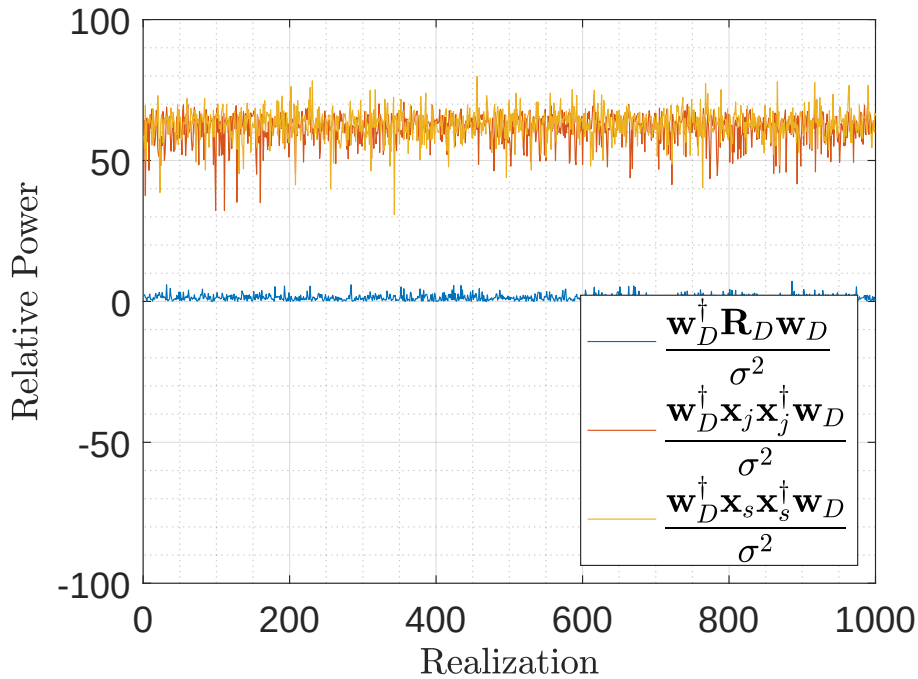

(b) Output power, dependent formulation, $M = 10$ Scatterers.

Figure 4.4: Relative power levels for independent and dependent formulations.

power, though the noise is incoherent and adds in power rather than in amplitude. For the weights to be effective in the independent case, the independent output powers,

$$P_{j,s} = \mathbf{w}^{\dagger}\mathbf{x}_{j,s}\mathbf{x}_{j,s}^{\dagger}\mathbf{w} \ , \tag{4.15}$$

must both be reduced to the noise floor or below. Note that for either the line-of-sight or the scattered components (4.15) is non-negative definite. Conversely for the dependent formulation, it is not necessary that (4.15) be below the noise floor because the two cross-terms in (4.13),

$$\mathbf{w}^{\dagger}\mathbf{x}_{s,j}\mathbf{x}_{j,s}^{\dagger}\mathbf{w} \ , \tag{4.16}$$

are present in the sum. Note that the two cross-terms are complex conjugates and their sum will be strictly real, though not necessarily positive. If the sum of the cross-terms is equal in magnitude to the sum of the co-terms, but with an opposite sign, the total output will be zero.

For multiple realizations, the individual power terms were recorded and compared to the overall output power. These powers relative to the noise are shown in Fig. 4.3. The output power in both cases is slightly higher than the noise power, as is expected from (4.14). However, the independent formulation produces a weight vector which cancels both the line-of-sight and the scattered interference individually, whereas the dependent formulation produces weights which do not. The red trace in 4.3b shows the power in the individual terms to be far greater than the noise power, though the coherent sum of all four terms produces an overall output power similar to the independent case. In each instance, the CRPA is capable of eliminating the interference.

Increasing the number of scatterers to $M = 10$ overwhelms the CRPA in the independent case but not in the dependent case as can be seen in Fig. 4.4. Similar to what was seen in the single realization depicted in Fig. 4.2, across multiple realizations the independent scattering environment produces too many independent fields at the CRPA to be canceled. Independent components exceeding the degrees of freedom overwhelm the CRPA and interrupt GPS service.

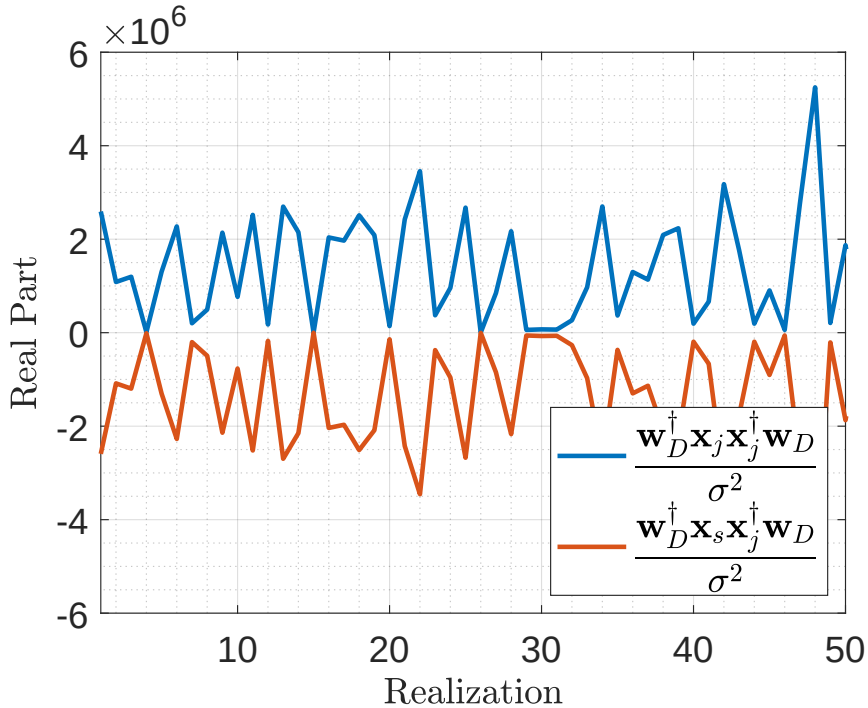

Figure 4.5: Real part of the co-terms and cross-terms.

However, the output power under the dependent formulation, shown as the blue trace in Fig. 4.4b is equal to the noise power scaled by the norm of the null-steering weights. The conditions described above, whereby the cross-terms and co-terms cancel one another out, are demonstrated in Fig. 4.5, in which the first 50 realizations are highlighted for clarity. The cross-terms are equal and opposite to the co-terms, and their sum is zero to working numerical precision. This indicates complete cancellation of the jammer and any number of multipath components provided they are fully correlated.

Closer inspection of the matrix inversion equation, (2.5), shows how this is accomplished. The denominator, $\mathbf{e}^\dagger \mathbf{R}^{-1} \mathbf{e}$, is the Lagrange multiplier, and may be ignored for the present discussion. Considering only the numerator, $\mathbf{R}^{-1}\mathbf{e}$, offers a geometric interpretation. The constraint vector is transformed by the inverse covariance matrix to generate the weight vector, and so the structure of $\mathbf{R}$ and $\mathbf{R}^{-1}$ is illuminating. If the interference power at the receiver is large relative to the noise power, the eigenvalues of $\overline{\mathbf{R}}_I$ are large relative to the eigenvalues of the noise contribution, σ^2. Given that $\mathbf{R}$ is a hermetian matrix, it shares its eigenvectors with its inverse, and eigenvalues associated with the same eigenvetor

are reciprocal to one another. This means that $\mathbf{w}$ is found by compressing the portions of $\mathbf{e}$ in the directions corresponding to the interference eigenvectors. The desired weight vector is then nearly perpendicular to the eigenvectors associated with the interference. However, when $M \geq N$, the interference eigenvectors span the entire space, and it is impossible cancel each of the independent paths simultaneously. This is one interpretation of what is meant by exhausting the CRPA degrees of freedom.

For the dependent case, $\overline{\mathbf{R}}_D$ is always rank one, so this condition is never met. In the N-dimensional signal space, there is only one eigenvector associated with the jammer, as all paths are linearly dependent.

To demonstrate this, multiple realizations were simulated in MATLAB with a single jammer and either $M = 1$ or $M = 10$ scatterers placed randomly within a 1 km radius of the receiver. In each case, independent and dependent formulations of $\overline{\mathbf{R}}$ were made, and the eigenvalues of each were recorded. The results are shown in Fig. 4.6. The single scatterer case is shown in Fig. 4.6a and 4.6b. The dependent formulation clearly has only one major eigenvalue, i.e. one eigenvalue that is much larger in magnitude than the smallest eigenvalue. Conversely, the independent formulation shows that $\overline{\mathbf{R}}_I$ has two major eigenvalues. When M is increased to 10 scatterers, the number of major eigenvalues remains unchanged at one for $\overline{\mathbf{R}}_D$, however the independent formulation shows that all the eigenvalues are large relative to the noise power, and $\overline{\mathbf{R}}_I$ is full rank. As can be seen, the number of eigenvalues large relative to noise power is directly related to the number of scatterers in the independent formulation. However, the number of major eigenvalues is invariant with respect to the number of scatterers for the dependent formulation, where the minor eigenvalues are effectively zero.

Here it has been shown that statistical dependence plays a large role in the operation of a CRPA in a multipath environment. At one extreme, the multiple components can be modeled as independent form the line-of-sight component as well as from one another. If enough components are present, and the power in each is large relative to the noise, the CRPA will be overwhelmed and no null-steering solution is possible. At the other extreme, if all paths add coherently, there is effectively on one jammer present at the receiver, and only one degree of freedom is required to fully cancel it. In a realistic environment, it is likely

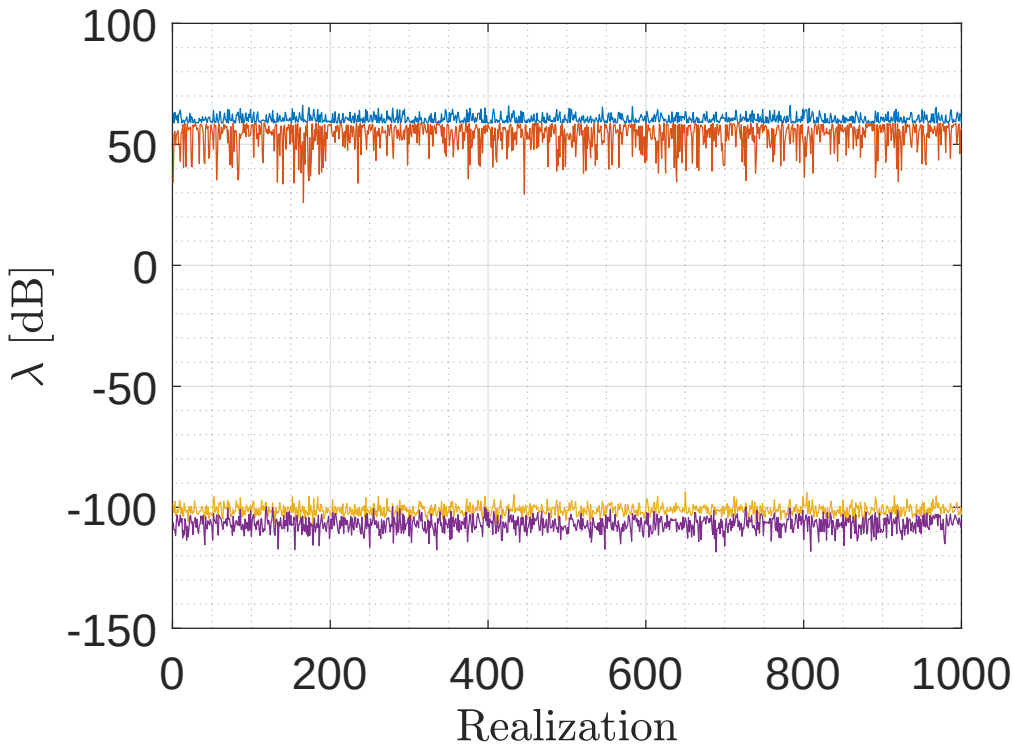

(a) Eigenvalues of $\overline{\mathbf{R}}_I$, $M = 1$ Scatterer.

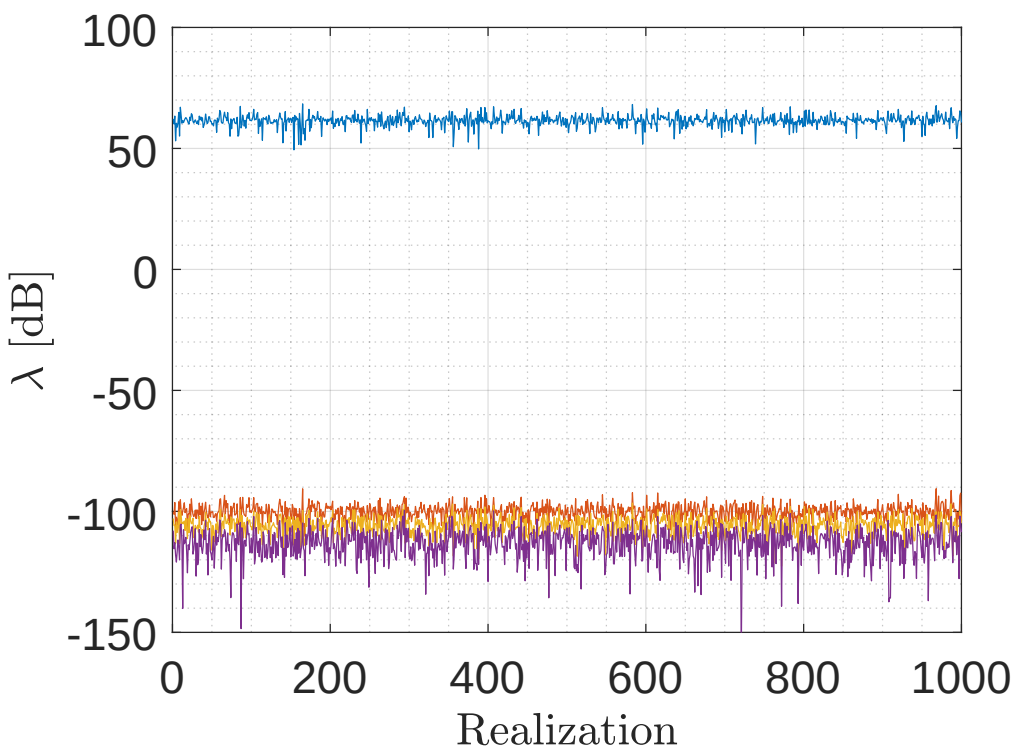

(b) Eigenvalues of $\overline{\mathbf{R}}_D$, $M = 1$ Scatterer.

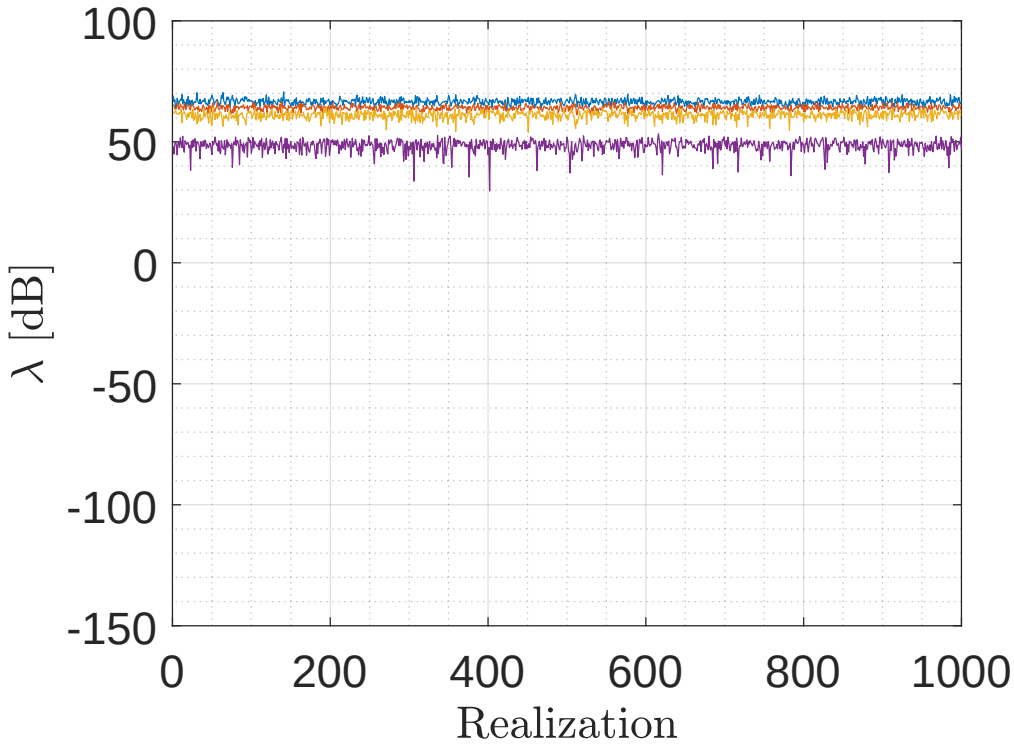

(c) Eigenvalues of $\overline{\mathbf{R}}_I$, $M = 10$ Scatterers.

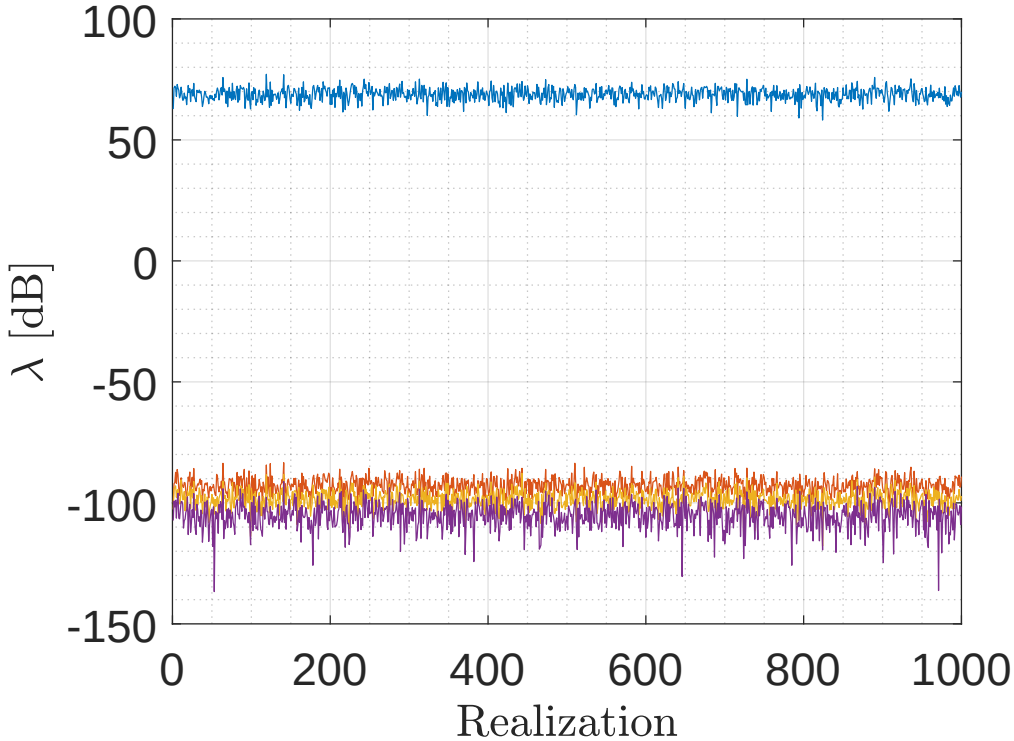

(d) Eigenvalues of $\overline{\mathbf{R}}_D$, $M = 10$ Scatterers.

Figure 4.6: Eigenvalues of the partial covariance matrix under fully independent and fully dependent assumptions.

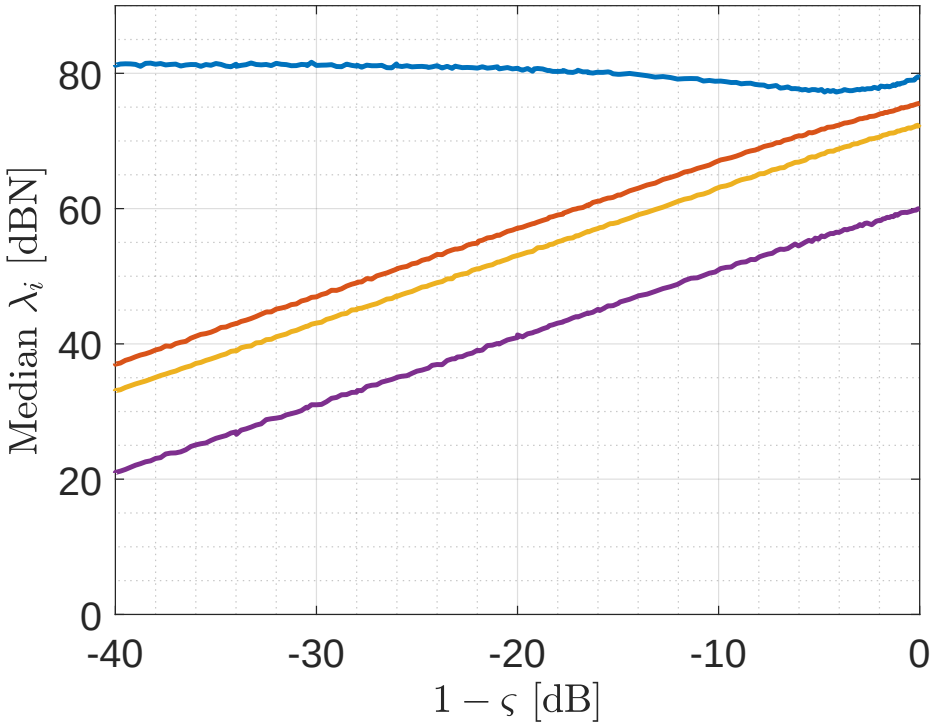

(a) $\Gamma_{md} = 1$, $\Gamma_{ms} = 1$.

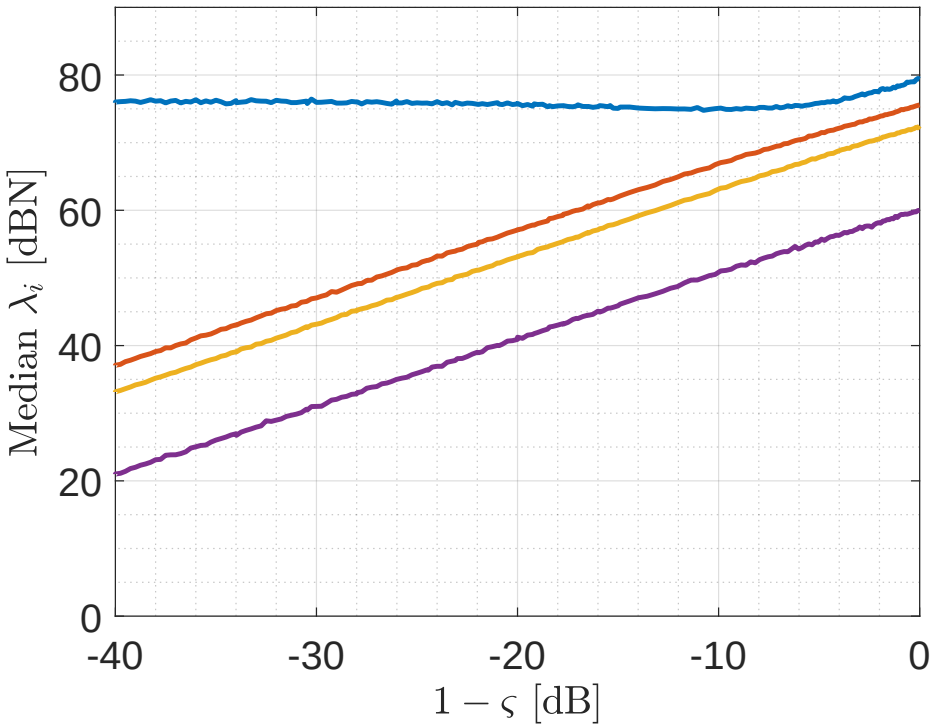

(b) $\Gamma_{md} = 1$, $\Gamma_{ms} = \frac{1}{2}$.

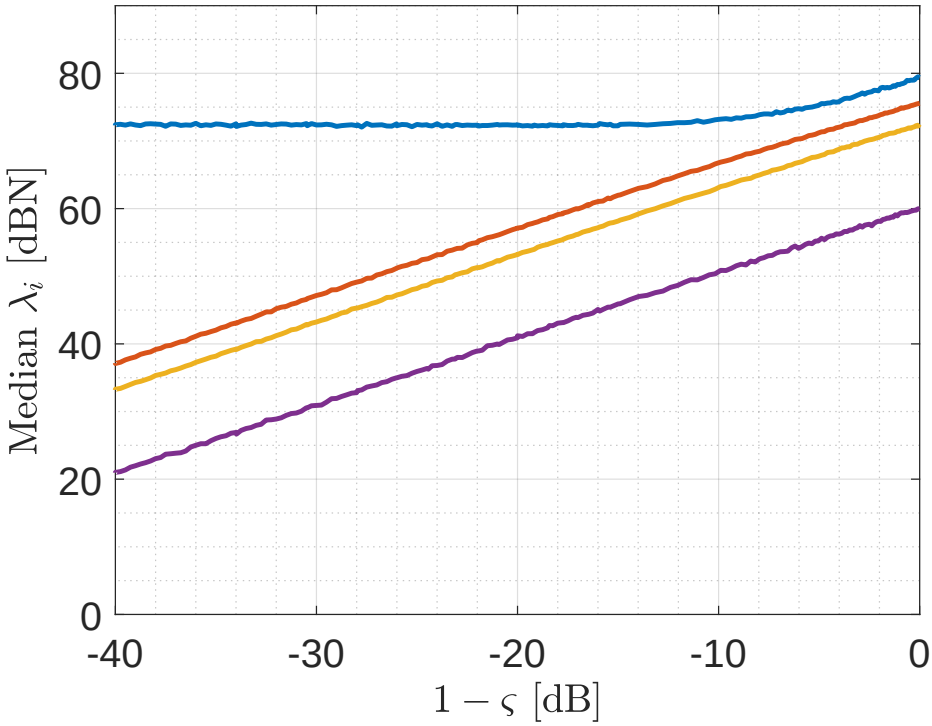

(c) $\Gamma_{md} = 1$, $\Gamma_{ms} = \frac{1}{4}$.

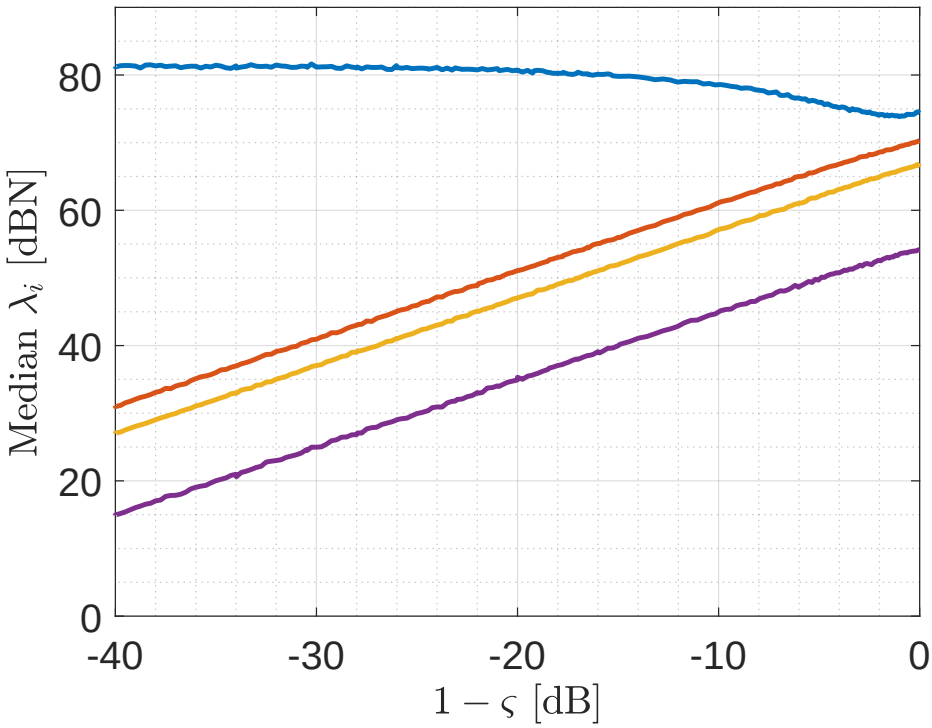

(d) $\Gamma_{md} = \frac{1}{2}$, $\Gamma_{ms} = 1$.

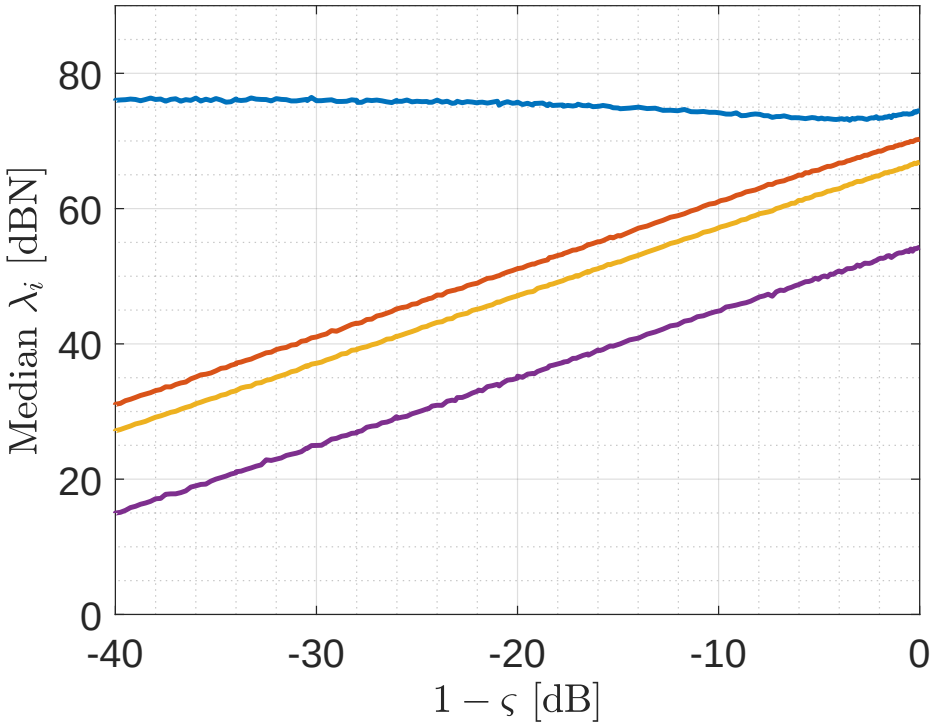

(e) $\Gamma_{md} = \frac{1}{2}$, $\Gamma_{ms} = \frac{1}{2}$.

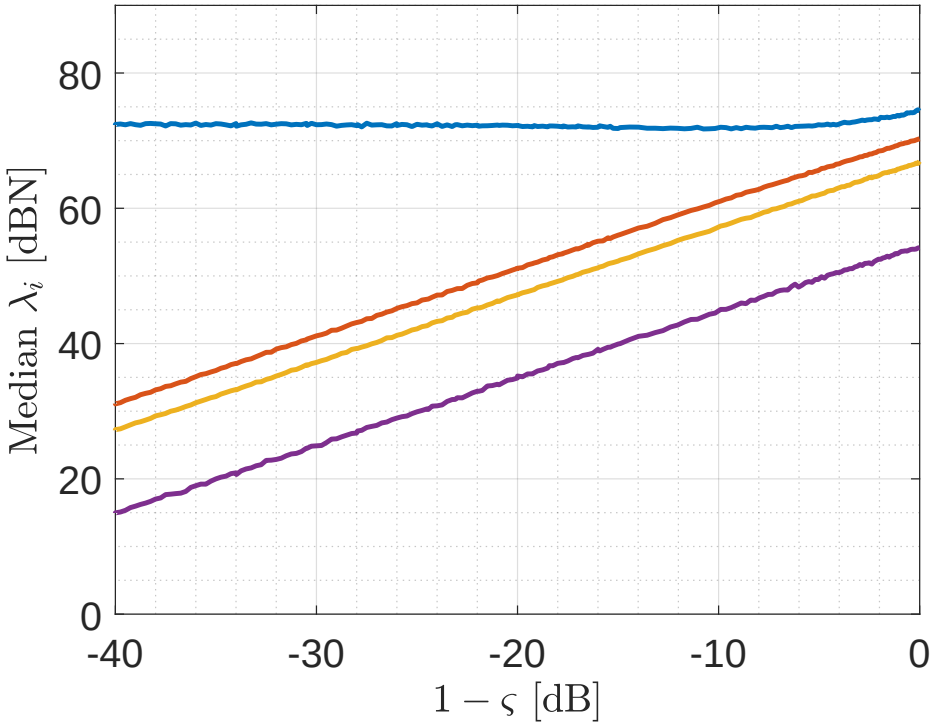

(f) $\Gamma_{md} = \frac{1}{2}$, $\Gamma_{ms} = \frac{1}{4}$.

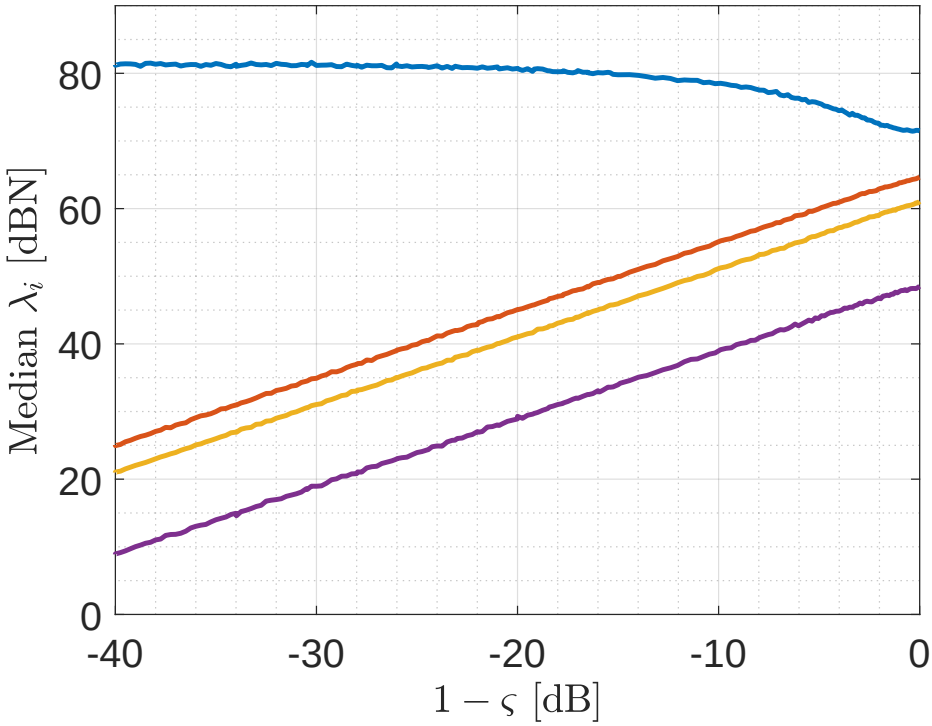

(g) $\Gamma_{md} = \frac{1}{4}$, $\Gamma_{ms} = 1$.

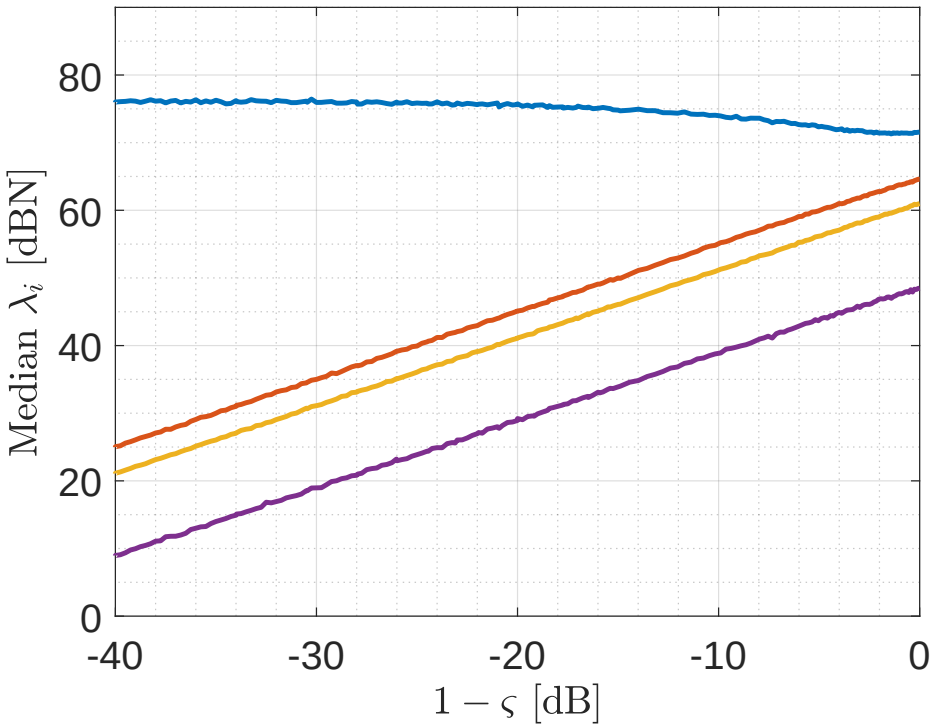

(h) $\Gamma_{md} = \frac{1}{4}$, $\Gamma_{ms} = \frac{1}{2}$.

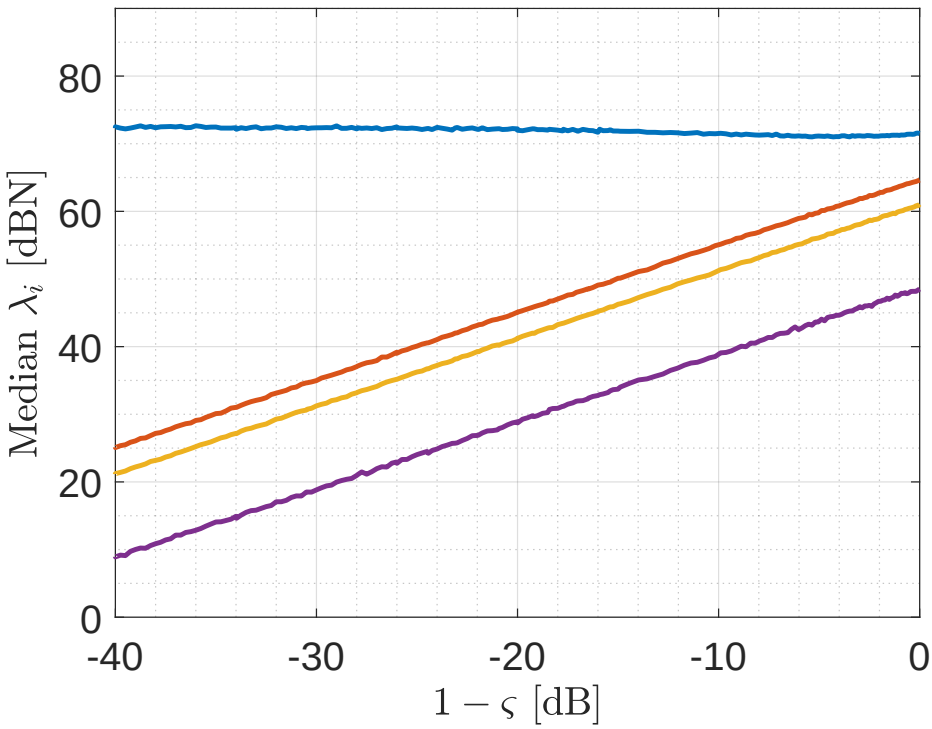

(i) $\Gamma_{md} = \frac{1}{4}$, $\Gamma_{ms} = \frac{1}{4}$.

Figure 4.7: Eigenvalues of $\overline{\mathbf{R}}_M$ for varying values of Γ_{md} and Γ_{ms}.

that neither of these conditions will be met, and a more general scattering environment model is needed.

4.3 Mixed Scattering

If the reflection coefficient of a scatterer is modeled to behave randomly, it is possible to formulate the covariance matrix as neither altogether independent nor completely dependent. Physical scattering environments encountered in practice are not likely to fall into either of these two extremes, therefore a middle ground formulation becomes necessary for predicting CRPA performance in physical environments. What follows is a parametric approach to modeling scattering as a combination of diffuse and specular, or statistically independent and dependent, reflection.

Consider a reflection coefficient which comprises both specular and diffuse reflection. The specular reflection is deterministic resulting in variations that depend only on the geometry of a given jamming environment. The diffuse reflection has a random phase, $\xi \sim \mathrm{U}\left[0, 2\pi\right]$, which will give rise to a scattered field that is statistically independent from the line-of-sight jammer. Let the specular and diffuse reflection coefficients be limited by some maximum values, Γ_{ms} and Γ_{md}, respectively, and the proportion of specular to diffuse reflection be controlled by a variable $0 \leq \varsigma \leq 1$, henceforth called the specular reflection factor. Now, Γ is written as

$$\Gamma = \varsigma \Gamma_{ms} + \left(1 - \varsigma\right) \Gamma_{md} e^{j\xi}. \tag{4.17}$$

Let $\mathbf{x}_s = \Gamma \tilde{\mathbf{x}}_s$ be the scattered jammer at the CRPA, with $\tilde{\mathbf{x}}_s$ is completely deterministic and dependent on path loss, phase propagation, and antenna element radiation patterns. Generalizing to multiple scatterers, $\mathbf{x}$ observed at the CRPA is written

$$\mathbf{x} = \mathbf{x}_N + \mathbf{x}_j + \sum_{m=1}^{M} \mathbf{x}_{s,m} = \mathbf{x}_N + \mathbf{x}_j + \sum_{m=1}^{M} \Gamma_m \tilde{\mathbf{x}}_{s,m}. \tag{4.18}$$

Now, the mixed scattering covariance matrix is defined as

$$\mathbf{R}_M = \mathrm{E}\left[\mathbf{x}\mathbf{x}^\dagger\right] = \sigma^2\mathbf{I} + \overline{\mathbf{R}}_M, \tag{4.19}$$

and removing the AWGN component gives us the partial mixed scattering covariance matrix,

$$\overline{\mathbf{R}}_M = \mathbf{x}_j\mathbf{x}_j^\dagger + \sum_{n=1}^{M}\sum_{m=1}^{M}\mathrm{E}\left[\Gamma_n\Gamma_m^*\right]\tilde{\mathbf{x}}_{s,n}\tilde{\mathbf{x}}_{s,m}^\dagger + \sum_{p=1}^{M}\mathrm{E}\left[\Gamma_p\right]\tilde{\mathbf{x}}_{s,p}\mathbf{x}_j^\dagger + \sum_{q=1}^{M}\mathrm{E}\left[\Gamma_q^*\right]\mathbf{x}_j\tilde{\mathbf{x}}_{s,q}^\dagger\ . \tag{4.20}$$

Taking the expectation of (4.17) eliminates the diffuse portion in the two single sums, i.e. $\mathrm{E}\left[\Gamma_{p,q}\right] = \varsigma\Gamma_{ms}$, whereas the expectation in the double summation is

$$\mathrm{E}\left[\Gamma_n\Gamma_m^*\right] = \left(\varsigma\Gamma_{ms}\right)^2 + \delta_m^n\left(1-\varsigma\right)^2\Gamma_{md}^2\ . \tag{4.21}$$

The independent and fully correlated cases can be recovered by allowing ς to be zero or one, respectively.

Intermediate values of ς exhibit some similarities to the independent formulation. Figure 4.7 shows the relationship between the eigenvalues of $\overline{\mathbf{R}}_M$ for different values of Γ_{md} and Γ_{ms}. The traces in the figure are the median eigenvalues across 1000 realizations for each value of ς. The three minor eigenvalues are dependent on ς and Γ_{md} only, with Γ_{ms} having no effect. The difference in these minor eigenvalues drops by 6 dB when Γ_{md} is cut in half, and they decrease at a rate of 10 dB per decade with $1-\varsigma$. Following this trend, the largest minor eigenvalue for $\Gamma_{md} = 1$ will be equal to the noise power when $\varsigma = 0.997$. This value corresponds to an initial jammer to noise ratio of 60 dB. For jammers with lower power relative to the noise power, the minor eigenvalues will fall below the noise floor for a smaller value of ς.

The major eigenvalue is affected by both Γ_{md} and Γ_{ms}. As ς approaches 0 the value of Γ_{md} has a greater effect, as can be seen by comparing Fig. 4.7a with Fig. 4.7g. The right-hand side of these figures approaches the independent case, or fully diffuse reflection, and a lower diffuse reflection coefficient results in less overall power at the CRPA. The left-hand side of the plot represents more specular reflection, and so the effect of Γ_{ms} is more pronounced, as can be seen by comparing Figs. 4.7a, 4.7b, and 4.7c. Similarly, decreasing

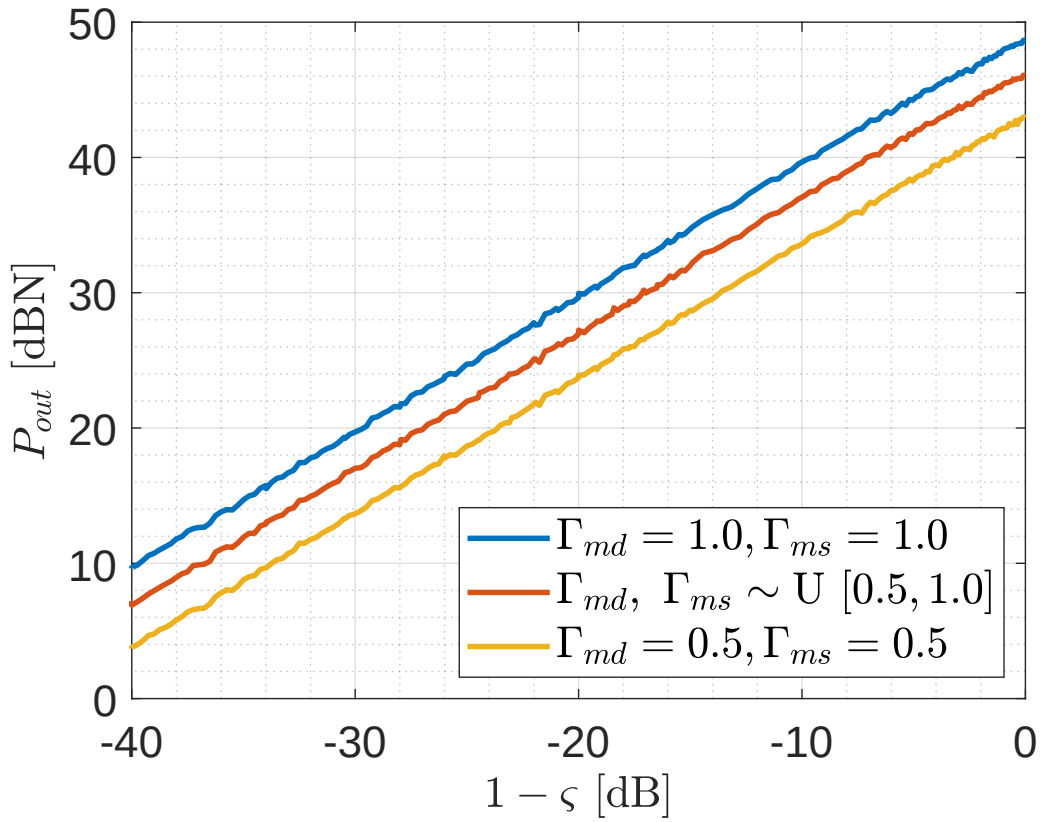

Figure 4.8: Median output power after nulling for different values of the specular reflection factor, ς.

the specular reflection coefficient reduces the coherent sum in the dependent case, and so the major eigenvalue converges to a value reduced in proportion to Γ_{ms}.

Recording the output power for these cases gives a similar result. Figure 4.8 shows the median output power, $\mathbf{w}^{\dagger}\mathbf{R}_M\mathbf{w}$, as a function of ς. The same 10 dB per decade relationship appears here, and for the blue trace, output power will be equal to the noise power at $1-\varsigma = -50$ dB or $\varsigma = 0.997$. The intersection with the $P_{out} = 0$ dBN axis occurs more quickly for smaller values of Γ_{md}, such as depicted by the yellow trace of Fig. 4.8.

The analysis in Fig. 4.7 assumes that each scatterer has the same values of Γ_{md} and Γ_{ms}. A more likely scenario is that the scatterer reflection coefficients are randomly distributed in some range. Letting $\Gamma_{md}, \Gamma_{ms} \sim \mathrm{U}\,[0.5, 1.0]$ and varying ς yields the red trace in Fig. 4.8. Here the red and yellow traces are 2.5 dB and 6 dB below the blue trace, which correspond to a factor of 0.75, the expected value of Γ_{ms}, and 0.5 respectively. Here the yellow trace

is 6 dB below the blue trace, corresponding to a factor of 0.5 which matches the values of Γ_{ms} and Γ_{md}. The red trace is 2.5 dB below the blue, which matches the expected values, $\mathrm{E}\left[\Gamma_{ms}\right] = \mathrm{E}\left[\Gamma_{md}\right] = 0.75$.

A similar analysis can be carried out for two independent jammer in a multipath environment. If a single jammer can be mitigated provided there is a large enough correlation with its reflected components, it stands to reason that two can as well. Figure 4.9 shows the eigenvalues for multipath environments with two jammers. As in Fig. 4.7, each realization comprises $M = 10$ randomly placed scatterers, and the CRPA receives two statistically independent line-of-sight components as well as two statistically independent groups of scattered fields. Scattered fields do have statistical dependence with other fields within the same group, as well as with the jammer which originated them, and that dependence is controlled again with ς.

In the two jammer case, $\overline{\mathbf{R}}_M$ has two major eigenvalues and two minor. The major eigenvalues are not equal in magnitude, because the two jammers, though linearly independent, are not orthogonal. Additionally, the minor eigenvalues are 6 dB greater than in Fig. 4.7, due to there being twice as many scattered fields present at the CRPA. The magnitude of the largest eigenvalue has also increased, though not by 6 dB. Again, this is due to some overlap between the eigenvectors of the two jammers, and a 6 dB increase would only be expected if the jammers were, in fact, fully correlated.

Considering both the one jammer and two jammer cases, a direct relationship between the minor eigenvalues ς has been shown, as well as with the overall output power. The 10 dB per decade drop occurs because multipath components arising from specular reflection add in phase, and are mitigated by a CRPA with any number of elements. The coherent jammer power is proportional to the specular reflection factor, and as ς approaches 1, the jammer power mitigated by the CRPA approaches the total power.

4.4 Time Domain Scattering

The phase variations and statistical independence in multipath environments is due to the relative motion of scattering objects. Fields scattered from a moving object exhibit

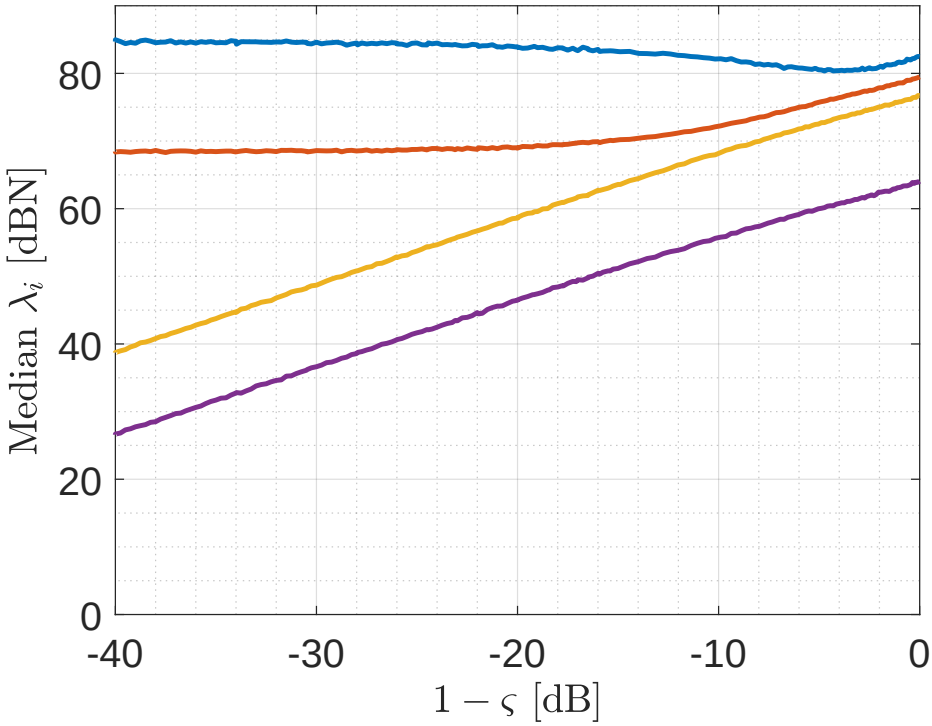

(a) $\Gamma_{md} = 1$, $\Gamma_{ms} = 1$.

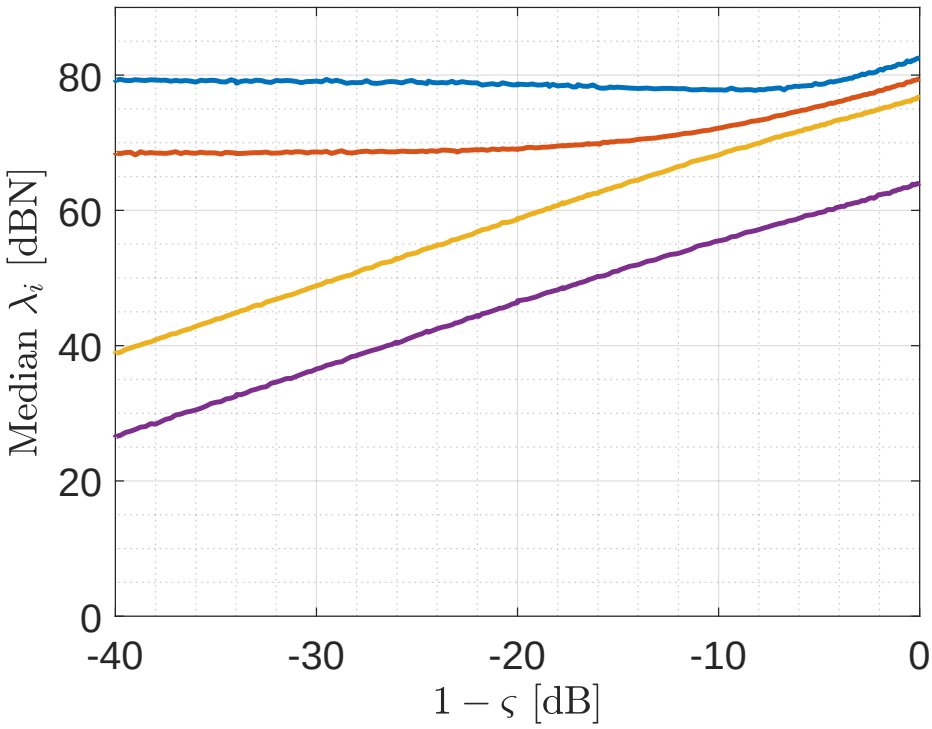

(b) $\Gamma_{md} = 1$, $\Gamma_{ms} = \frac{1}{2}$.

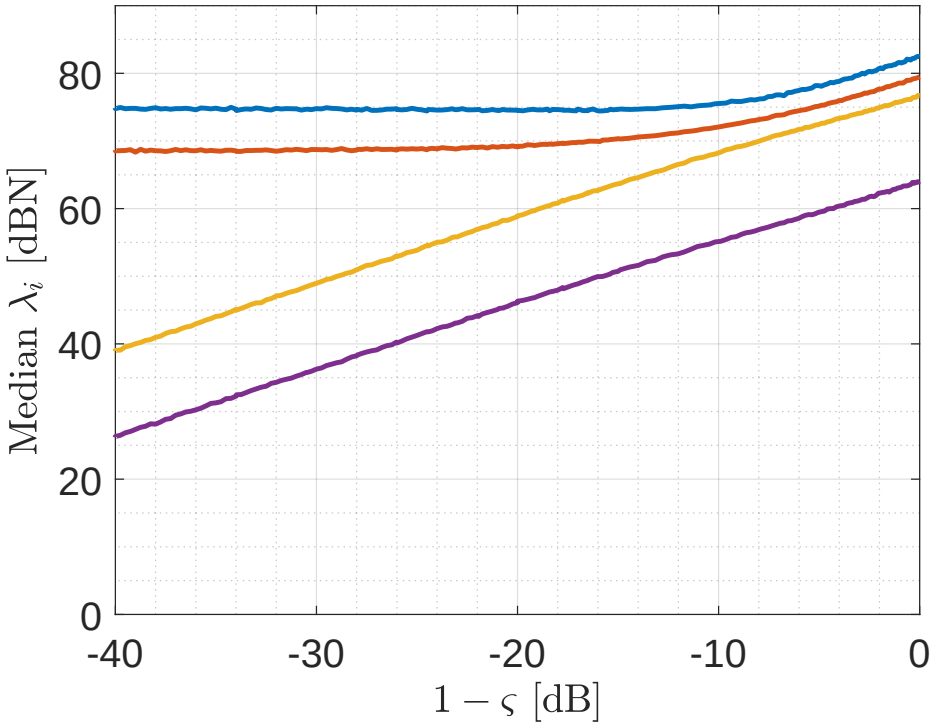

(c) $\Gamma_{md} = 1$, $\Gamma_{ms} = \frac{1}{4}$.

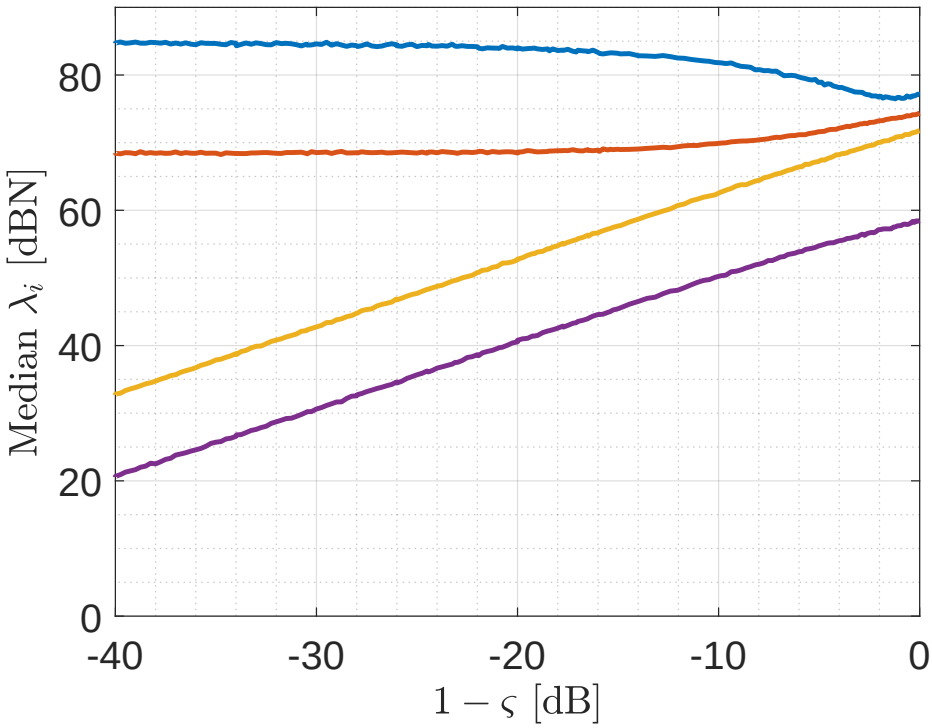

(d) $\Gamma_{md} = \frac{1}{2}$, $\Gamma_{ms} = 1$.

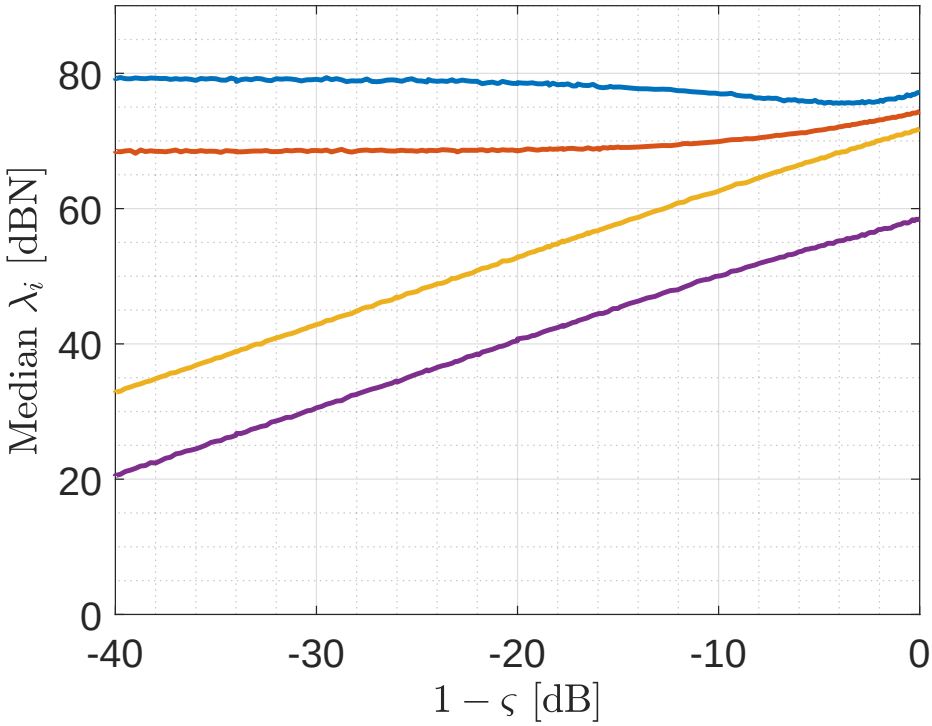

(e) $\Gamma_{md} = \frac{1}{2}$, $\Gamma_{ms} = \frac{1}{2}$.

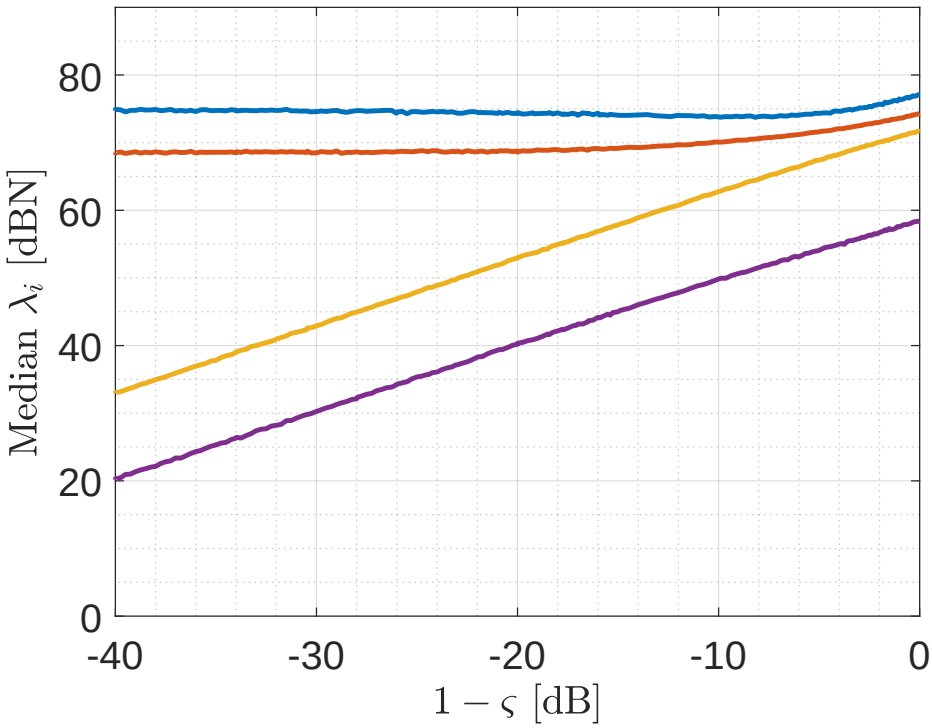

(f) $\Gamma_{md} = \frac{1}{2}$, $\Gamma_{ms} = \frac{1}{4}$.

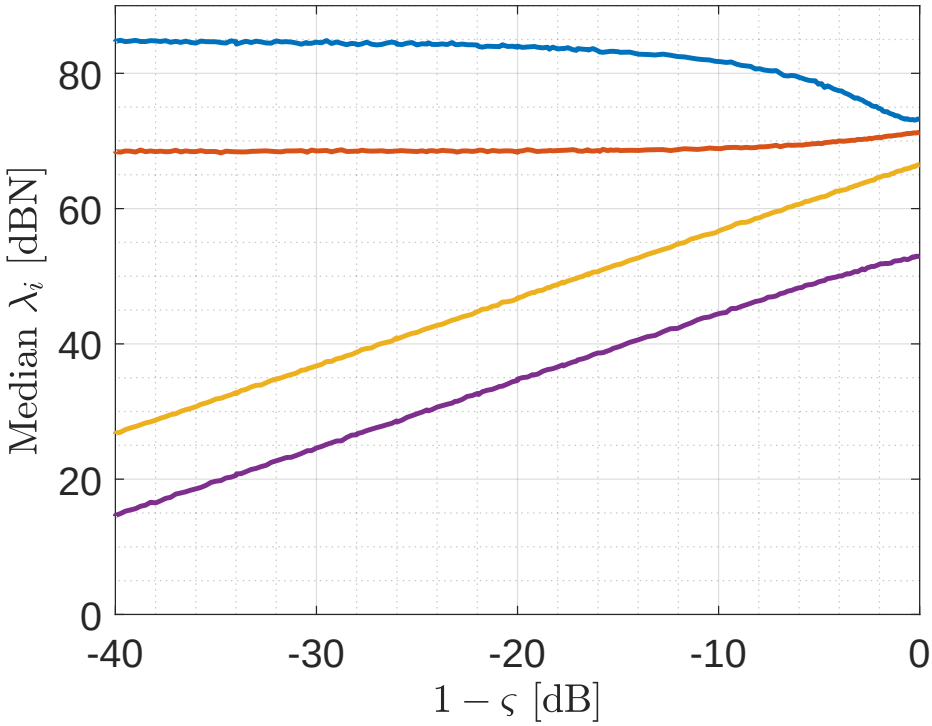

(g) $\Gamma_{md} = \frac{1}{4}$, $\Gamma_{ms} = 1$.

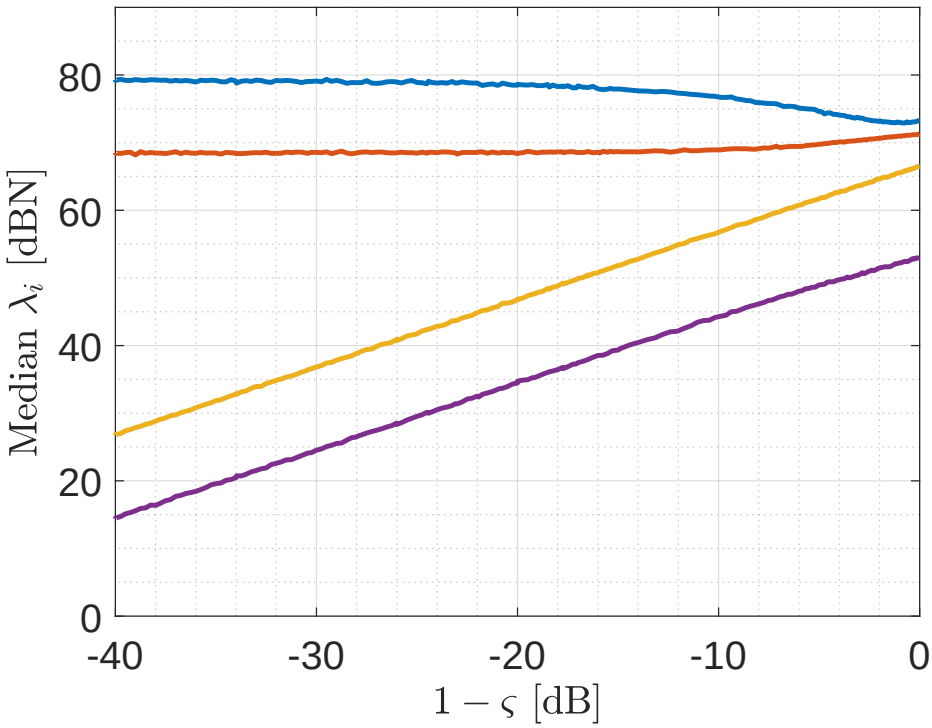

(h) $\Gamma_{md} = \frac{1}{4}$, $\Gamma_{ms} = \frac{1}{2}$.

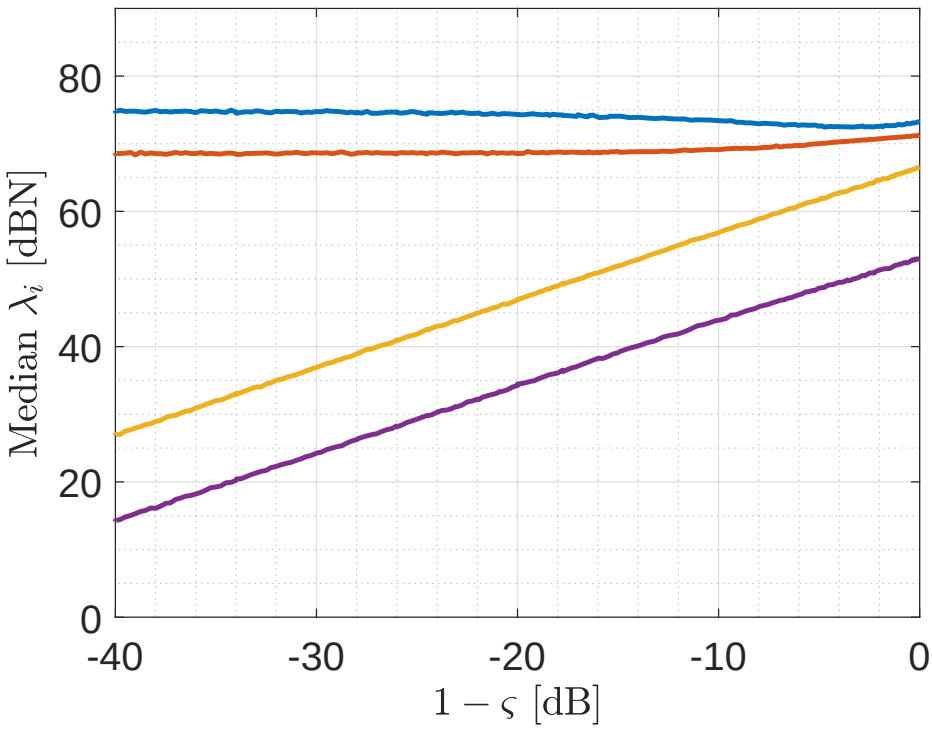

(i) $\Gamma_{md} = \frac{1}{4}$, $\Gamma_{ms} = \frac{1}{4}$.

Figure 4.9: Eigenvalues of $\overline{\mathbf{R}}_M$ for varying values of Γ_{md} and Γ_{ms}, two jammer case.

a Doppler shift, resulting in time varying phase differences at the receiver. Incorporating motion into a deterministic scattering environment by associating random velocity vectors to scattering objects can give rise to time varying phase differences, which may prevent an iterative CRPA from canceling interference.

The scattered fields at the CRPA for a single jammer and $M = 10$ scatterers are computed as a function of time by

$$\boldsymbol{\mathcal{E}}_{s,i}^{inc} = \mathrm{Re}\left\{ e^{j(\omega t - \psi_i(t))} \left(E_{\theta,i} \begin{bmatrix} \cos\theta_{s,i}(t)\cos\phi_{s,i}(t) \\ \cos\theta_{s,i}(t)\sin\phi_{s,i}(t) \\ \sin\theta_{s,i}(t) \end{bmatrix} + E_{\phi,i} \begin{bmatrix} -\sin\phi_{s,i}(t) \\ \cos\phi_{s,i}(t) \\ 0 \end{bmatrix} \right) \right\}, \tag{4.22}$$

where the phase $\psi_i(t)$ is a function of the velocity vector $\boldsymbol{\nu}_i$,

$$\psi_i(t) = \mathrm{k}_0 \begin{bmatrix} (x_c - \nu_{x,i}t)\sin\theta_{s,i}(t)\cos\phi_{s,i}(t) \\ +(y_c - \nu_{y,i}t)\sin\theta_{s,i}(t)\sin\phi_{s,i}(t) \\ +(z_c - \nu_{z,i}t)\cos\theta_{s,i}(t) \end{bmatrix}. \tag{4.23}$$

The dot product of the incident field is taken with the vector effective height $\mathbf{h}\left(\theta_{s,i}(t), \phi_{s,i}(t)\right)$, which also varies with time due to the changing angles-of-arrival for the scatterers. The load voltages are found for a matched condition, and are summed for the total load voltage present at each of the n CRPA ports,

$$\left[\mathbf{v}_t^L\right]_n = \left[\mathbf{v}_j^L\right]_n + \sum_{i=1}^{M} \left[\mathbf{v}_{s,i}^L\right]_n = |v_t^L|_n \,\mathrm{Re}\{e^{j(\omega t + \beta_n)}\}. \tag{4.24}$$

The in-phase and quadrature components are then computed,

$$\left[\mathbf{x}_I\right]_n = |v_t^L|_n \cos\left(2\pi f_{IF} t + \beta_n\right),$$

$$\left[\mathbf{x}_Q\right]_n = -|v_t^L|_n \sin\left(2\pi f_{IF} t + \beta_n\right), \tag{4.25}$$

where $f_{IF} = 30$ MHz is the intermediate frequency. The in-phase and quadrature vectors are then input into the iterative algorithm (2.28).

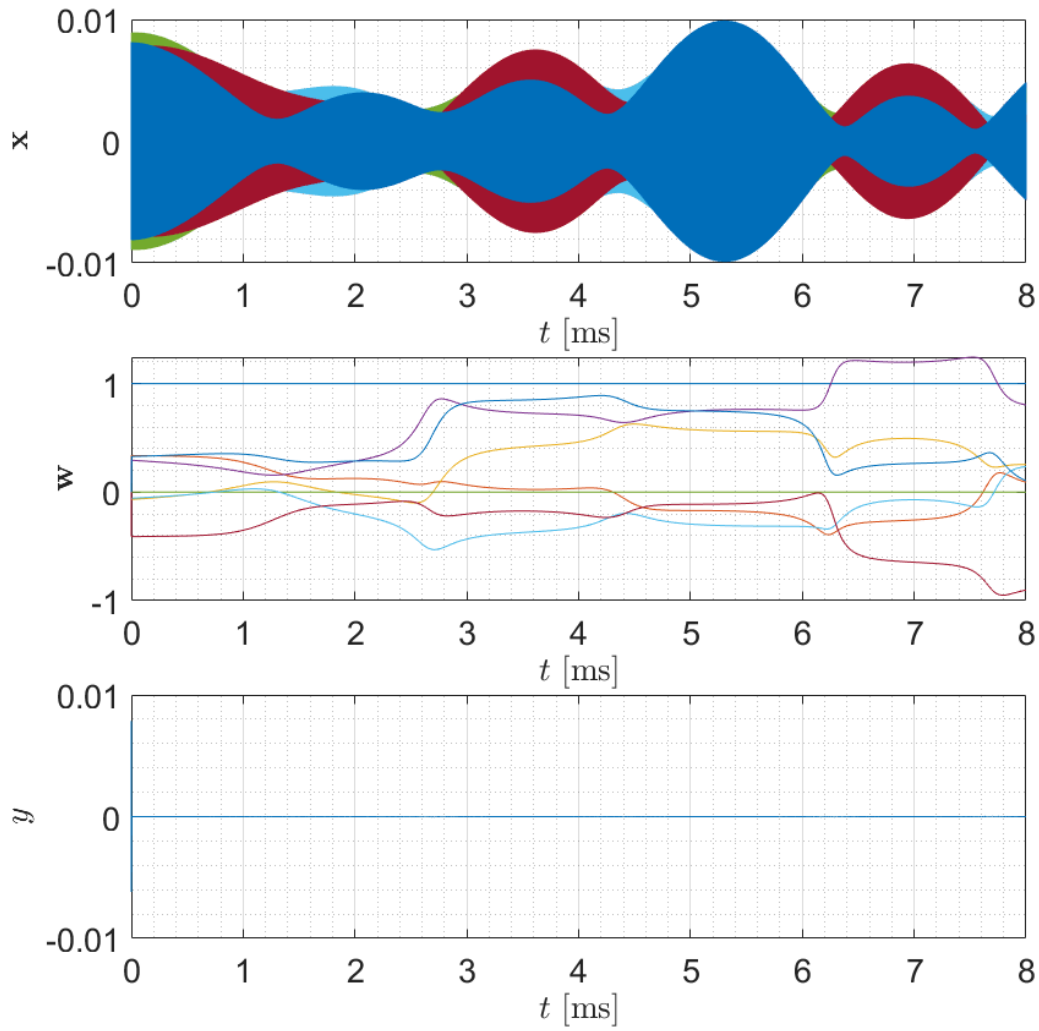

Figure 4.10: Input, weights, and output for time domain moving scatterer realization.

Figure 4.10 shows the results of applying Frost's Algorithm to the input vectors (4.25) for $M = 10$ scatterers moving with randomly oriented velocity vectors with a variance of 50 mph. The jammer is, again, an omni-directional dipole operating at 10 W and located 1 km from the CRPA. Scatterers are located within elevations $\pm 5°$ relative to the receiver and within a 1 km radius. The fading of the input channels is slow relative to the algorithm, which updates at 125 MHz, and so the output, y, is reduced regardless of the fading. The weights continue to change over the entire time span, never converging to one value. In this case, $\mathbf{R}$ is non-stationary, and the optimal weights change with time. Over short

periods of time the scattered fields are correlated with the jammer, though the correlation coefficient changes with time. Despite a small number of CRPA elements, a single jammer in a multipath environment does not severely impact CRPA operation provided there is some correlation between the scattered fields.

The success of the iterative techniques will necessarily depend on the algorithm update rate and the rate of variation for the respective phases. Different center frequencies, velocity vectors, and update rates will yield a different overall performance for any distinct case. However, for the numbers used here, it is realistic that the application of Frost's Algorithm to a GPS CRPA with scatterers moving at typical vehicle velocities can successfully mitigate interference in a multipath environment.

4.5 Discussion

This chapter has presented a mixed scattering model parameterized by the specular reflection factor, ς. Mixed scattering is modeled as a combination of specular and diffuse scattering giving rise to statistically dependent and independent multipath components, respectively.

As ς approaches one, the scattered components all add in phase at the CRPA, and total cancellation is possible. This has been shown to be the case given the structure of the partial covariance matrix under the dependence assumption. After removing the portion of $\mathbf{R}$ due to Gaussian noise, $\overline{\mathbf{R}}$ is always rank one and a null-steering solution is always possible, even if a visible null is not.

At the other extreme, when ς approaches zero, all the scattering is modeled to be diffuse and the multipath components, being independent, require one degree of freedom per incident wave. Under this condition no solution is possible.

A time-domain scenario has also been presented to predict how a CRPA may behave in the real world. The relative motion of different objects and the associated Doppler shifts introduce random phases between different multipath components. If these phases vary rapidly enough, the real-time CRPA implementation behaves like the independent formulation. However, if the phases vary slowly enough relative to the algorithm update

rate, the electromagnetic environment is dependent over sufficiently long stretches of time to find a stable set of weights. This can be realized at the assumed vehicular speeds using clock rates that are achievable with modern hardware.

Jammer power in this chapter has been assumed to be high relative to the noise power. This highlights the structure of the covariance matrix well, and emphasizes differences between dependent and independent cases. Additionally, the maximum reflection coefficient for diffuse scattering ranges from 0.5 to 1.0. It is likely that much of the energy reflected from a diffuse surface will be directed to angles away from the CRPA, and a smaller value may be more appropriate. If jammer power is lower and a small fraction of that power is reflected towards the CRPA, GPS interruption is not a foregone conclusion. The given environment and jammer charachteristics will ultimately determine whether a CRPA design is adequate in protecting PNT services for the user. What has been presented here is intended as a framework for considering physical channel models to SWAP constrained systems.

Determination of appropriate values for Γ_{md}, Γ_{ms}, and ς require extensive measurements in a variety of environments. No doubt some general characteristics will arise, such as similarities in Γ_{md} or Γ_{ms} on the type of terrain or dependence of ς on the user's velocity. However, these are only speculations at this point, as a comprehensive measurement campaign is beyond the scope of this work.

CHAPTER 5

POLARIZATION AND STAP CONSIDERATIONS

In this chapter, correlated and independent jamming is investigated using a generalized scattering matrix, $\mathbf{\Gamma}$, which includes scattering effects on the polarization of the propagating waves. Techniques for generating realizations of $\mathbf{\Gamma}$ are described and applied to correlated and independent jamming environments. Under these assumptions, a comparison of dual-linear and RHCP CRPAs is presented.

Additionally, STAP techniques are discussed. Both narrowband and wideband scenarios are presented, with two potential null-steering constraint vectors applied to each. The wideband mitigation possible with STAP makes it the best candidate for man-portable CRPA realizations.

5.1 Polarization

In order to compare CRPA operation when polarization degrees of freedom are included, two four-element planar CRPA models were generated using FEKO: one with dual linear elements, and one with RHCP elements. Both were subjected to the same multipath environments and satellite coverage for each was logged.

The multipath environments now considered comprise a single jammer and $M = 10$ scatterers. These are formed in the same manner as described in Chapter 4, however, polarization of the jammer and reflected components may now differ from one another, and are dictated by a generalized reflection matrix, $\mathbf{\Gamma}$ of (4.6). Three relevant matrix operations

are used to define $\mathbf{\Gamma}$, these being rotation, reflection, and shear. First, consider the rotation

$$\begin{bmatrix} E_\theta \\ E_\phi \end{bmatrix} = \boldsymbol{P} \begin{bmatrix} E_{\theta'} \\ E_{\phi'} \end{bmatrix} = \begin{bmatrix} \cos\rho & -\sin\rho \\ \sin\rho & \cos\rho \end{bmatrix} \begin{bmatrix} E_{\theta'} \\ E_{\phi'} \end{bmatrix}, \tag{5.1}$$

which does not change axial ratio or the sense of rotation, but merely rotates the locus of the electric field by some angle ρ. Next reflection about a line defined by its normal vector, $\hat{\mathbf{l}} = [l_\theta \; l_\phi]^T$, is given by

$$\begin{bmatrix} E_\theta \\ E_\phi \end{bmatrix} = \boldsymbol{\Lambda} \begin{bmatrix} E_{\theta'} \\ E_{\phi'} \end{bmatrix} \begin{bmatrix} l_\theta^2 - l_\phi^2 & 2l_\theta l_\phi \\ 2l_\theta l_\phi & l_\phi^2 - l_\theta^2 \end{bmatrix} \begin{bmatrix} E_{\theta'} \\ E_{\phi'} \end{bmatrix}. \tag{5.2}$$

This transform does change the sense of rotation, i.e. a right-handed circular or elliptical wave subject to (5.2) becomes left-handed. Finally, a shear transform is defined as one of the following,

$$\begin{bmatrix} E_\theta \\ E_\phi \end{bmatrix} = \boldsymbol{K}_\phi \begin{bmatrix} E_{\theta'} \\ E_{\phi'} \end{bmatrix} = \begin{bmatrix} 1 & \kappa \\ 0 & 1 \end{bmatrix} \begin{bmatrix} E_{\theta'} \\ E_{\phi'} \end{bmatrix},$$

$$\begin{bmatrix} E_\theta \\ E_\phi \end{bmatrix} = \boldsymbol{K}_\theta \begin{bmatrix} E_{\theta'} \\ E_{\phi'} \end{bmatrix} = \begin{bmatrix} 1 & 0 \\ \kappa & 1 \end{bmatrix} \begin{bmatrix} E_{\theta'} \\ E_{\phi'} \end{bmatrix}. \tag{5.3}$$

Note that this transform will increase $\|\mathbf{E}\|$, and so does not represent any physical scattering process. To address this, $\boldsymbol{K}$ must divided by $1 + \kappa$. Now, $\boldsymbol{K}$ has the effect of rotating LP fields, or changing the axial ratio of circularly and elliptically polarized waves.

Of the three matrices defined above, only $\boldsymbol{K}$ is capable of changing the reflected power. However, it is rare that all of the incident power will be reflected from a scatterer. Some portion may be transfered through the scattering oject, and the reflected waves may not all be oriented in the same direction. To account for this decrease in power, a scalar reflection coefficient Γ is included, giving the reflection matrix the form

$$\mathbf{\Gamma} = \Gamma \boldsymbol{P} \boldsymbol{\Lambda} \boldsymbol{K}. \tag{5.4}$$

The scalar coefficient can be strictly real or a complex number provided that $\|\Gamma\| \leq 1$.

For the purpose of the Monte Carlo simulations which follow, each scattering object is assumed to have a unique scattering matrix, $\mathbf{\Gamma}_i$. The three transforms can be defined for each scatterer by the following random parameters. Rotation of the ith scattered field is set by $\rho_i \sim \mathrm{U}\left[0, 2\pi\right]$. Similarly for $\boldsymbol{K}$, let $\kappa_i \sim \mathrm{U}\left[0, 1\right]$. Finally, the matrix $\mathbf{\Lambda}$ is parameterized by a line of reflection in the $\theta - \phi$ plane. This is accomplished letting $\beta \sim \mathrm{U}\left[0, 2\pi\right]$ and defining the line of reflection as

$$\mathbf{l} = \begin{bmatrix} \cos\beta \\ \sin\beta \end{bmatrix}. \tag{5.5}$$

A second consideration for $\mathbf{\Lambda}$ must also be made, namely whether or not the reflection takes place. When an RHCP incident electric field reflects off of a plane, the reflected fields are LHCP. However, enforcing a reflection matrix that flips the sense of rotation for every scattered component could artificially improve the predicted performance of a CRPA using RHCP elements, especially if multiple reflections take place over long distances. Of course, $\boldsymbol{K}$ will change the axial ratio of the scattered field, and the FEKO modeled CRPA elements do not have perfect axial ratios either, so despite polarization mismatch, some power from LHCP scattered fields is still present on the CRPA ports. However, the obvious choice is to let $\boldsymbol{\Lambda} = \mathbf{I}_{2\times 2}$ with probability $\frac{1}{2}$ and take the form of (5.2) the rest of the time. Similarly, K is defined to act on either the θ or ϕ component of $\mathbf{E}$, and it two will take either value with probability $\frac{1}{2}$. Finally, values of Γ are taken to be a uniformly distributed, $\Gamma_i \sim \mathrm{U}\left[0.5, 1.0\right]$.

An initial realization with $M = 1$ scatterer is shown in Fig. 5.1 for a CRPA with four RHCP elements. Both independent and fully correlated formulations are plotted with the jammer indicated by the black circle and the scatterer indicated by the brown circle. The scattering matrix, $\mathbf{\Gamma}$, was assumed to be the identity matrix in this case, so that the CRPA would be presented with two RHCP incident waves. Figure 5.1a shows a deep null in the direction of the jammer, however the scatterer seems offset from the scatter angle-of-arrival. This is due to the CRPA elements having higher gain in the direction towards the jammer than the scatterer. The scattered field suffers more path loss, and impinges on the CRPA from an angle near the horizon, where the reference pattern has lower gain. Figure 5.1b does not show good alignment between nulls and incidence angles, however this is to be

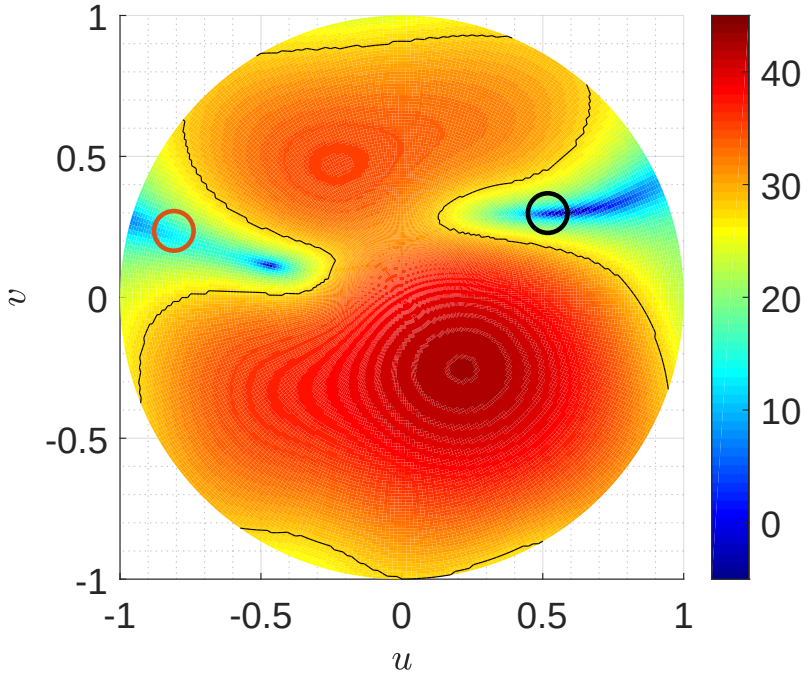

(a) Independent scattering, coverage = 81.1%.

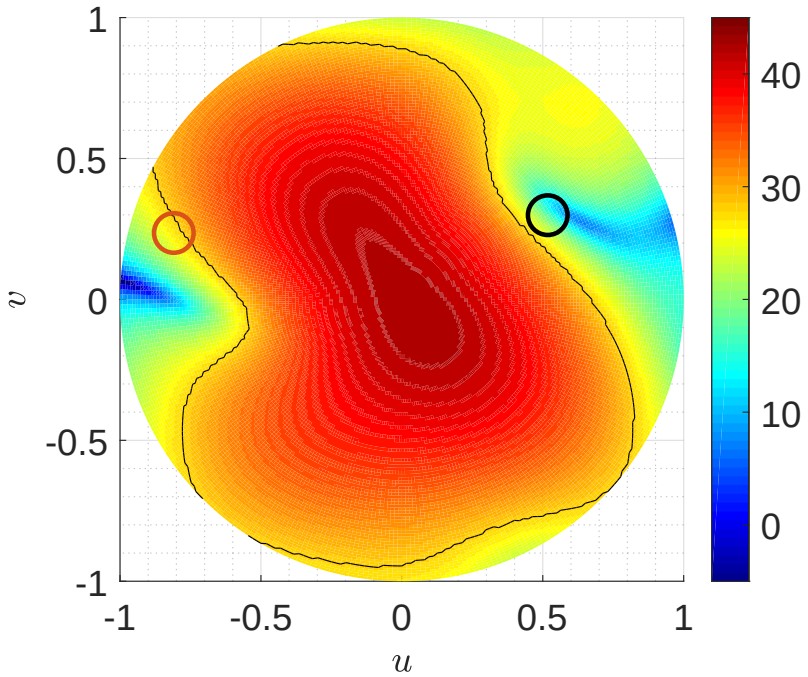

(b) Dependent scattering, coverage = 72.4%.

Figure 5.1: Coverage maps (C_s/N_0) for single scatterer and RHCP array, $\mathbf{\Gamma} = \mathbf{I}_{2\times 2}$.

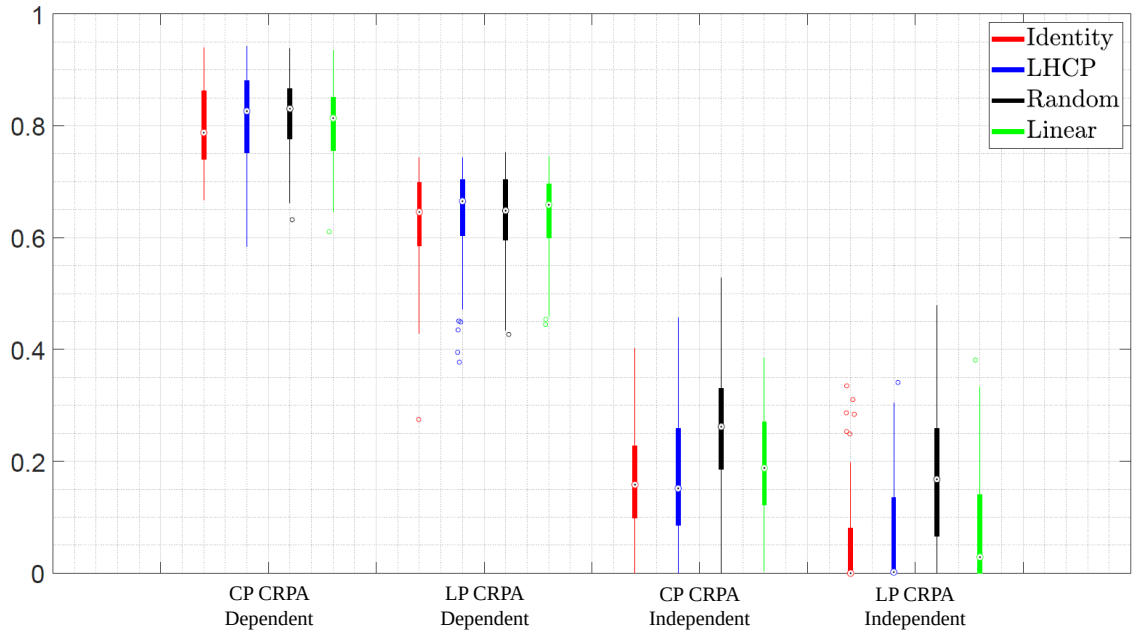

Figure 5.2: CRPA coverage under independent and dependent scattering assumptions for different scattering matrix models.

expected. Recall that in Fig. 4.1, the dependent formulation did not generate any visible nulls, though cancellation did occur as shown by the drop in output power.

A comparison of satellite coverage for different CRPA configurations and scattering assumptions is shown in Fig. 5.2. The scattering matrix was assumed to take on four different values, an identity matrix, an LHCP matrix where the ϕ component is negated to produce LHCP scattered fields, the random $\mathbf{\Gamma}$ described above, and finally the $\mathbf{\Gamma}$ of (4.9), denoted LP in Fig. 5.2. Also, because the random $\mathbf{\Gamma}$ is scaled by $\Gamma \sim \mathrm{U}\left[0.5, 1.0\right]$ for each scatterer, the rest of the matrices are scaled by $\mathrm{E}\left[\Gamma\right] = 0.75$ to prevent overly optimistic predictions for the random $\mathbf{\Gamma}$ compared to the other forms. Independent and fully correlated scattering was assumed for each case. The jammer and scatterers are located near the horizon at elevation angles not exceeding 15°, and positions of each are determined randomly.

Unsurprisingly, the dependent cases result in higher coverage than the dependent cases. Also, for the dependent cases, the form $\mathbf{\Gamma}$ takes makes nearly no difference on coverage. The independent cases have more variation, in particular, the random $\mathbf{\Gamma}$, which is the most realistic form for $\mathbf{\Gamma}$ to take results in the highest coverage.

In every case, the RHCP CRPA performs better than the dual-linear CRPA. Two dual-linear elements lack the degrees of freedom to cancel multiple CP or EP jammers, and the additional degrees of freedom that worked well for strictly LP jammers are not sufficient.

This section has shown how polarization can be incorporated into a multipath jamming environment. It is also possible to consider mixed scattering conditions similar to those in Chapter 4 by one of two choices in formation of $\boldsymbol{\Gamma}$. The first would be to allow the scalar Γ be replaced by mixed reflection coefficient of (4.17), whereas the second option would be to define separate diffuse and specular scattering matrices, and vary the proportion of each present with ς, i.e.

$$\boldsymbol{\Gamma} = \varsigma\Gamma_s\boldsymbol{P}_s\boldsymbol{\Lambda}_s\boldsymbol{K}_s + (1-\varsigma)\Gamma_d\boldsymbol{P}_d\boldsymbol{\Lambda}_d\boldsymbol{K}_d. \tag{5.6}$$

The second of these two options would, no doubt, be a more accurate model of a physical environment, however, obtaining realistic values for all the parameters would require a significant measurement campaign. This analysis has been neglected here, as the limit cases are considered. Under fully correlated scattering, CRPA performance decreases compared to the line of sight case, though not to a complete loss of coverage. Independent scattering is much more detrimental, but when scattering objects are close to the horizon, even this does not guarantee a total loss of GPS service in all cases. The actual theater of operation for a man-portable CRPA will fall somewhere between, and parameterizing this fully under the mixed scattering model presented in this work requires field measurements to acquire realistic values of ς.

5.2 Space-Time Adaptive Processing Analysis

The limitations imposed on a man-portable CRPA design decrease the spatial degrees of freedom that may be feasible. Two possible candidates for improving performance and increasing the number of jammers which may be mitigated are dual-linear elements and STAP. In the previous section it has been shown that, though dual-linear elements do show some promise in simulation when the total number of ports is doubled, if the number of ports remains the same the performance is highly degraded.

Doubling the number of channels increases the SWAP requirements of the CRPA in

a substantial way. The following discussion on STAP highlights the benefits of adding time-domain degrees of freedom in the digital domain.

5.2.1 Narrow Band Jammers

STAP processing uses multiple time samples of the input vector, $\mathbf{x}$, to introduce additional time-domain degrees off freedom for null-steering. With an additional p tapped delay lines, $\mathbf{x}$ becomes

$$\mathbf{x}^{STAP} = \begin{bmatrix} \mathbf{x}(k) \\ \mathbf{x}(k-1) \\ \vdots \\ \mathbf{x}(k-p) \end{bmatrix}. \tag{5.7}$$

For Frost's algorithm, (2.28) does not need to be adjusted, only the dimensions of the vectors and the constraints. Possible constraints for STAP processing are similar to the constraints discussed in Section 2.1, however care must now be taken to define the additional vector elements. Consider first the Capon steering vector, $\boldsymbol{\psi}$, as defined in (2.4). To implement STAP processing in a particular direction, and at a particular frequency, phase shifted copies of $\boldsymbol{\psi}$ are concatenated together to form a $pN \times 1$ vector

$$\boldsymbol{\psi}^{STAP} = \begin{bmatrix} \boldsymbol{\psi} \\ \boldsymbol{\psi} e^{-j\Delta} \\ \vdots \\ \boldsymbol{\psi} e^{-jp\Delta} \end{bmatrix}, \tag{5.8}$$

where $\Delta = 2\pi f_{IF} T_s$.

Because STAP allows for more degrees of freedom than space-only null-steering, some may be deployed to constrain the weights to steer towards more than one direction. If the steering vectors, $\boldsymbol{\psi}_i$, to the GPS SVs are known, and there are sufficient taps to balance the

degrees of freedom for jammers and SVs, the constraint matrix may be defined as

$$\mathbf{C} = \begin{bmatrix} \boldsymbol{\psi}_1^\dagger & \boldsymbol{\psi}_1^\dagger e^{-j\Delta} & \cdots & \boldsymbol{\psi}_1^\dagger e^{-jp\Delta} \\ \boldsymbol{\psi}_2^\dagger & \boldsymbol{\psi}_2^\dagger e^{-j\Delta} & \cdots & \boldsymbol{\psi}_2^\dagger e^{-jp\Delta} \\ \vdots & \vdots & \ddots & \vdots \\ \boldsymbol{\psi}_q^\dagger & \boldsymbol{\psi}_q^\dagger e^{-j\Delta} & \cdots & \boldsymbol{\psi}_q^\dagger e^{-jp\Delta} \end{bmatrix}, \tag{5.9}$$

for p taps and q SVs. This is the constraint matrix in (2.24). This set of constraints will offer the best performance, however it requires feedback from the GPS receiver to estimate $\boldsymbol{\psi}_i$ and is ill suited to the modular man-portable SWAP constrained CRPA considered in this work.

For STAP processing, two forms of blind null-steering suggest themselves for STAP. First consider

$$\mathbf{e}_4 = [1\ 0\ 0\ 0\ 0\ \cdots\ 0]^T, \tag{5.10}$$

which is a familiar constraint vector with additional zeros concatenated at the end. This will enforce the condition that a single reference element will remain on. However, the vector

$$\mathbf{e}_5 = \frac{1}{\sqrt{p-1}} \left[1\ 0\ 0\ 0\ e^{j\Delta}\ 0\ 0\ 0\ e^{j2\Delta}\ 0\ 0\ 0\ \cdots\right]^\dagger, \tag{5.11}$$

similarly enforces the condition that a single reference element remains on, but with multiple time samples added in phase at a particular frequency determined by Δ. When chosen correctly, $\mathbf{e}_5$ adds GPS signals coherently, increasing C_s/N_0.

Both $\mathbf{e}_4$ and $\mathbf{e}_5$ result in similar beam patterns when null-steering in the presence of CW jammers. Figure 5.3 shows a single realization of the reception patterns for representative null-steering realizations using $\mathbf{e}_4$ and $\mathbf{e}_5$ in the presence of a narrow band jammer. The two patterns are identical, except for a 11.9 dB uniform difference. This experiment when repeated for 1000 realizations yielded this result in each case. There is a uniform increase in signal power due to the coherent sum of adjacent time samples, but the overall pattern in otherwise unchanged at the frequency of interest.

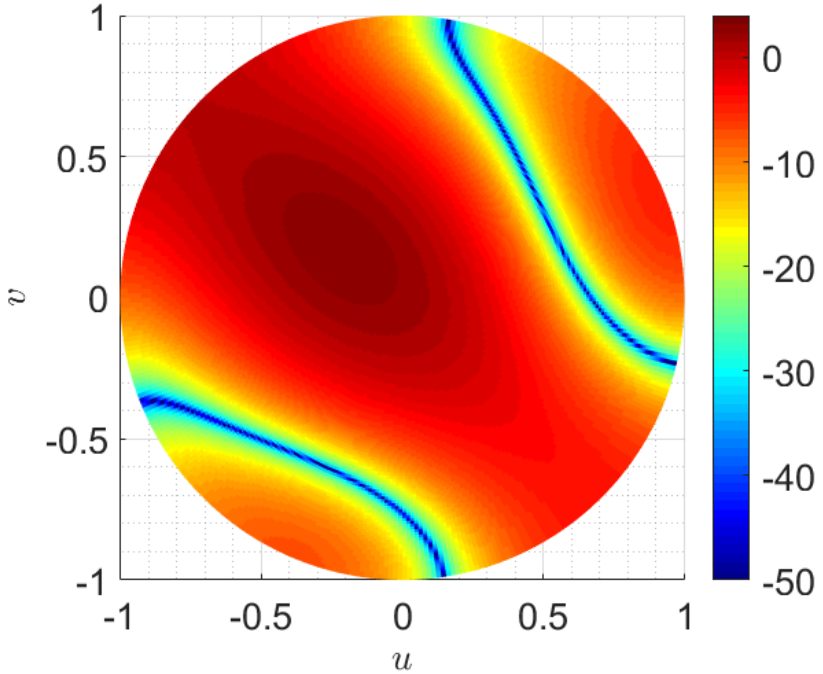

(a) Reception pattern using $\mathbf{e}_4$.

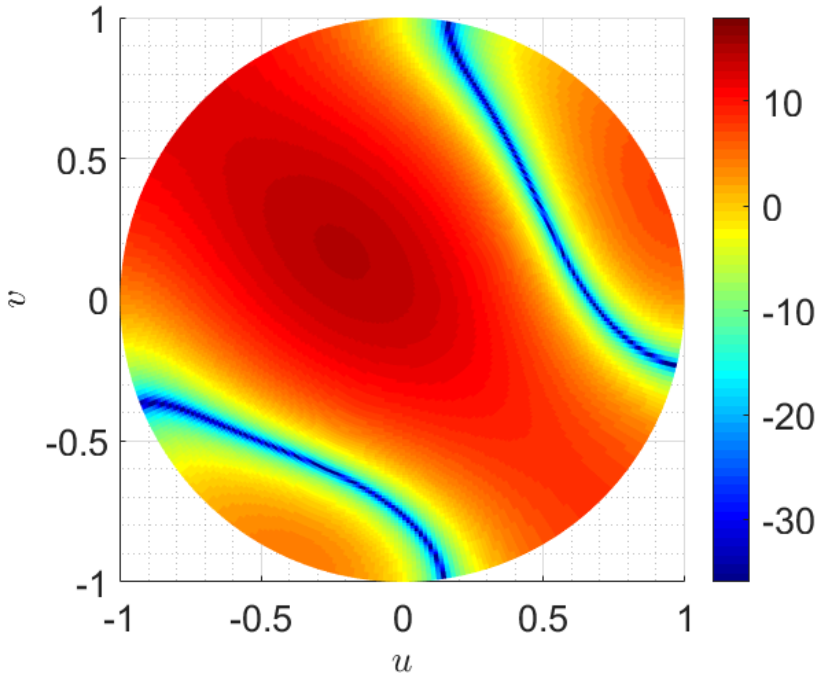

(b) Reception pattern using $\mathbf{e}_5$.

Figure 5.3: Comparison of constraint vectors for use in STAP.

5.2.2 Wide Band Jammers

Synthesis of wideband jammers can take many forms, however the type of wideband jammer that is most difficult to cancel is Band-limited Gaussian noise (BLGN). This wide band noise, which overlaps the GPS spectrum and originates from a jammer, can be reduced using STAP techniques, provided it originates from some direction. Conventional, single-sample null-steering fails for this type of jammer, as does polarization diversity, however STAP is able to mitigate it by producing a wide band null in the reception pattern for multiple frequencies. To demonstrate this, the constraint vectors, $\mathbf{e}_4$ and $\mathbf{e}_5$ are applied to traces of synthesized time domain data representing a BLGN jammer. Gaussian noise traces are generated in MATLAB and fed into a bandpass filter matched to the GPS L1 spectrum, i.e. 1.57542 $\pm$ 10.23 MHz, to match the L1 P(Y) code. The band-limited traces are then offset in time depending on the angles-of-arrive of the jammer, corresponding to the differences in times-of-arrival of the plane wave at each element, resulting in the $N \times 1$ jammer vector, $\mathbf{x}_j(t)$. Additionally, AWGN is added to account for the antenna brightness temperature and thermal noise in the electronics. This is the same noise referenced in earlier results, and is uncorrelated across elements. The CRPA front end is assumed to have an initial filtering stage for image rejection, and so $\mathbf{x}_j(t)$ and $\mathbf{x}_N(t)$ are filtered by a COTS filter. The spectra of each component, the jammer and the noise, are shown in Fig. 5.4 after this first filtering stage. The next stage is downconversion, whereby the RF signals are brought down in frequency to an intermediate frequency, f_{IF}. This is accomplished by mixing the input vectors with a sinusoidal local oscillator at frequency f_{LO},

$$\mathbf{x}'_{j,N}(t) = \mathbf{x}_{j,N}(t) cos(2\pi f_{LO} t), \tag{5.12}$$

creating copies at the sum and difference frequencies, $|f_c \pm f_{LO}|$. Another filtering stage must be used to eliminate the higher frequency component, leaving the downconverted received vector,

$$\mathbf{x}''_{j,N}(t) = h_{LPF}(t) * \mathbf{x}'_{j,N}(t), \tag{5.13}$$

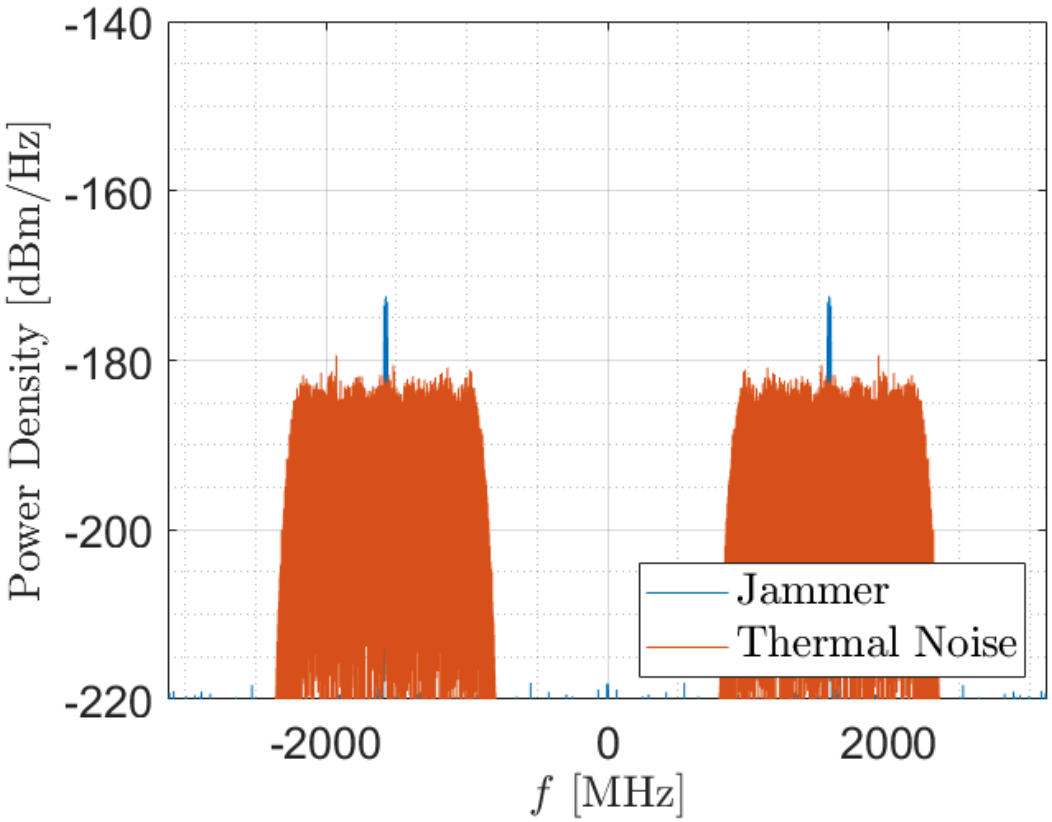

Figure 5.4: Spectral power densities of band-limited Gaussian noise jammer and additive white Gaussian noise present prior to image rejection.

where $*$ denotes convolution and h_{LPF} is the impulse response of the low-pass filter. The spectra following this filtering stage appear in Fig. 5.5. The next stage is the analog to digital converter (ADC) with sample period T_s, which is implemented in MATLAB by down sampling the input signal,

$$\mathbf{x}''_{j,N}(k) = \mathbf{x}''_{j,N}(k * T_s). \tag{5.14}$$

Following this stage, the in-phase and quadrature components must be separated. In the preceding chapter, these were computed with (4.25) from the RF components. This assumed IQ downconversion in hardware by mixing with a cosine and a sine, however, performing this step with digital filters reduces the hardware requirements of the system. The quadrature component of a signal is found using a Hilbert transformer with an ideal frequency response of

$$H(f) = -j\text{sgn}(f). \tag{5.15}$$

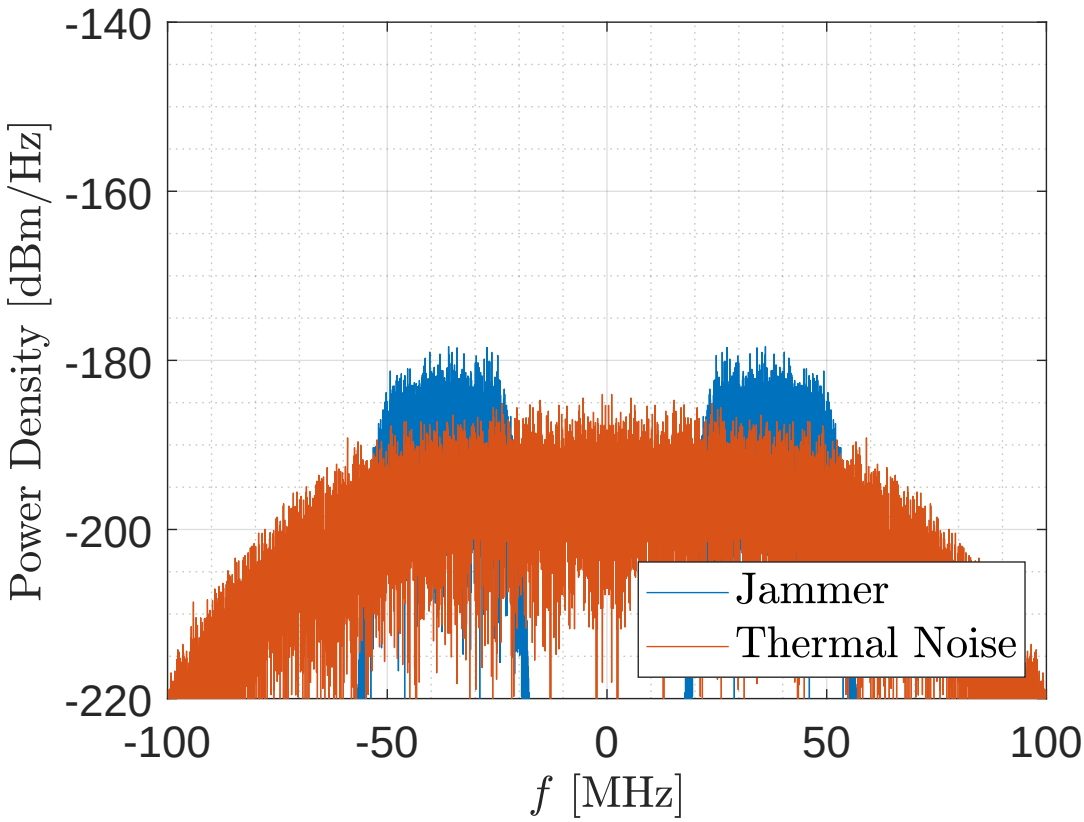

Figure 5.5: Spectral power densities of band-limited Gaussian noise jammer and additive white Gaussian noise present prior to downconversion.

This is approximated digitally using an FIR Hilbert filter, $h_H(t)$, however the response is not ideal, in that high and low frequency components are cut off, and ripple exists in the passband. To control for this, another FIR filter, $h_{bpf}(t)$ is constructed for the in-phase component, which is designed to have the same passband as $h_H(t)$ and similar ripple characteristics. Both filters are high-order to minimize the ripple. In phase and quadrature components for an input vector, $\mathbf{x}$, are then found from

$$\mathbf{x}_I = h_{bpf} * \mathbf{x}, \tag{5.16}$$

$$\mathbf{x}_Q = h_H * \mathbf{x}. \tag{5.17}$$

Figure 5.6 shows the spectra after I/Q generation. Note that the Hilbert transform only imparts a 90° phase to the input signal, and so the power spectra for I and Q components are

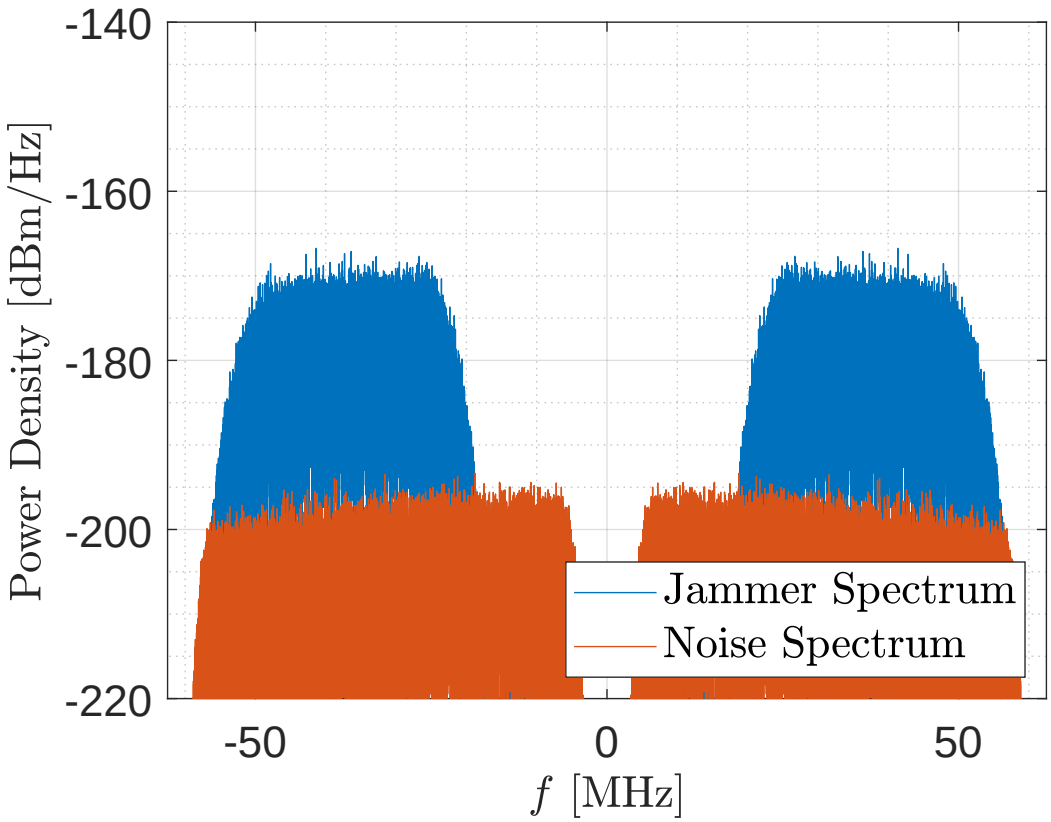

Figure 5.6: Spectral power densities of band-limited Gaussian noise jammer and additive white Gaussian noise present prior to image rejection.

the same. Both h_H and h_{bpf} are designed for the P(Y) code spectrum after downconversion, and so the act of digital filtering mitigates the thermal noise power above 50 MHz. The effect is more pronounced than the anti-aliasing filter, h_{lpf}, because of the higher filter order.

The input vectors are nearly ready for STAP signal processing, but one more step is necessary. Tapped delay lines are used to turn a $N \times 1$ vector into a $N(p+1) \times 1$ vector for p taps. By appending time-delayed samples of the received vector, the STAP received

Table 5.1: Input and output power comparison for STAP constraint vectors.

Input condition	Input power [dBm]	$\mathbf{e}_4$ output power	$\mathbf{e}_5$ output power
Noise only	-117.0	-121.5	-115.7
Noise and jammer	-92.9	-112.7	-112.8

vector,

$$\mathbf{x}^{STAP}(k) = \begin{bmatrix} \mathbf{x}''_{j,I}(k) + \mathbf{x}''_{N,I}(k) \\ \mathbf{x}''_{j,I}(k-1) + \mathbf{x}''_{N,I}(k-1) \\ \vdots \\ \mathbf{x}''_{j,I}(k-p) + \mathbf{x}''_{N,I}(k-p) \end{bmatrix} + j \begin{bmatrix} \mathbf{x}''_{j,Q}(k) + \mathbf{x}''_{N,Q}(k) \\ \mathbf{x}''_{j,Q}(k-1) + \mathbf{x}''_{N,Q}(k-1) \\ \vdots \\ \mathbf{x}''_{j,Q}(k-p) + \mathbf{x}''_{N,Q}(k-p) \end{bmatrix}, \tag{5.18}$$

is found, and can be input into (2.28).

For $p = 3$ taps, (2.28) was applied to $\mathbf{x}^{STAP}$ using both $\mathbf{e}_4$ and $\mathbf{e}_5$. The input and output spectra for either constraint vector appear in Fig. 5.7. The blue traces are the input spectra, which combine both the jammer component and the thermal noise. The orange traces show the reduction in power over a wide range of frequencies. However, a comparison of the power levels highlights some of the differences more readily than the figure. Power can be found by integrating over either time or frequency axes. The integration time range is selected so that the output power can be found for only the stretch of time after $\mathbf{w}$ converges. Input and output power levels appear in Table 5.1 for both STAP constraints and different input conditions. Prior to utilizing STAP, the input power on a single channel, with no tapped delay lines, is -92.9 dBm. The noise component only, without the jammer, is -117.0 dBm. After STAP processing, the overall output power is -112.7 dBm and 112.8 dBm for $\mathbf{e}_4$, and $\mathbf{e}_5$, respectively. Each of the constraint vectors reduces the the output power to the same level, about 5 dB above the initial noise power. The increase is to be expected as $\|\mathbf{w}\|^2 > 1$ in each case. However, another difference appears when considering the output power of the STAP system in the absence of a jammer. With noise only traveling through the system, the output power under $\mathbf{e}_4$ decreases to -121.5 dBm, whereas the output power under $\mathbf{e}_5$ increases to -115.7 dBm. The explanation for this can be found by considering the front end.

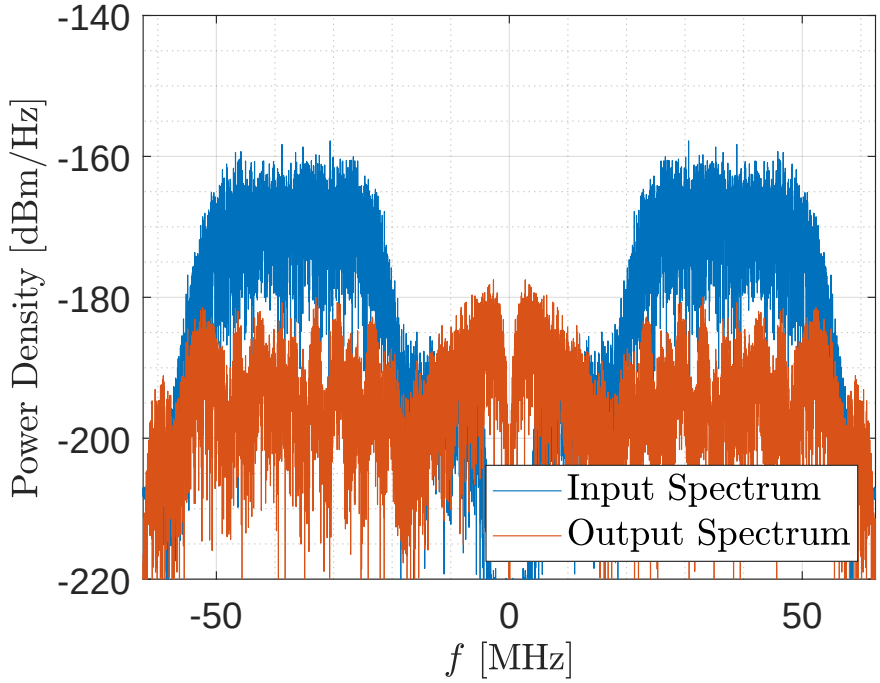

(a) STAP using $\mathbf{e}_4$.

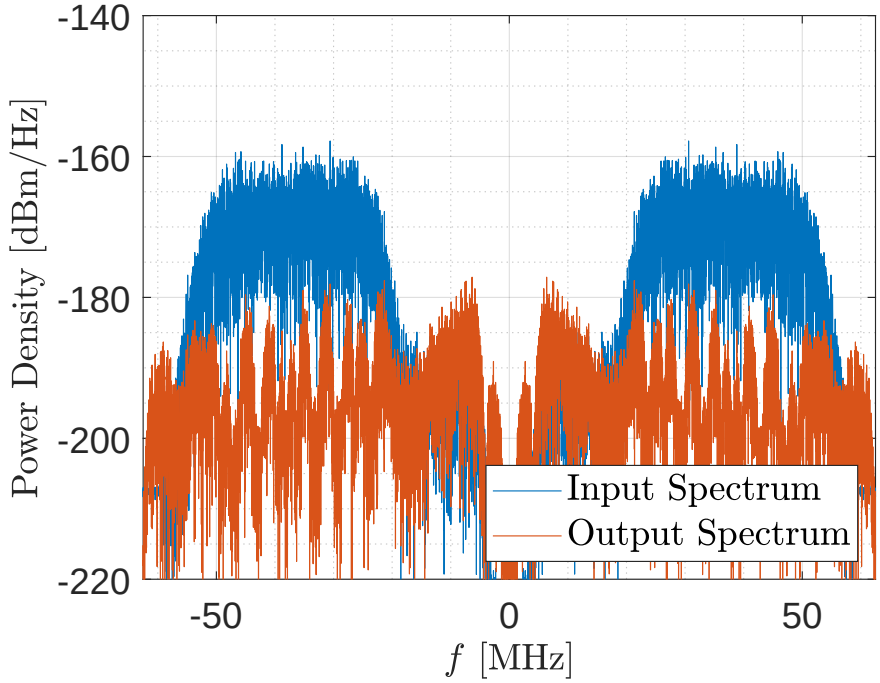

(b) STAP using $\mathbf{e}_5$.

Figure 5.7: Input and output spectra for band-limited Gaussian noise jammer under either STAP constraint.

Before any filtering occurs, the thermal noise is assumed to be Gaussian, i.e., it has a flat power spectral density over the entire frequency domain. This is a good approximation for thermal noise, despite having infinite power. The autocorrelation for this model is the dirac delta function, meaning distinct samples of AWGN, no matter how closely in time they are sampled, are uncorrelated. After filtering, we have band limited Gaussian noise, and instantaneous decorrelation no longer occurs. Adjacent time samples for the noise component are now correlated, though noise across different elements is still uncorrelated. This means that weights generated using $\mathbf{e}_4$ will actually suppress some of the AWGN as seen in the processor. However, $\mathbf{e}_5$ enforces the condition that multiple time samples on the reference element be added together, resulting in the thermal noise adding coherently. The increase from input power is small, though, and does not negate the benefits of $\mathbf{e}_5$ discussed in Section 5.2.1.

STAP increases the degrees of freedom and enables the CRPA to handle wide band jammers, a benefit not imparted by the use of dual-linear elements. Additionally, the STAP architecture is implemented in software and does not require additional front end channels, which include power hungry components such as mixers and analog to digital converters. The greater functionality without significant increases in size or power make a STAP system the better option.

5.3 Discussion

In this chapter, it has been shown that CRPA polarization diversity in a multipath environment, in which the polarization of scattered jammers can change substantially compared to the original jammer, does not offer advantages over a CRPA with the same number of degrees of freedom entirely in the spatial domain. Under full correlation, the CP CRPA produced higher coverage overall in the presence of jammers, due in no small part to the 3 dB polarization mismatch between the GPS signals and the CRPA present in the LP CRPA. Independent scattering reduces the coverage in each case below the 50% level, where the probability of recovering a position solution rapidly declines. Under these circumstance, a very minor advantage is still enjoyed by the CP CRPA. Dual-linear elements reduce the

overall size of the array by having two ports originating from the same antenna, but in terms of performance, there is no apparent advantage when keeping the number of channels the same. If the number of antennas is held fixed, i.e. if the dual-linear CRPA realization has twice the number of channels, marginal increases in performance are present at the cost of greater power demands. The necessary hardware requirements for polarization diversity make it less appealing than increasing degrees of freedom digitally in the time domain.

Additionally, STAP processing for both narrow-band and wideband jamming environments has been considered. Two candidate STAP constraint vectors have been suggested, of which the vector denoted $\mathbf{e}_5$ offers higher signal output power, and therefore coverage. This is due to adjacent time-samples adding coherently at the desired frequency. However, under the receiver assumptions is Section 5.2.2 output noise power also increases by a small amount, due to band-limited Gaussian noise not completely decorrelating instantaneously, however, this does not outweigh the benefits seen by $\mathbf{e}_5$ over $\mathbf{e}_4$. STAP processing also has been shown to succeed at canceling wide band jammers, which is not achieved with space-only processing. Since STAP is performed digitally, unlike polarization diversity which must be realized in hardware, and is able to mitigate wide band jammers, futher investigations into man-portable CRPAs should focus on STAP rather than dual-linear elements.

CHAPTER 6

CONCLUSIONS

Military GPS receivers deliver crucial information that influences real-time decision making by soldiers on the ground. Unfortunately, GPS is easily jammed, both by unsophisticated systems and by the military powers of the world. Mitigation of jamming by the use of CRPAs has shown promising results for large platforms, however the dismounted soldier does not presently have a means to combat this threat. This work has investigated considerations for a man-portable anti-jam system with a focus on the modeling of antennas and the propagation environments they operate in. The analysis was guided by two major factors, namely the unique SWAP constraints of wearable or hand-held CRPAs and the dynamic changes to the operating conditions including dynamic orientation and positioning of disjoint CRPA elements and multipath effects.

The SWAP constraints and the operating environment for a man-portable CRPA present unique design challenges. Efficient processing by a small number of antenna elements and associated hardware is critical for a device that must be carried by a soldier, already burdened by other necessary of equipment. Furthermore, the performance of a sparse CRPA in dynamically changing environments is dependent on a number of factors, such changes in relative positions and orientations. In Chapter 3, techniques for modeling perturbations of CRPA geometry were presented. From these models, an estimate of the necessary update rate for adaptive null-steering algorithms was attained, suggesting that changes in relative element positions and orientations could be handeled by modern processing hardware. However, these predictions do not fully capture the realities of physical antenna performance. Mutual coupling and dielectric losses were shown in Section 3.3.2 to reduce CRPA perfor-

mance when degrees of freedom are strained. This is of particular interest, as the operating environment of a man-portable CRPA introduces additional multipath considerations compared to similar technologies, such as vehicle or aircraft mounted platforms.

As the soldier moves through his environment, changing multipath components from nearby objects and distant terrain have the potential to overwhelm a CRPA limited in degrees of freedom. A single jammer along with its scattered fields can exhaust the CRPA degrees of freedom provided that the components are sufficiently uncorrelated from one another. In contrast, correlated multipath components require only one degree of freedom for cancellation. To address the uncertain statistical characteristics of possible jamming environments, a mixed scattering model was developed in Chapter 4. Under the model assumptions, the relative power in correlated and uncorrelated multipath components is controlled with the specular reflection factor, ς. Fully specular and diffuse reflection are achieved by setting ς to one or zero, respectively. The minor eigenvalues of $\overline{\mathbf{R}}_M$, which determine the CRPAs ability to mitigate multipath components, decrease at a rate of 10 dB per decade with $1 - \varsigma$. As ς increases, more power is transfered into the major eigenvalue associated with the line of sight jammer and the portion of the scattered fields which are linearly dependent with it. Some jammer power still eludes the CRPAs cancellation, specifically, the power in the independent components. However, at a certain point this is small relative to the noise, and GPS service can be recovered.

The mixed scattering model has been presented with values thought reasonable by the author, and chosen to highlight the structure of $\overline{\mathbf{R}}_M$. Yet, realistic values for ς, as well as Γ_{md} and Γ_{ms}, are still unknown. Measuring ς for various objects and different environments introduces many challenges, and confirmation of this model will require an extensive measurement campaign. At present, this model is a framework with room for refinement from experimental verification. Nevertheless, the trend demonstrated by this model was confirmed by investigating algorithm performance in real time, simulated by assuming scattering from objects in motion in Section 4.4. This suggests successful null-steering is possible with objects moving at vehicular speeds provided the algorithm is able to converge rapidly enough to keep pace with a non-stationary $\mathbf{R}$.

The mixed scattering model can incorporate more general electromagnetic effects, such

as changes in polarization from reflection. Chapter 5 incorporates a randomly parameterized reflection matrix, $\mathbf{\Gamma}$, defined by three transformations, rotation, sheer, and reflection. This matrix was used in the fully independent and dependent cases, and suggestions for expanding the mixed scattering framework were given in Section 5.1. Incorporation of $\mathbf{\Gamma}$ into the model enables real-world scattering effects to be included, and enables comparisons to be made between dual-linear and RHCP CRPAs in multipath environments.

Because increasing the degrees of freedom is of interest for both multipath considerations and environments with multiple jammers present, polarimetric CRPAs must be evaluated. Of course, it is necessary to make a distinction between the comparison that can be made between dual-linear and RHCP CRPAs. Doubling the number of ports keeps the CRPA size relatively unchanged, but also doubles the number of front end channels. Increased hardware demands add to the cost, complexity, and power requirements of a system. The benefit of this is that there are now more degrees of freedom. The comparison in Section 3.1 is between a four port RHCP CRPA and an eight-port dual-linear CRPA. Under these circumstances, the dual-linear elements are predicted to perform better than the RHCP elements. However, comparing two four-port CRPAs, as in Section 5.1 is an entirely different scenario. Now the power requirements are assumed to be the same for both CRPAs, as are the degrees of freedom. If the CRPA design is limited to four ports, the dual-linear CRPA does not offer any advantages over the RHCP CRPA for any of the assumed scattering models. The increased power demands are too high to make additional polarimetric degrees of freedom a viable option.

Another way to increase CRPA degrees of freedom is through STAP techniques. Adding tapped delay lines increases processing power, though this can be done digitally and does not require additional hardware beyond potentially a larger processor. Power demands for this technique are relatively modest by comparison, as these additional degrees of freedom do not require any extra ADC channels, or local oscillators. Furthermore, this is not the only advantage offered by STAP. Of the methods considered in this work, only STAP is capable of canceling band-limited Gaussian noise jammers. Section 5.2 demonstrated this, and suggested a possible constraint vector to increase GPS signal power by adding adjacent time samples coherently at the GPS frequency. The multiple advantages to STAP processing

make it the best candidate for implementing a man-portable CRPA.

Modern military operations rely heavily on the electromagnetic spectrum. This is known to our allies and our adversaries. GPS is particularly vulnerable to jamming, though the problem also extends to communications and sensor networks, and this trend shows no sign of stopping. New techniques and technologies are needed to protect our interests, and adaptable modeling methods are necessary to their development. Considerations for a man-portable GPS CRPA have motivated this work, but it is intended to be general enough to find use in multiple domains.

BIBLIOGRAPHY

[1] S. Pace, G. Frost, D. Frelinger, D. Fossum, D. Wassem, and M. M. Pinto, *Global Positioning System: Assessing National Policies.* Santa Monica: Rand Publishing, 1996.

[2] I.-G.-J. GPS Directorate, "Navstar GPS space segment/navigation user interfaces." IS-GPS-200J, May 2018.

[3] I. T. McMichael, E. Lundberg, D. Hanna, and S. Best, "Horizon nulling helix antennas for GPS timing," in *2017 IEEE International Symposium on Antennas and Propagation & USNC/URSI National Radio Science Meeting*, IEEE, July 2017.

[4] E. L. Gordon, H. S. Eilts, and J. P. Volpi, "Directed reception pattern antenna." US Patent 5410321, Apr. 25, 1995.

[5] B. R. Rao, *GPS/GNSS Antennas.* Norwood, MA: Artech House, 2012.

[6] D. S. DeLorenzo, S. C. Lo, P. K. Enge, and J. Rife, "Calibrating adaptive antenna arrays for high-integrity GPS," *GPS Solutions*, vol. 16, pp. 221–230, May 2011.

[7] R. L. Fante and J. J. Vaccaro, "Evaluation of adaptive space-time-polarization cancellation of broadband interference," in *2002 IEEE Position Location and Navigation Symposium*, 2002.

[8] B. Clerckx and C. Oestges, *MIMO Wireless Networks.* Waltham, MA: Elsevier Science, 2nd ed., 2013.

[9] P. Almers, E. Bonek, A. Burr, N. Czink, M. Debbah, V. Degli-Esposti, H. Hofstetter, P. Kysti, D. Laurenson, G. Matz, A. Molisch, C. Oestges, and H. zcelik, "Survey of channel and radio propagation models for wireless MIMO systems," *EURASIP Journal on Wireless Communications and Networking*, vol. 2007, no. 1, p. 019070, 2007.

[10] E. D. Kaplan, *Understanding GPS: Principles and Applications.* Norwood, MA: Artech House, 2nd ed., 2005.

[11] B. Widrow, P. Mantey, L. Griffiths, and B. Goode, "Adaptive antenna systems," *Proceedings of the IEEE*, vol. 55, no. 12, pp. 2143–2159, 1967.

[12] S. Applebaum, "Adaptive arrays," *IEEE Transactions on Antennas and Propagation*, vol. 24, pp. 585–598, Sep 1976.

[13] L. Griffiths and C. Jim, "An alternative approach to linearly constrained adaptive beamforming," *IEEE Transactions on Antennas and Propagation*, vol. 30, pp. 27–34, Jan 1982.

[14] J. Griffiths, "Adaptive array processing a tutorial," *IEE Proceedings H Microwaves, Optics and Antennas*, vol. 130, no. 1, pp. 309–313, 1983.

[15] E. Ngai, D. Blejer, T. Phuong, and J. Herd, "Anti-jam performance of small GPS polarimetric arrays," in *IEEE Antennas and Propagation Society International Symposium*, IEEE, 2002.

[16] M. Trinkle and W.-C. Cheuk, "Null-steering GPS dual-polarised antenna arrays," in *Sat Nav 2003 Conference Proceedings*, (Melbourne, Australia), Menay Pty Ltd, July 2003.

[17] W. Cheuk, M. Trinkle, and D. Gray, "Null-steering LMS dual-polarised adaptive antenna arrays for GPS," *Journal of Global Positioning Systems*, vol. 4, pp. 258–267, Dec. 2005.

[18] J. Wang and M. G. Amin, "Multiple interference cancellation performance for GPS receivers with dual-polarized antenna arrays," *EURASIP Journal on Advances in Signal Processing*, vol. 2008, Oct 2008.

[19] G. Hatke, "Adaptive array processing for wideband nulling in GPS systems," in *Conference Record of Thirty-Second Asilomar Conference on Signals, Systems and Computers (Cat. No.98CH36284)*, IEEE, 1998.

[20] R. L. Fante, "Performance measures for GPS anti-jam antenna arrays." The MITRE Corporation, 2006.

[21] D. S. DeLorenzo, J. Gautier, J. Rife, P. Enge, and D. Akos, "Adaptive array processing for GPS interference rejection," in *Proceedings of the 18th International Technical Meeting of the Satellite Division of the Institute of Navigation*, 2005.

[22] D. S. DeLorenzo, *Navigation accuracy and interference rejection for GPS adaptive antenna arrays*. PhD thesis, Stanford University, 2007.

[23] R. Fante and J. Vaccaro, "Wideband cancellation of interference in a GPS receive array," *IEEE Transactions on Aerospace and Electronic Systems*, vol. 36, pp. 549–564, Apr 2000.

[24] Y. C. Chuang and I. J. Gupta, "On-the-fly estimation of antenna induced biases in SFAP based GNSS antenna arrays," *Navigation*, vol. 61, pp. 323–330, Dec 2014.

[25] A. Rivera-Albino and C. A. Balanis, "Adaptive spherical array with non-uniformly spaced taps for GPS signal processing," in *2011 IEEE International Symposium on Antennas and Propagation (APSURSI)*, IEEE, Jul 2011.

[26] I. J. Gupta, T.-H. Lee, K. A. Griffith, C. D. Slick, C. J. Reddy, M. C. Bailey, and D. DeCarlo, "Non-planar adaptive antenna arrays for GPS receivers," *IEEE Antennas and Propagation Magazine*, vol. 52, pp. 35–51, Oct 2010.

[27] P. J. Soh, B. V. den Bergh, H. Xu, H. Aliakbarian, S. Farsi, P. Samal, G. A. E. Vandenbosch, D. M. M.-P. Schreurs, and B. K. J. C. Nauwelaers, "A smart wearable textile array system for biomedical telemetry applications," *IEEE Transactions on Microwave Theory and Techniques*, vol. 61, pp. 2253–2261, May 2013.

[28] J. Li, "GPS interference mitigation for small UAV applications," Master's thesis, The University of Adelaide, Adelaide, South Australia, 2009.

[29] D. Reynolds, A. Brown, and A. Reynolds, "Miniaturized GPS antenna array technology and predicted anti-jam performance," (Nashville), pp. 777–785, the Satellite Division of the Institute of Navigation, Sept. 1999.

[30] R. J. Mailloux, *Phased Array Antenna Handbook*. Artech House Publishers, 3rd ed., 2018.

[31] M. Jensen and J. Wallace, "A review of antennas and propagation for MIMO wireless communications," *IEEE Transactions on Antennas and Propagation*, vol. 52, pp. 2810–2824, Nov. 2004.

[32] G. N. Kamga, M. Xia, and S. Aissa, "Spectral-efficiency analysis of regular- and large-scale (massive) MIMO with a comprehensive channel model," *IEEE Transactions on Vehicular Technology*, vol. 66, pp. 4984–4996, June 2017.

[33] K. Mammasis, R. W. Stewart, and J. S. Thompson, "Spatial fading correlation model using mixtures of von mises fisher distributions," *IEEE Transactions on Wireless Communications*, vol. 8, pp. 2046–2055, Apr. 2009.

[34] M. Patzold and B. O. Hogstad, "A wideband MIMO channel model derived from the geometric elliptical scattering model," in *2006 3rd International Symposium on Wireless Communication Systems*, IEEE, Sep 2006.

[35] S. Valaee, B. Champagne, and P. Kabal, "Parametric localization of distributed sources," *IEEE Transactions on Signal Processing*, vol. 43, no. 9, pp. 2144–2153, 1995.

[36] Z. Lu, J. Wang, B. Ba, and D. Wang, "Direct position determination of coherently distributed noncircular sources," *Wireless Communications and Mobile Computing*, vol. 2018, pp. 1–12, Jun 2018.

[37] T. Wu, Z. Deng, Y. Li, and Y. Huang, "Two-dimensional DOA estimation for incoherently distributed sources with uniform rectangular arrays," *Sensors*, vol. 18, p. 3600, Oct 2018.

[38] J. Cadzow, "A high resolution direction-of-arrival algorithm for narrow-band coherent and incoherent sources," *IEEE Transactions on Acoustics, Speech, and Signal Processing*, vol. 36, pp. 965–979, Jul 1988.

[39] J. A. Maloney, D.-H. Kwon, R. Janaswamy, and S. D. Keller, "Comparison of radiation pattern modeling methods for GPS controlled reception pattern array," in *2017 IEEE International Symposium on Antennas and Propagation & USNC/URSI National Radio Science Meeting*, pp. 1897–1898, IEEE, July 2017.

[40] J. A. Maloney, S. D. Keller, T. K. Anthony, S. J. Weiss, D.-H. Kwon, and R. Janaswamy, "Measurement of a four channel analog beamformer for anti-jam GPS applications," in *2019 URSI National Radio Science Meeting (USNC-URSI NSRM)*, 2018.

[41] J. A. Maloney, D.-H. Kwon, R. Janaswamy, and S. D. Keller, "Effects of electromagnetic modeling methods on coverage prediction of anti-jam GPS antenna," in *2018 IEEE International Symposium on Antennas and Propagation & USNC/URSI National Radio Science Meeting*, pp. 1563–1564, IEEE, July 2018.

[42] J. A. Maloney, D.-H. Kwon, R. Janaswamy, S. D. Keller, T. K. Anthony, J. T. Clark, R. Harris, A. Harrison, and S. J. Weiss, "Hardware realization and performance measurement of an anti-jam GPS antenna array," in *2019 IEEE International Symposium on Antennas and Propagation & USNC/URSI National Radio Science Meeting*, 2019. Submitted for publication.

[43] J. A. Maloney, D.-H. Kwon, S. D. Keller, and R. Janaswamy, "Realistic GPS coverage prediction for dual-polarized controlled reception pattern antennas," *IEEE Antennas and Wireless Propagation Letters*, vol. 16, pp. 1907–1910, 2017.

[44] B. Volcker, M. Bengtsson, and B. Ottersten, *Adaptive Antenna Arrays Trends and Applications*, ch. Spatially Spread Sources in Antenna Array Processing, pp. 394–419. Springer Berlin Heidelberg, 2004.

[45] A. Massa, M. Donelli, F. DeNatale, S. Caorsi, and A. Lommi, "Planar antenna array control with genetic algorithms and adaptive array theory," *IEEE Transactions on Antennas and Propagation*, vol. 52, pp. 2919–2924, Nov 2004.

[46] R. Janaswamy, *Radiowave Propagation and Smart Antennas for Wireless Communications*. Norwell, Massachusetts: Kluwer Academic Publishers Group, 2001.

[47] A. Neskovic, N. Neskovic, and G. Paunovic, "Modern approaches in modeling of mobile radio systems propagation environment," *IEEE Communications Surveys & Tutorials*, vol. 3, no. 3, pp. 2–12, 2000.

[48] G. Xu, *GPS, Theory, Algorithms and Applications*. New York: Springer, 2003.

[49] K. Amidfa, G. Tsoulos, and A. Nix, "Performance evaluation of direction-of-arrival (DOA) estimation algorithms for mobile communication systems," in *2000 IEEE 51st Vehicular Technology Conference Proceedings*, IEEE.

[50] J. Salz and J. Winters, "Effect of fading correlation on adaptive arrays in digital mobile radio," *IEEE Transactions on Vehicular Technology*, vol. 43, no. 4, pp. 1049–1057, 1994.

[51] W. C. Jakes, *Microwave Mobile Communications*. John Wiley & Sons, 1974.

[52] P. Stoica, Z. Wang, and J. Li, "Robust capon beamforming," in *Conference Record of the Thirty-Sixth Asilomar Conference on Signals, Systems and Computers*, pp. 876–880, 2002.

[53] S. Haykin, *Adaptive Filter Theory*. Upper Saddle River, New Jersey: Prentice Hall, 3rd ed., 1996.

[54] J. Liu, W. Liu, H. Liu, B. Chen, X.-G. Xia, and F. Dai, "Average SINR calculation of a persymmetric sample matrix inversion beamformer," *IEEE Transactions on Signal Processing*, vol. 64, pp. 2135–2145, Apr 2016.

[55] Y. Gu and A. Leshem, "Robust adaptive beamforming based on interference covariance matrix reconstruction and steering vector estimation," *IEEE Transactions on Signal Processing*, vol. 60, pp. 3881–3885, Jul 2012.

[56] J. R. Shewchuk, "An introduction to the conjugate gradient method without the agonizing pain," *Carnegie-Mellon University. Department of Computer Science*, 1994.

[57] F. S. Beckman, *Mathematical Methods for Digital Computers*, vol. 1, ch. The Solution of Linear Equations by the Conjugate Gradient Method, pp. 62–77. Wiley, 1960.

[58] R. Barrett, M. Berry, T. F. Chan, J. Demmel, J. M. Donato, J. Dongarra, V. Eijkhout, R. Pozo, C. Romine, and H. Van der Vorst, *Templates for the solution of linear systems: building blocks for iterative methods*. Siam, 1994.

[59] J. G. Proakis and D. Manolakis, *Digital Signal Processing-Principles, Algorithms, and Applications*. Pearson, 4th ed., 2007.

[60] J. A. Apolinario and M. L. R. de Campos, "The constrained conjugate gradient algorithm," *IEEE Signal Processing Letters*, vol. 7, pp. 351–354, Dec 2000.

[61] W. Sethares, D. Lawrence, C. Johnson, and R. Bitmead, "Parameter drift in LMS adaptive filters," *IEEE Transactions on Acoustics, Speech, and Signal Processing*, vol. 34, pp. 868–879, Aug 1986.

[62] R. Klemm, *Principles of Space-Time Adaptive Processing*. Institution of Engineering and Technology, 2006.

[63] R. Klemm, ed., *Applications of Space-Time Adaptive Processing*. Institution of Engineering and Technology, 2004.

[64] O. L. Frost, "An algorithm for linearly constrained adaptive array processing," *Proceedings of the IEEE*, vol. 60, no. 8, pp. 926–935, 1972.

[65] J. R. Guerci, *Space-Time Adaptive Procesing for Radar*. Artech House, 2014.

[66] W. L. Melvin and J. A. Scheer, eds., *Principles of Modern Radar*. SciTech Publishing Inc, 2012.

[67] A. Barmettler, "CalSky," Oct. 2017.

[68] R. F. Harrington, *Time-harmonic electromagnetic fields*. New York, NY: McGraw-Hill, 1961.

[69] C. A. Balanis, *Advanced Engineering Electromagnetics*. New York, NY: Wiley, 1989.

[70] D. J. Griffiths, *Introduction to Electrodynamics*. Englewood Cliffs, NJ: Prentice-Hall, 1981.

[71] C. A. Balanis, *Antenna Theory: Analysis and Design*. Hoboken, NJ: Wiley-Interscience, 3rd ed., 2005.

[72] D. M. Pozar, *Microwave Engineering*. John Wiley and Sons Ltd, fourth ed., 2011.

[73] R. Marks and D. Williams, "A general waveguide circuit theory," *Journal of Research of the National Institute of Standards and Technology*, vol. 97, p. 533, Sep 1992.

[74] R. Schmidt, *a signal subspace approach to multiple emitter location and spectral estimation*. PhD thesis, Stanford University, 1981.

[75] D. R. H. Craig F. Bohren, *Absorption and Scattering of Light by Small Particles*. Wiley-VCH, 2008.

[76] R. Mohammadkhani, *Adaptive impedance matching to compensate mutual coupling effects on compact MIMO systems.* PhD thesis, The University of Edinburgh, 2012.

[77] W. Weichselberger, *Spatial Structure of Multiple Antenna Radio Channels.* PhD thesis, Institut fur Nachrichtentechnik und Hochfrequenztechnik, 2003.

[78] D. H. Johnson and D. E. Dugeon, *Array Signal Processing, Concepts and Techniques.* Upper Saddle River, New Jersey: PTR Prentice-Hall, Inc., 1993.

[79] B. Widrow, *Aspects of network and system theory*, ch. Adaptive Filters, pp. 563–586. Holt, Rinehart and Winston, 1971.

[80] D. G. Luenberger, "The conjugate residual method for constrained minimization problems," *SIAM Journal on Numerical Analysis*, vol. 7, pp. 390–398, Sep 1970.

[81] P. Misra and P. Enge, *Global Positioning System : Signals, Measurements, and Performance.* Ganga-Jamuna Press, second ed., 2006.

[82] BBC, "Boxer Hatton packs half-ton punch." online, June 2007.

[83] R. Janaswamy, "Effect of element mutual coupling on the capacity of fixed length linear arrays," *IEEE Antennas and Wireless Propagation Letters*, vol. 1, pp. 157–160, 2002.

[84] S. D. Keller, S. J. Weiss, J. A. Maloney, D.-H. Kwon, R. Janaswamy, and J. Morley, "Design considerations for a wearable anti-jam GPS antenna," in *2018 2nd URSI Atlantic Radio Science Meeting (AT-RASC)*, IEEE, May 2018.

[85] R. Cao and S.-C. Yu, "Wideband compact CPW-fed circularly polarized antenna for universal UHF RFID reader," *IEEE Transactions on Antennas and Propagation*, vol. 63, pp. 4148–4151, Sep 2015.

[86] A. K. Fung, *Microwave Scattering and Emission Models and Their Applications.* Artech House, 1994.

[87] R. N. Colwell, *Manual of Remote Sensing.* American Society of Photogrammetry, second ed., 1983.

[88] A. Saleh and R. Valenzuela, "A statistical model for indoor multipath propagation," *IEEE Journal on Selected Areas in Communications*, vol. 5, pp. 128–137, Feb 1987.

[89] W. M. Cornette and J. G. Shanks, "Physically reasonable analytic expression for the single-scattering phase function," *Applied Optics*, vol. 31, p. 3152, Jun 1992.